

## REPORT DOCUMENTATION PAGE

Form Approved  
OMB No. 0704-0188

The public reporting burden for this collection of information is estimated to average 1 hour per response, including the time for reviewing instructions, searching existing data sources, gathering and maintaining the data needed, and completing and reviewing the collection of information. Send comments regarding this burden estimate or any other aspect of this collection of information, including suggestions for reducing the burden, to Department of Defense, Washington Headquarters Services, Directorate for Information Operations and Reports (0704-0188), 1215 Jefferson Davis Highway, Suite 1204, Arlington, VA 22202-4302. Respondents should be aware that notwithstanding any other provision of law, no person shall be subject to any penalty for failing to comply with a collection of information if it does not display a currently valid OMB control number.  
PLEASE DO NOT RETURN YOUR FORM TO THE ABOVE ADDRESS.

1. REPORT DATE (DD-MM-YYYY)	2. REPORT TYPE	3. DATES COVERED (From - To)		
05/17/2010	Final report	October 29, 2008-February 28, 2010		
4. TITLE AND SUBTITLE			5a. CONTRACT NUMBER	
Intrinsic Impact and Fatigue Property Degradation of Composite Materials in Sea Water			5b. GRANT NUMBER N00014-08-1-0137	
			5c. PROGRAM ELEMENT NUMBER	
6. AUTHOR(S) Luoyu Roy Xu			5d. PROJECT NUMBER	
			5e. TASK NUMBER	
			5f. WORK UNIT NUMBER	
7. PERFORMING ORGANIZATION NAME(S) AND ADDRESS(ES) Vanderbilt University Division of Sponsored Research Station B, Box 7749 2301 Vanderbilt Place, Nashville, TN 37235-7749			8. PERFORMING ORGANIZATION REPORT NUMBER	
9. SPONSORING/MONITORING AGENCY NAME(S) AND ADDRESS(ES) Office of Naval Research 100 Alabama St SW Suit 4R15 Atlanta, GA 30303-3104.			10. SPONSOR/MONITOR'S ACRONYM(S)	
			11. SPONSOR/MONITOR'S REPORT NUMBER(S)	
12. DISTRIBUTION/AVAILABILITY STATEMENT Approved for public release; distribution unlimited.				
13. SUPPLEMENTARY NOTES The views, opinions and/or findings contained in this report are those of the author(s) and should not be construed as an official Department of the Navy position, policy or decision, unless so designated by other documentation.				
14. ABSTRACT Durability and dynamic failure properties are critical parameters for naval composite ships in seawater. However, previous approaches and measurements have significantly underestimated the intrinsic durability of composite structures. In this study, a new composite "fish tank" approach was developed to accurately simulate the material/mechanics conditions of composite structures in seawater. Four E-glass/vinyl ester composite specimens were weakly bonded together to form a seawater tank. Therefore, only one surface of each composite specimen was exposed to seawater and this surface was subjected to drop-weight impact, which is very similar to the dynamic failure process of ship structures subjected to underwa				
15. SUBJECT TERMS durability, dynamic failure,composite materials				
16. SECURITY CLASSIFICATION OF:		17. LIMITATION OF ABSTRACT	18. NUMBER OF PAGES	19a. NAME OF RESPONSIBLE PERSON Luoyu R. Xu
a. REPORT UNCLASSIFIED	b. ABSTRACT UNCLASSIFIED	c. THIS PAGE UNCLASSIFIED	UNCLASSIFIED	19b. TELEPHONE NUMBER (Include area code) 615-335-5493
10				

**Final technical report to the Office of Naval Research**

Contract Number	N00014-08-1-0137
Title of Research	Intrinsic Impact and Fatigue Property Degradation of Composite Materials in Sea Water
Principal Investigator	L. R. Xu
Organization	Vanderbilt University, Nashville, TN

***Abstract***

Durability and dynamic failure properties are critical parameters for naval composite ships in seawater. However, previous measurements have significantly underestimated the intrinsic durability of composite structures. In this study, a new composite “fish tank” approach was developed to accurately simulate the material/mechanics conditions of composite structures in seawater. Four E-glass/vinyl ester composite specimens were weakly bonded together to form a seawater tank. Therefore, only one surface of each composite specimen was exposed to seawater and this surface was subjected to drop-weight impact, which is very similar to the dynamic failure process of ship structures subjected to underwater explosion. A series of experiments of dry and wet composite specimens were conducted to characterize the impact damage, and the residual compression strength. Results of more than 50 specimens with more than 21-month seawater exposure show that the compression after impact strengths of the wet specimens reduced less than 9% compared to the dry baseline specimens. Therefore, durability of current marine composite is much better than previously measured. Our simple and novel “fish tank” durability experiment is expected to provide accurate justification for the required maintenance period of new composite ship structures.

**Technical Section*****Technical Objectives***

The main objectives of this project include: 1) developing a novel approach to accurately simulate the material/mechanics conditions of composite structures in seawater; 2) characterizing the impact damage, and the residual compression strength of marine composites as a function of time of seawater exposure; and 3) conducting a combined experimental and numerical investigation of the interface shear strength measurements.

***Technical Approach***

In this study, a new composite “fish tank” approach was developed. Four E-glass/vinyl ester composite specimens were weakly bonded together to form a seawater tank. Therefore,

May 26, 2010

**20100601012**

only one surface of each composite specimen was exposed to seawater and this surface was subjected to drop-weight impact, which is very similar to the dynamic failure process of ship structures subjected to underwater explosion.

### Materials and sample preparation

Glass fiber reinforced vinyl ester (glass/VE) panels were produced using vacuum assisted resin transfer molding (VARTM) by Prof. U. Vaidya's group at the University of Alabama at Birmingham. Eight layers of plain weave glass fabric (CWR 2400/50 plain weave, Composites One, LLC) were used to produce the panels with approximately 5mm thickness which is required by ASTM D 7137 "Standard Test Method for Compressive Residual Strength Properties of Damaged Polymer Matrix Composite Plates". The fiber fraction of the panels was found to be 54% vol. after burn off testing was conducted. Compression after impact (CAI) testing samples with a dimension of 101.6 mm x 152.4 mm (4" x 6") were cut and machined to meet the strict dimension requirement specified in ASTM D 7137.

### Construction of a composite seawater tank

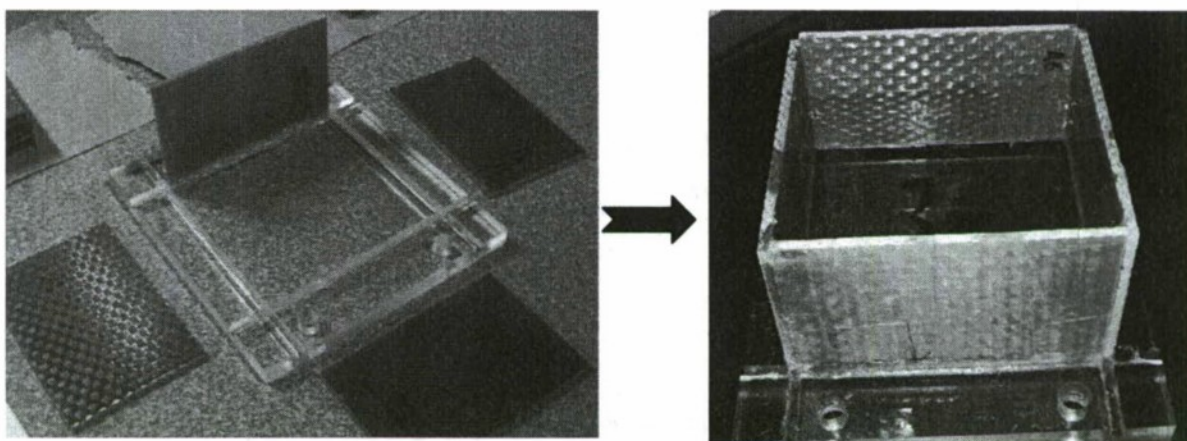


Figure 1. A composite tank before construction (left) and after construction with seawater inside (right)

As shown in Figure 1, silicone rubber as aquarium sealant (Perfecto Manufacturing, Noblesville, IN) were applied to four slots of a base PMMA plate before four composite specimens were inserted. PMMA has very little reaction with seawater. The reason to use silicone rubber is that it provides enough bonding strength under water pressure. Meanwhile, it is not too strong for to break/debond this tank into four composite plates for future impact experiments. After one week of the construction of this tank (full bonding strength), it was filled with synthetic seawater (Ricca Chemical Co., TX). This tank will be disassembled after certain periods of time such as three months, six months etc. to conduct impact and compression experiments (see Figure 2). The impact experiments of dry specimens were conducted to provide baseline data.

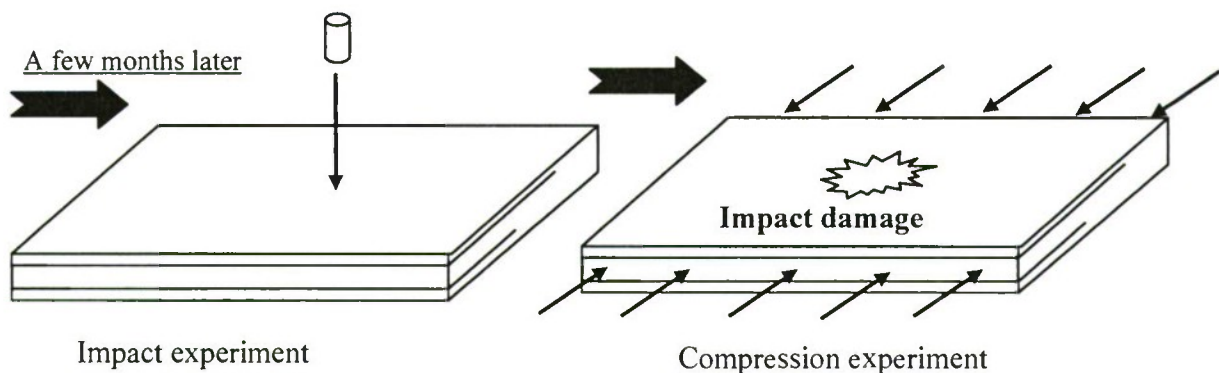


Figure 2. Layered composite specimens subjected to out-of-plane impact and compression

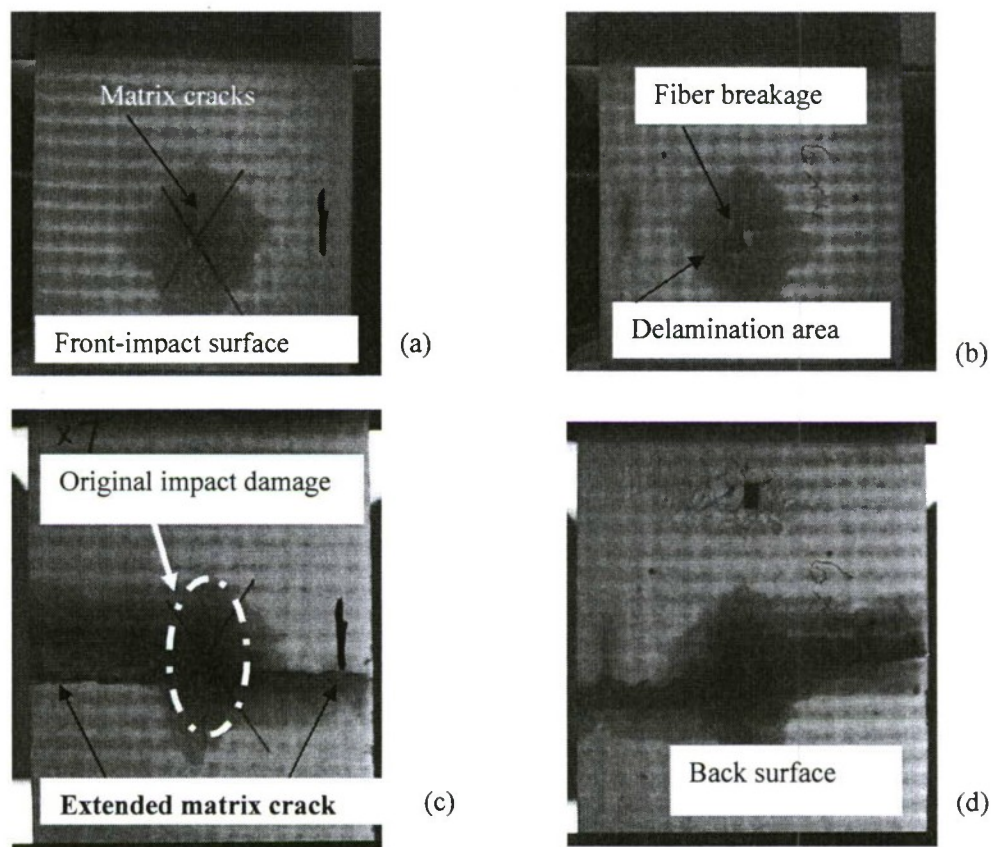


Figure 3. Typical impact damage on the front and back surfaces, (a) and (b), and typical compression failure of the impacted specimen (c) and (d).

### Impact experiments of durability specimens

Impact damage was introduced using a drop tower setup. All samples (fixed four edges) were subjected to an impact (60 joules impact energy) using a 16mm (5/8") diameter hemisphere impactor. Damage zones of the impacted samples are clearly seen in Figure 3(a), (b). For the

front surface directly subjected to impact, dark areas represent internal delamination, with possible several delaminations at the different interfaces. As discussed by Xu and Rosakis [1], these delaminations are mainly shear-dominated, so the interlaminar shear strength is an important parameter for delamination resistance characterization. Also, two major matrix cracks were observed near the impact site (as shown by two dark mark lines). One matrix crack was along the horizontal direction and the other one was along the vertical direction. On the back surface of the impacted specimen, fiber breakage was observed at the impact site and this failure mode contributed to major impact energy absorption. Meanwhile, fiber/matrix debonding appeared as white thin lines on the back surface of the impacted specimens. These four major failure modes indeed make different contributions to the composite impact resistance [2], and we believe fiber breakage and delamination play the major role to absorb impact energy.

### Compression tests for impacted specimens

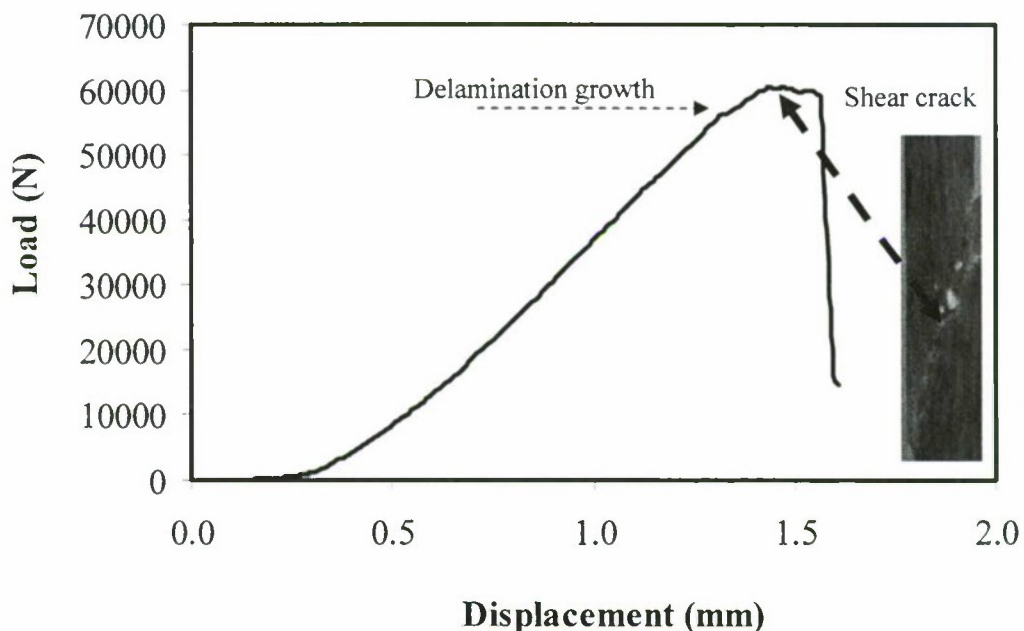


Figure 4. A typical load-displacement curve of a compressive test of an impacted marine composite laminate

Impacted samples were mounted into a compression fixture. A loading rate of 1 mm/min was used. The progressive compression failure started from the impact damage as shown in Figure 4. Initially, as the compression load increased, delamination from the previous impact propagated in a local buckling form. Unlike impact-induced delamination, its propagation is mainly opening-dominated. Delamination also appeared along the horizontal matrix crack and this matrix crack extended to the two edges as the compressive loading increased, as seen in Figure 3. The final failure (maximum load) was controlled by a shear crack near the horizontal matrix crack as seen in Figure 4. An inclined angle around 30-45 degrees (with respect to the compressive loading direction) was observed from the two vertical edges of the failed specimen. These results are similar to previous compressive failure results reported by Daniel [3], Tsai and Sun [4], Oguni

and Ravichandran [5]. A load-displacement curve is illustrated in Figure 4 for a compressive experiment of an impacted specimen. The initial non-linear part is caused by the initial gap of the compressive fixture. Then a long linear load-displacement part is recorded. The failure mode starts from the opening delamination from the impacted-induced delamination (shear-dominated), followed by a sudden propagation of the longitudinal matrix crack and a final shear crack appeared along the specimen edge based on the recorded high-definition video.

#### **A master curve of the accurate durability measurement using our new approach**

Table 1 shows all CAI data up to 21 months. The dry specimen is used as a baseline specimen or comparison. Since the CAI strength combines the effects of the seawater exposure and impact damage, it is very convenient to use this simple parameter to present complicated impact damage and the seawater effect.

Table 1. History of the Compression-After-Impact (CAI) Strength in seawater

Time (months)	Mean CAI (Mpa)	% Reduction
0	132.98 ± 7.59	0
4	140.40 ± 4.37	+5.58
9.5	121.39 ± 10.98	-8.72
13	125.63 ± 9.05	-5.53
17	128.15 ± 8.77	-3.63
21	122.22 ± 9.22	-8.09

From the table, we notice that the CAI strength reduction is less than 9% after one-year seawater exposure. This is much less than 40% CAI strength reduction as reported by Imielinska and Guillaumat [6] on the same compression after impact experiments with different composite materials. Obviously, if the durability of a new composite ship reduced so dramatically in less than one year, this ship should not be manufactured. This comparison confirms that our new approach produces more reasonable data as our experiments simulate the right material conditions.

These CAI data are also plotted in Figure 5. A slight increase in CAI strength for the specimen after four-month seawater exposure is probably due to the specimen size effect. The average thickness of this set of specimens is at least 10% higher than other specimens. The CAI strength is not a material property so it is sensitive to the specimen sizes especially the specimen thickness. After four-month seawater exposure, the CAI strength reduction has very small change up to 21 months, which might be related to seawater saturation inside the specimens. Since no additional seawater enters the composite specimens after a certain amount of time [7], no new damage caused by seawater effect such as fiber-matrix interface strength reduction will occur. Therefore, the CAI strength of the wet specimen, which combines the effects of impact damage (not a function of seawater exposure time), and the seawater damage (such as to the matrix), will have very small change in one to two years. Since there is no protective coating or

painting on the composite plates, the future composite ship structures, which have strong coating or painting, should have excellent durability and dynamic failure properties.

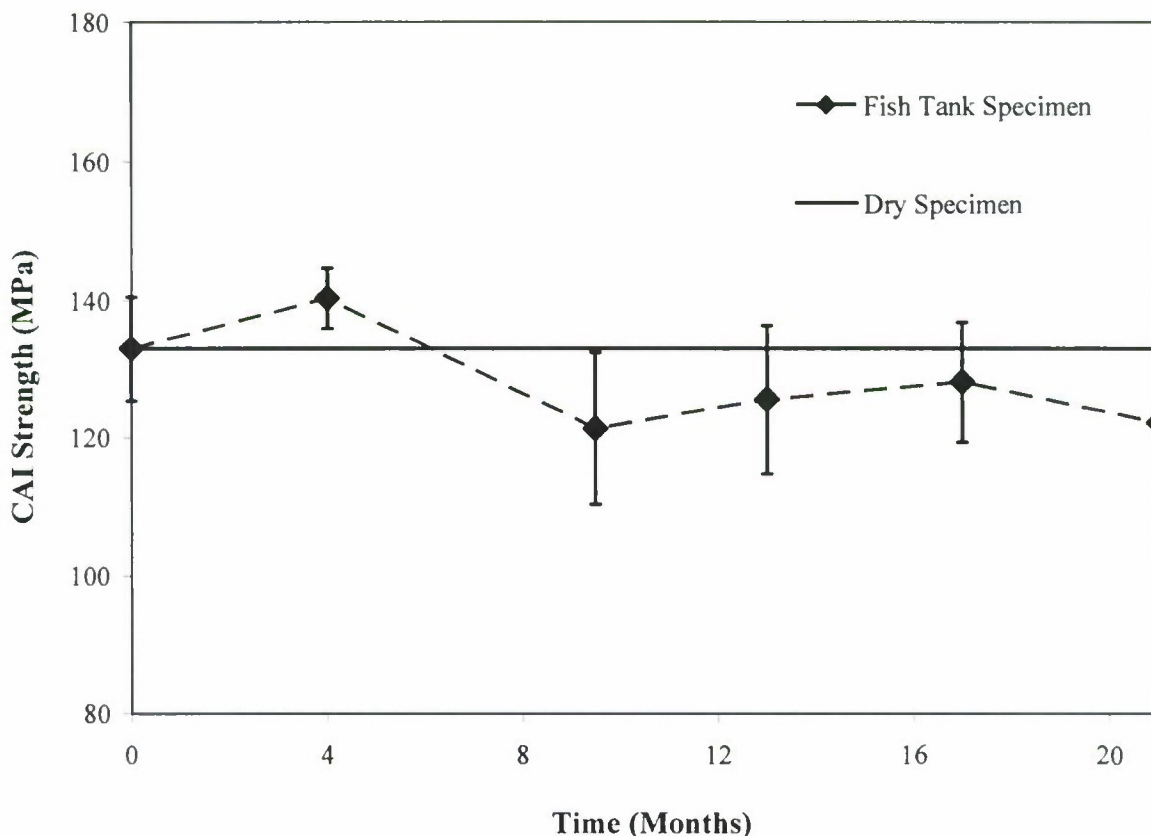


Figure 5. A master curve of the compressive strength change as a function of seawater exposure time

#### Experimental studies of two common approaches of shear strength measurements

Since the previous impact failure modes included shear-dominated delamination and shear cracks, shear strength measurements are very important for composite materials. Among several shear strength approaches, the Iosipescu shear test has been used for the past 20-30 years because the Iosipescu shear specimen provides a test region of uniform shear stress, rather than a parabolic variation shown by the short-beam shear specimen as seen in Figure 6.

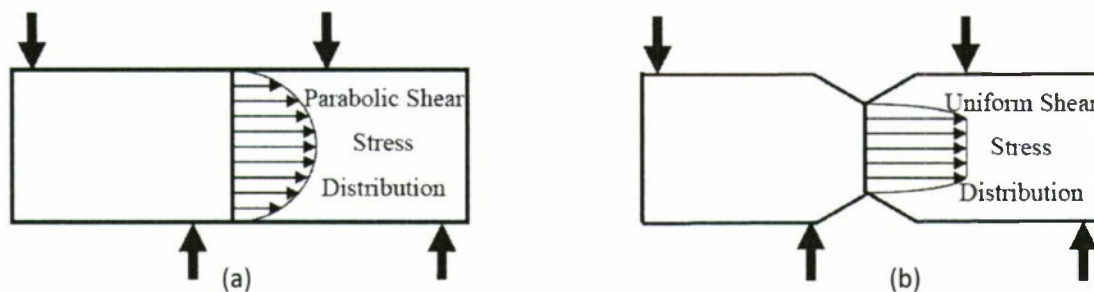


Figure 6. Schematic of (a) Butt-joint shear specimen and (b) Iosipescu shear specimen.

However, due to different shear stress distributions of these two approaches, will they lead to different shear strength measurements? No one answers this fundamental question and we try to provide partial answer using simplified materials, i. e., bonded homogenous materials with weak interfaces. Test specimens were made of three different types of materials including Aluminum, PMMA and Polycarbonate. The reason for using bonded specimens is that we want the shear specimens to fail at the interface by shear and not in tension at the upper edges. The adhesive used in this experiment is Loctite 384. One of the key requirements in choosing the adhesive was that its strength should be close to or lesser than that of the bulk material. The individual halves were machined to ensure that they were of the desired dimensions and were sand-blasted at the bonding surfaces to provide good adhesion. The specimens were bonded using a fixture to guarantee their dimensionality after bonding under room temperature.

The test set-up consists of three parts including a mechanical system for testing the specimens, an optical system used to develop photoelasticity fringe patterns and an imaging system to record and capture the images. All specimens were loaded to failure and their strength data were recorded as shown in Table 2. It should be noted that the failure of all specimens was sudden and brittle. From the above table it is seen that the average values are close and the data from the Iosipescu shear test are slight higher. The Iosipescu specimen shows a higher value of measured bonding strength because of the lower cross sectional area involved. The Iosipescu specimen has about 60% of the cross sectional area of the butt-joint shear specimen and thus it leads to a greater value of the measured bonding strength due the “size effect”. These results show that the shear stress distribution has least effect on the shear strength measurements. Of course, this result is only applicable to any interface without stress singularity such as caused by a crack (macro-scale) or bi-material corner.

Table 2. Measured Bonding Shear Strength Data (at least 20 specimens tested for each case)

Materials	Iosipescu shear (MPa)	Butt-joint shear (MPa)	Difference (%)
Aluminum-Al	10.75	10.16	+ 5.8
Polycarbonate-PC	10.99	8.51	+ 23.3
PMMA-PMMA	11.58	10.19	+ 13.6

### Modeling and simulation of the shear strength comparison

A finite element model of the specimen was built using ANSYS 11.0 to obtain the distribution of the stresses in the specimen. Two different types of materials were chosen to represent the actual experiment. A linear, elastic and isotropic material was chosen as only brittle materials are considered in this analysis. The specimen was meshed using Plane 42 quad elements. A finer mesh was used in the notch region in order to capture any stress singularities. A coarser mesh was used elsewhere to save on computational time and effort. Plane 42 elements were exclusively used in order to meet the requirements of the plotting software Tecplot. In order to incorporate a realistic simulation of the load transfer from the fixture to the specimen, an iterative procedure was adopted. The left portion of the specimen is fixed and cannot move in the vertical dimension. Displacement constraints are applied similar to what is observed in reality. The top left edge node is restrained from moving in both x and y directions in order to prevent rigid body movements. On the right portion, an initial vertical uniform displacement is applied. Now the reaction loads at each of the nodes with a constraint is checked to verify that they are not in tension. The constraint was removed from those nodes which showed a tensile reaction force instead of a compressive one and a new analysis with the updated set of boundary conditions was carried out. This was done until convergence and the total applied load was obtained by integrating the shear stress across the interface of the specimen.

The load applied in the form of displacements was initially obtained from the experimental load-displacement plot. The actual load on the specimen was later obtained by integrating the shear stress along the interface. This procedure was iteratively carried until the required load (for matching the fringe patterns) was obtained. The numerical modeling of the shear specimens was validated by comparison of the numerical photoelastic fringe plots with the experimental ones. The comparison for an Iosipescu shear specimen is shown in Figure 7. It is seen that the experimental and numerical patterns have a pretty close match. The fringes appear concentrated around the top and bottom loading blocks. This is due to the highly non-linear force distribution on the upper right and lower left loading blocks.

These results show that the shear stress distribution has least influence on the strength measurements. Therefore, future simplified and efficient methods can be developed to measure important shear strengths as long as the shear stress is not singular.

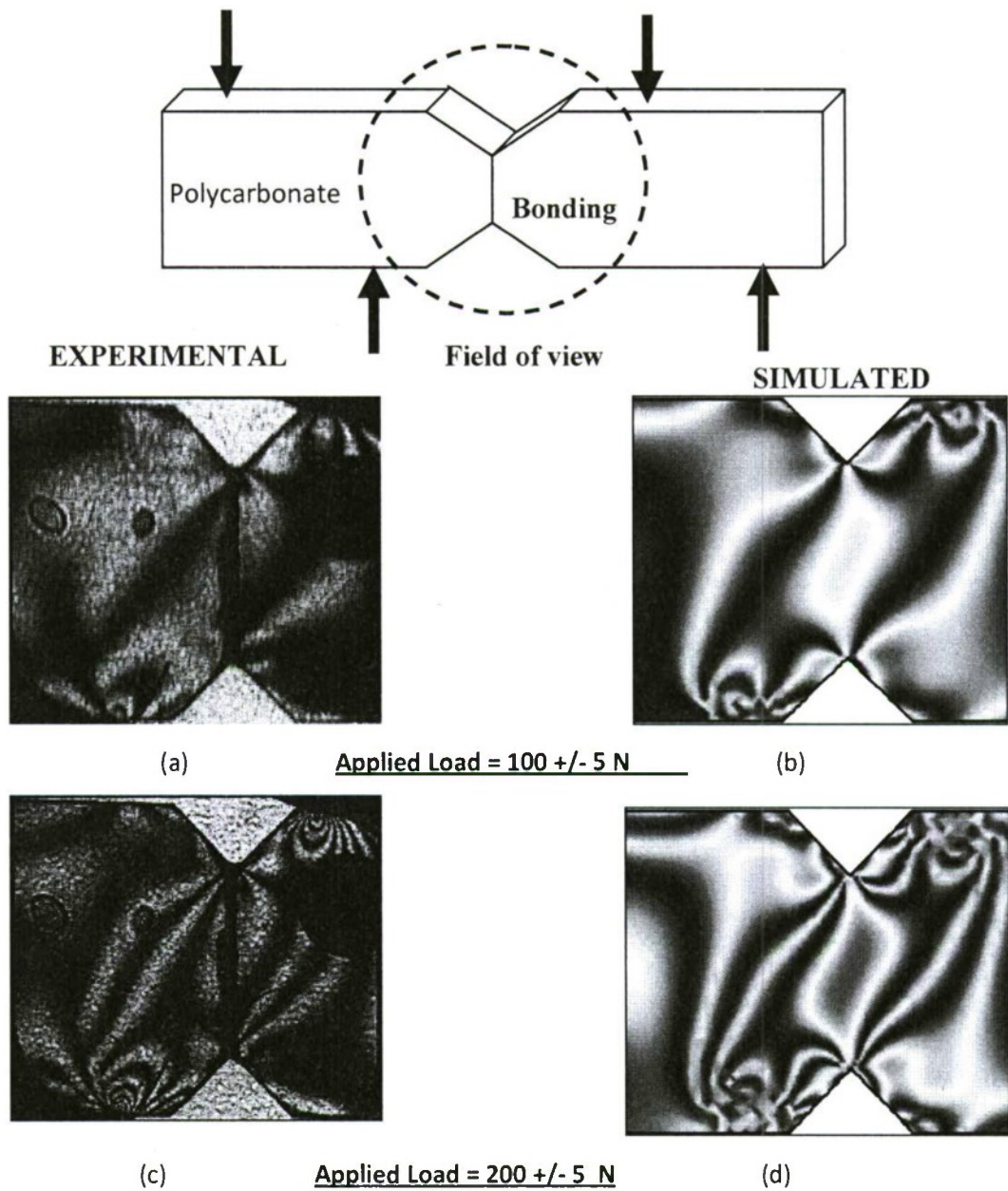


Figure 7. Comparison between experimental and finite element generated fringe patterns for an Iosipescu specimen made of bonded Polycarbonate

## REFERENCES

1. Xu, L. R. and Rosakis, A. J., 2002. Impact failure characteristics in sandwich structures; Part I: Basic Failure Mode Selections. *International Journal of Solids and Structures*, 39, 4215-4235.
2. Abrate, S., 1998. Impact on composite structures, Cambridge University Press, New York.
3. Daniel, I. M. <http://www.composites.northwestern.edu/>
4. Tsai, J. and Sun, C.T., 2004, Dynamic compressive strength of polymeric composites, *International Journal of Solids and Structures*, 41, 3211-3224.
5. Oguni, K., and Ravichandran, G., 2001. Dynamic compressive behavior of unidirectional E-glass/vinylester composites. *Journal of Materials Science*, 36, 831-838.
6. Imielinska, K. and Guillaumat, L. , 2004. The effect of water immersion ageing on low-velocity impact behaviour of woven aramid–glass fibre/epoxy composites, *Composite Science and Technology*, 64, 2271–2278.
7. Weitsman, YJ, and Elahi. M., 2000. Effects of fluids on the deformation, strength and durability of polymeric composites—an overview. *Mech Time- Depend Mater*, 4,107–26.

## Publications (ONR-supported since October 2008, see attached PDF file)

1. L. R. Xu, "In-class Paper Demonstration and Experiment for Mechanics of Materials and Advanced Solid Mechanics Courses," *International Journal of Engineering Education*, Vol. 24, pp. 540-544. 2008.
2. L. R. Xu and A. J. Rosakis, "Real-time Experimental Investigation on Dynamic Failure of Sandwich Structures and Layered Materials", *Composite Materials and Sandwich Structures, An Anthology of ONR Sponsored Research* (editors: E.E. Gdoutos, I.M. Daniel and Y.D.S. Rajapakse), pp. 571-604, Springer publisher, 2009.
3. A. Krishnan and L. R. Xu, "Effect of the interfacial stress distribution on the material interfacial shear strength measurement," *Experimental Mechanics*, Vol. 50. pp. 293-288. 2010.
4. A. Krishnan, Xu LR, "Systematic evaluation of bonding strengths and fracture toughnesses of adhesive joints," *Submitted to Journal of Adhesion*, 2010.
5. A. Krishnan and L. Roy Xu, "An efficient approach to measure the Mode II fracture toughness of materials with preferred interfaces," Submitted to *International Journal of Fracture*, 2010

# Real-Time Experimental Investigation on Dynamic Failure of Sandwich Structures and Layered Materials

L. Roy Xu and Ares J. Rosakis

**Abstract** We present a systematic experimental investigation of the generation and subsequent evolution of dynamic failure modes in sandwich structures and layered materials subjected to out-of-plane low-speed impact. Model sandwich specimens involving a compliant polymer core sandwiched between two metal layers and other model layered materials were designed to simulate failure evolution mechanisms in real sandwich structures and layered materials. High-speed photography and dynamic photoelasticity were utilized to study the nature and sequence of such failure modes. In all cases, inter-layer (interfacial) cracks appeared first. These cracks were shear-dominated and were often intersonic even under moderate impact speeds. The transition from inter-layer crack growth to intra-layer crack formation was also observed. The shear inter-layer cracks kinked into the core layer, propagated as opening-dominated intra-layer cracks and eventually branched as they attained high enough growth speeds causing brittle core fragmentation. In-depth failure mechanics experiments on the dynamic crack branching, crack kinking and penetration at a weak interface, interfacial debonding ahead of a main incident crack were also conducted to understand the physical insight of the dynamic failure modes and their transition observed from sandwich structures and layered materials.

## 1 Introduction

Layered materials and sandwich structures have diverse and technologically interesting applications in many areas of engineering. These include the increased use of composite laminates in aerospace and automotive engineering; the introduction

---

L.R. Xu (✉)

Department of Civil and Environmental Engineering, Vanderbilt University, Nashville,  
TN 37235, USA  
e-mail: luoyu.r.xu@gmail.com

A.J. Rosakis

Graduate Aeronautical Laboratories, California Institute of Technology, Pasadena,  
CA 91125, USA  
e-mail: rosakis@aero.caltech.edu

of layered concrete pavements in civil engineering; the use of thin films and layered structures in micro-electronic components, and recently, the introduction of sandwich structures in a variety of naval engineering applications (Hutchinson and Suo [1]; Rajapakse [2]). While failure characteristics of layered materials and sandwich structures subjected to static loading have been investigated extensively in the past years, their dynamic counterparts have remained elusive (Sun and Rechak [3]; Cantwell and Morton [4]; Abrate [5]). Indeed, the presence of highly complex and transient dynamic failure modes in such materials and the inaccessibility of internal damage have resulted in experimental studies limited to only the final impact damage and the residual strengths. To begin addressing the need for real-time observations of failure events, the work presented here focuses on the study of such events in model sandwich structures, and in particular, on the identification of their nature, chronological evolution and interaction.

To identify the evolution of failure modes, it is convenient to first classify these modes based on the material constitutions of layered/reinforced structures. As shown schematically in Fig. 1, there are two major categories of failure observed in post-mortem studies. The first major failure category is decohesion (or cracking) between bonded layers at an interface. This is often referred to as delamination in composite laminates or interfacial debonding in thin films or sandwich structures. It is also called inter-layer failure. Generally, two distinct inter-layer failure modes are observed. The first one involves opening-dominated inter-layer cracking or "delamination buckling" (Gioia and Ortiz [6]; Kadomateas [7]). The second one involves shear-dominated inter-layer cracks or "shear delaminations," and often occurs in layered materials subjected to out-of-plane impact (Choi et al. [8]; Lambros and Rosakis [9]).

The second major category is referred to as intra-layer failure. There are three possible intra-layer failure modes depending on the material constitution. The first

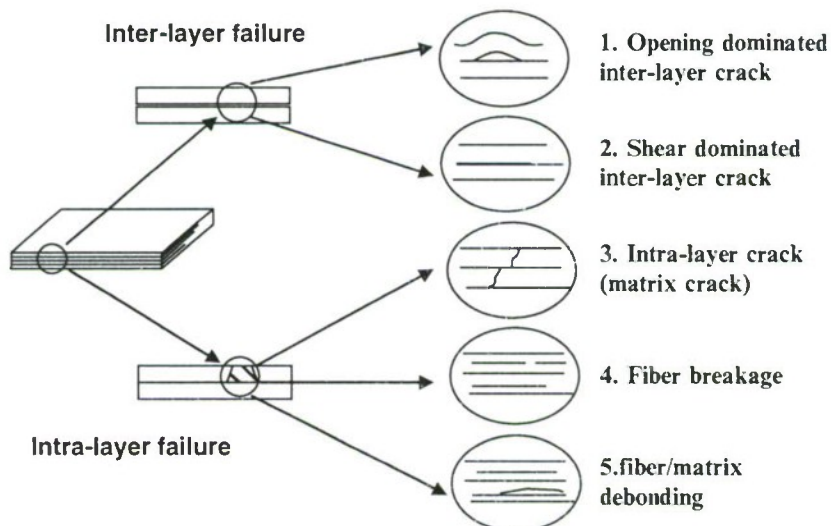


**Fig. 1** Failure modes for layered materials based on material constitution

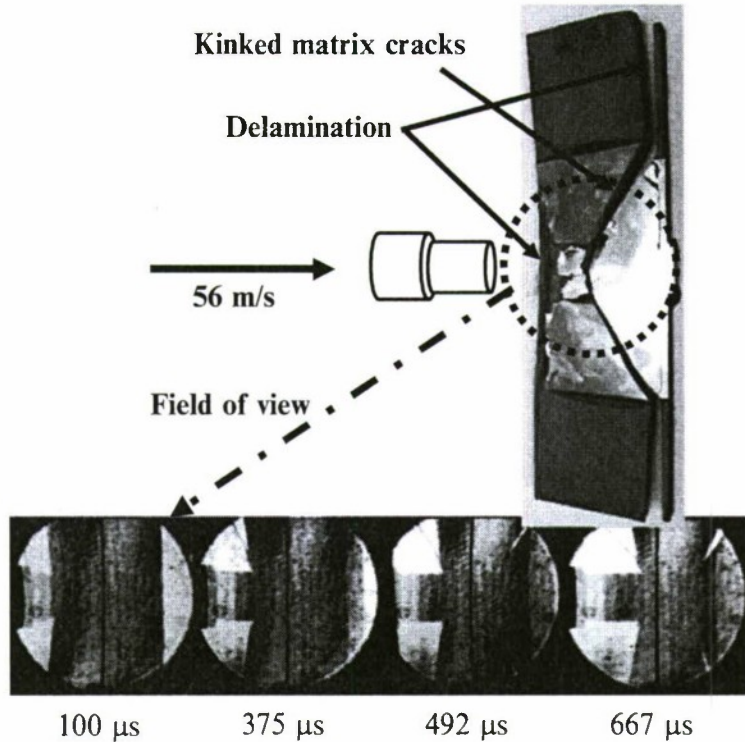


**Fig. 2** A series of back lit photos showing the dynamic failure process for a fiberglass face plates/PVC foam core sandwich structure

one is called intra-layer cracking or matrix cracking as seen in Fig. 2. This type of cracking often occurs inside the matrix of fiber-reinforced composites or within the soft core of sandwich structures [10]. It is also found in the form of tunneling cracks in thin film/substrate structures [1]. Another possible intra-layer failure is the failure of reinforcements such as fiber breakage and fiber kinking within a layer (Oguni et al. [11]). The third intra-layer failure mode is interfacial debonding between the matrix material and the reinforcement such as debonding between particle/fiber and matrix occurring within a constituent layer [12]. Indeed, the sequence, nature and interaction of these dynamic failure modes were never properly clarified.

In perhaps the first attempt to visualize impact failure in sandwich structures used in Naval applications, Semenski and Rosakis [13] tested thin sections of such plate structures composed of PVC foam cores, sandwiched between E-glass face-plates. A pulsed laser was used to illuminate the specimens from the back side and a high-speed camera recorded the deformation and failure events. A sequence of photographs corresponding to this process is shown in Fig. 2 together with the post-mortem picture of the recorded specimen. As evident from the post-mortem picture, there are, at least, two types of failure present. Inter-layer failure demonstrates itself in the form of delamination between the face plates and the foam core at the vicinity of the impact site and free edges. On the opposite side, delamination is evident only on the top and on the bottom part of the specimen. Intra-layer failure in the form of mode I, opening cracks in the soft core is also observed forming a highly

symmetric pattern. Because the core is opaque, the high-speed pictures shown below are of limited use. What they show, however, is the emergence and propagation of the opening intra-layer (matrix) cracks inside the foam core. Indeed, these cracks seem to originate at the fiber glass/PVC interface opposite to the side of impact, and to symmetrically propagate towards the impact point. These cracks originate at the same location where the fiberglass/PVC delamination terminates. However, the time sequence and interaction between such inter-layer delamination and the visible intra-layer, opening cracks in the core are not obvious. Indeed, the backlit real-time photographs do not show any evidence of interfacial delamination within the time window of observation. As we will show later, this observation is misleading and is due to the fact that inter-layer fractures are typically shear-dominated. As such they do not allow for light to go through during the recording event because the shear crack faces remain in contact at the early stages of this process.

The inability of back-lit photography to visualize the failure process completely, motivates the use of partially transparent model sandwich systems which allow the use of full field optical techniques capable of capturing the nucleation and growth of both opening and shear-dominated cracks and their transition from one mode to the other [14]. For many complex engineering problems, model experiments may prove extremely useful as intermediate steps, which reveal the basic physics of the problem and provide relatively straightforward explanations of the failure patterns observed in post-mortem observations. A successful approach was adopted by Walter and Ravichandran [15], who designed a model aluminum/PMMA/aluminum specimen to simulate and visualize the static debonding and matrix cracking process in ceramic matrix composites. In our experiments, we also adopt the same idea and introduce an appropriate intermediate model configuration. In order to simulate the difficult three-dimensional problem of the out-of-plane impact of real sandwich structures and to simultaneously preserve the essence of the failure phenomena involved, we introduce a two-dimensional, plane stress specimen, which represents a cross-sectional cut of the layered material as illustrated in Fig. 3.

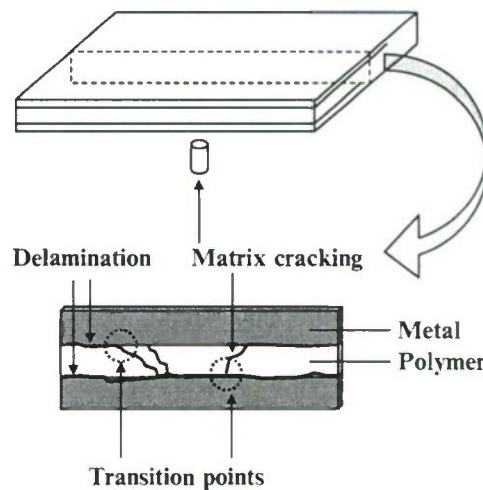


**Fig. 3** Model layered specimens are idealized cross sections of real structure subjected to out-of-plane impact

For this type of model specimen, the failure process is easy to record, visualize and analyze. It is noted that although the exact impact mechanics involved in two configurations is not identical (the real case is three-dimensional while the model specimen is closer to a plane stress state), the mechanisms of stress wave propagation and failure progression of the real and the model layered materials are quite analogous. In designing these model two-dimensional sandwich specimens, it is important to select model materials whose elastic mismatch is similar to that of materials used in real engineering applications (in our case PVC/composites). Selecting similar Dundurs' parameters [1] may ensure similarity of the elasto-static response for the interfacial mechanics problem. Meanwhile, selecting model material combinations with similar ratios of wave speeds of two constitution materials to the real structure is perhaps the most important consideration in the dynamic case, where timing of events and stress intensity are governed by the constituent material wave speeds. Also, the ratio of inter-layer and intra-layer strengths (or fracture toughnesses) is important. These three issues provide sets of similarity rules to connect the real structures to our models experiments. As schematically shown in Fig. 3, matrix cracks and delamination are the two major impact failure modes in sandwich structures and layered composites. At some intersection points, matrix cracks and delamination are connected as also seen in the post-impact picture of Fig. 2. One frequently asked question in the literature is whether the matrix cracks lead to the delamination or the delamination happens first and subsequently kinks into the adjacent layer inducing the matrix crack. This is a typical problem of sequence and failure mode transition identification.

Since the nature and origin of such failure mechanisms can only be theorized by post-mortem observations, the necessity of full-field real-time, high-speed measurements becomes obvious. To this effect, the objectives of the current work are to conduct systematic experimental studies of the time evolution and nature of different dynamic failure modes and to investigate their interactions. Through these model experiments, we try to identify the basic physical phenomena, and to provide guidance for theoretical models and much needed, real-time, validation of numerical codes. To make this comparison more meaningful, we choose model material combinations that have the ratios of wave speeds very close to those used in real sandwich structures.

## 2 Experimental Procedure

### 2.1 *Materials and Specimens*

Two kinds of materials were used in the experiments described below. A 4340-carbon steel was employed to simulate the stiff and strong fiberglass faceplates of sandwich structures. The polymeric material, which was used to simulate the weak core layer, such as the PVC foam core or balsa wood in sandwich structures or

the 90° plies in cross-ply laminates, is Homalite-100. The adhesive used to bond the metal/polymer interface is Weldon-10. The detailed properties of this adhesive and the effect of interfacial strength variation on dynamic failure mode selection are reported by Xu and Rosakis [16, 17]. The shear wave speed is an important parameter in this investigation. The shear wave speed ratio for the core and faceplate is 3.2 for typical E-glass/PVC sandwich structures of the type that have recently been used in construction of full-scale composite ships. Details on the complete set of physical and constitutive properties for E-glass composite materials have recently been discussed by Oguni et al. [11]. For comparison, the same shear wave speed ratio, for the idealized steel/Homalite model sandwiches, is about 2.7 based on the data from Ref. [14]. Although the absolute values of these constituent properties are very different in the “idealized” versus the “real” solids, the idealized material combinations have been chosen in such a way as to have a shear wave speed ratio that is very similar to its real sandwich counterparts.

As shown in Fig. 4, three different types of model sandwich specimen geometries were designed and tested. Type A specimens have equal layer widths and involve two different materials. They contain two metal layers with one polymer layer sandwiched between them. Type B specimens involve two thin metal layers (faceplates) and one polymer layer. This type of specimens is quite similar in geometry (ratio of core to face plate thickness) to realistic sandwich plates used in engineering applications. The only difference between type C and type B specimens is their lengths. Type C specimens are twice as long as type B specimens. The purpose of type C specimens is to explore the impact failure patterns with least edge effect present in the time scale of the failure process. All three types of specimens have the same out-of-plane thickness of 6.35 mm.

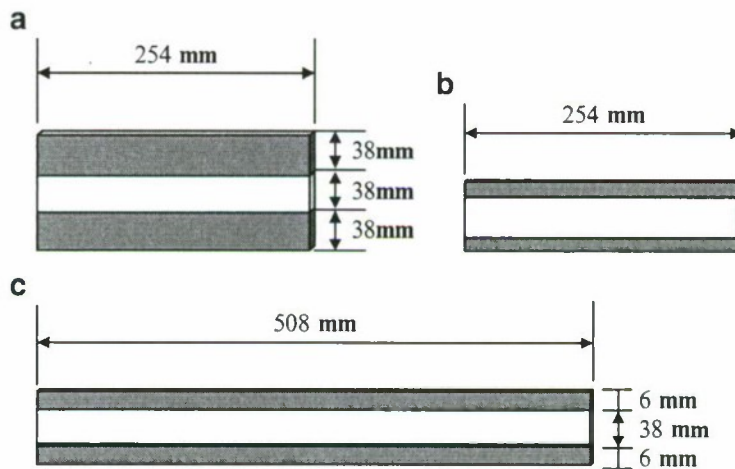


**Fig. 4** Model specimens simulating sandwich structures (*shaded layers – metals; transparent layers – polymers*)

## 2.2 Experimental Setup

The majority of experiments in this investigation were performed using dynamic photoelasticity. This classical method has recently found a lot of new applications such as study of the dynamic fracture processes in functionally gradient materials (FGMs) [18]. The Coherent Gradient Sensing (CGS) method [19] was also used in a small number of cases. A schematic of the dynamic photoelasticity setup used here is given in Fig. 5. Two circular polarizer sheets were placed on either side of the specimen. A coherent, monochromatic, plane polarized laser light output was collimated to a circular beam of 100 mm in diameter. The laser beam was transmitted through the specimen and the resulting fringe pattern was recorded by the high-speed camera. A Cordin model 330A rotating-mirror type high-speed film camera was used to record the images. During the impact test, a projectile was fired by the gas gun and impacted the specimen center. The generation of isochromatic fringe patterns is governed by the stress-optic law. For the case of monochromatic light, the condition for the formation of fringes can be expressed as [20]:

$$\hat{\sigma}_1 - \hat{\sigma}_2 = \frac{Nf_\sigma}{h} \quad (1)$$

where  $\hat{\sigma}_1 - \hat{\sigma}_2$  is the principal stress difference of the thickness averaged stress tensor.  $f_\sigma$  is the material fringe value,  $N$  is the isochromatic fringe order and  $h$  is the specimen thickness. The isochromatic fringe patterns observed are proportional to contours of constant maximum in-plane shear stress,  $\hat{\tau}_{\max} = (\hat{\sigma}_1 - \hat{\sigma}_2)/2$ .

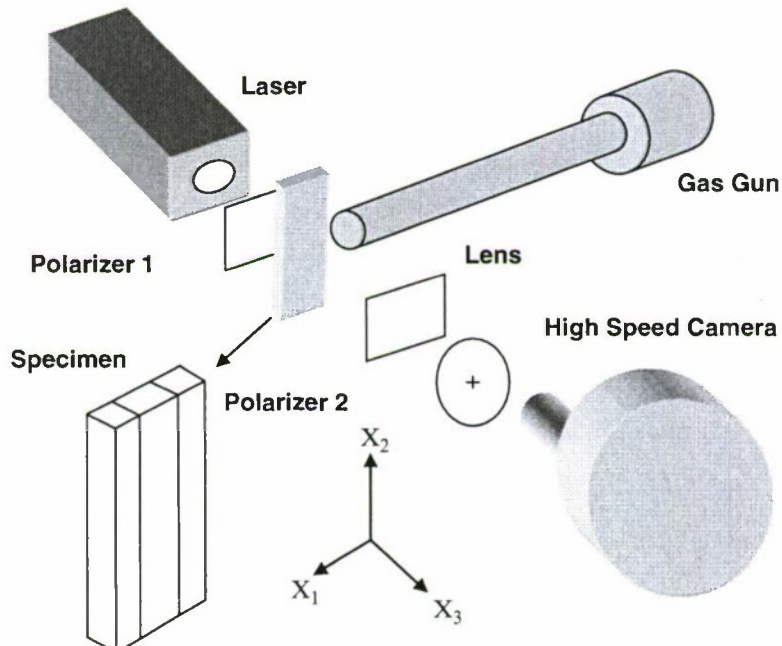


**Fig. 5** Schematic of the dynamic photoelasticity and high-speed photography setup

### 3 Results and Discussion

#### 3.1 Failure Process of Short Model Sandwich Specimens with Equal Layer Widths

The diameter of the laser beam was 100 mm; however, the maximum length of the zone that had to be investigated was 254 mm long. In order to observe all possible dynamic failure modes present in each case, the field of view had to be moved from one location to another for each specimen configuration under the same impact condition. Figure 6 presents a series of photoelastic images of the Homalite core layer of a type A specimen.

The dark circular spot at the upper right corner is a scaling mark (diameter 6.35 mm) bonded on the specimen. The thin horizontal dark line, seen around the center of every image, is the streak line of the camera. This line provides a stationary reference when the whole specimen moves during the impact process. At first, the field of view was centered on the middle of the specimen because it was close to the impact position and failure was expected to initiate from this zone. As shown in Fig. 6b, about 158  $\mu$ s after impact, two inter-layer cracks at the lower interface entered the field of view and propagated towards the specimen center. Later on (around 182  $\mu$ s), the two inter-layer cracks, identified by the moving concentration of fringes at their tips, are seen to meet each other in Fig. 6d. Similar to shear-dominated interfacial cracks in bimaterials [21], those inter-layer cracks are also shear-dominated. Because the Homalite and steel layers are still in contact up to that time, no visual evidence of decohesion is apparent in the images, although these cracks have already broken the interface in a combination of compression and shear. After these two inter-layer cracks meet at the center, a bright gap between the Homalite and steel layers can be seen to appear in Fig. 6e. Along this clearly opened interface and on the Homalite side, two Rayleigh surface waves are now seen to propagate, originating from the center and moving outwards, towards the specimen edges.

Perhaps the most interesting conclusion deriving from the sequence shown in Fig. 6 is the fact that delamination did not initiate in the interface directly above the impact point but did so outside our central field of view at two symmetric, off-axis, locations along the lower interface. In order to discover the location of crack nucleation, we must move our field of view off the specimen center to investigate the origins of these inter-layer cracks. In order to conclusively identify the origins of the upper and lower inter-layer cracks, the field of view was once more moved to the specimen edge as shown in Fig. 7a. After impact at the specimen center, the stress waves in the bottom steel layer propagated towards the edge creating a visible head wave structure on the lower wave speed polymer side (see Fig. 7b). Right after the stress wave reached the free edge, due to the existence of a stress singularity at the bimaterial corner [22, 23], an inter-layer crack initiated at the lower interface as seen in Fig. 7c. This crack propagated towards the specimen center. After around 160  $\mu$ s, another inter-layer crack initiated at the upper interface also moving towards the center. This upper inter-layer crack soon kinked into the core layer and branched into a fan of multiple mode-I intra-layer cracks. Crack branching as reported by

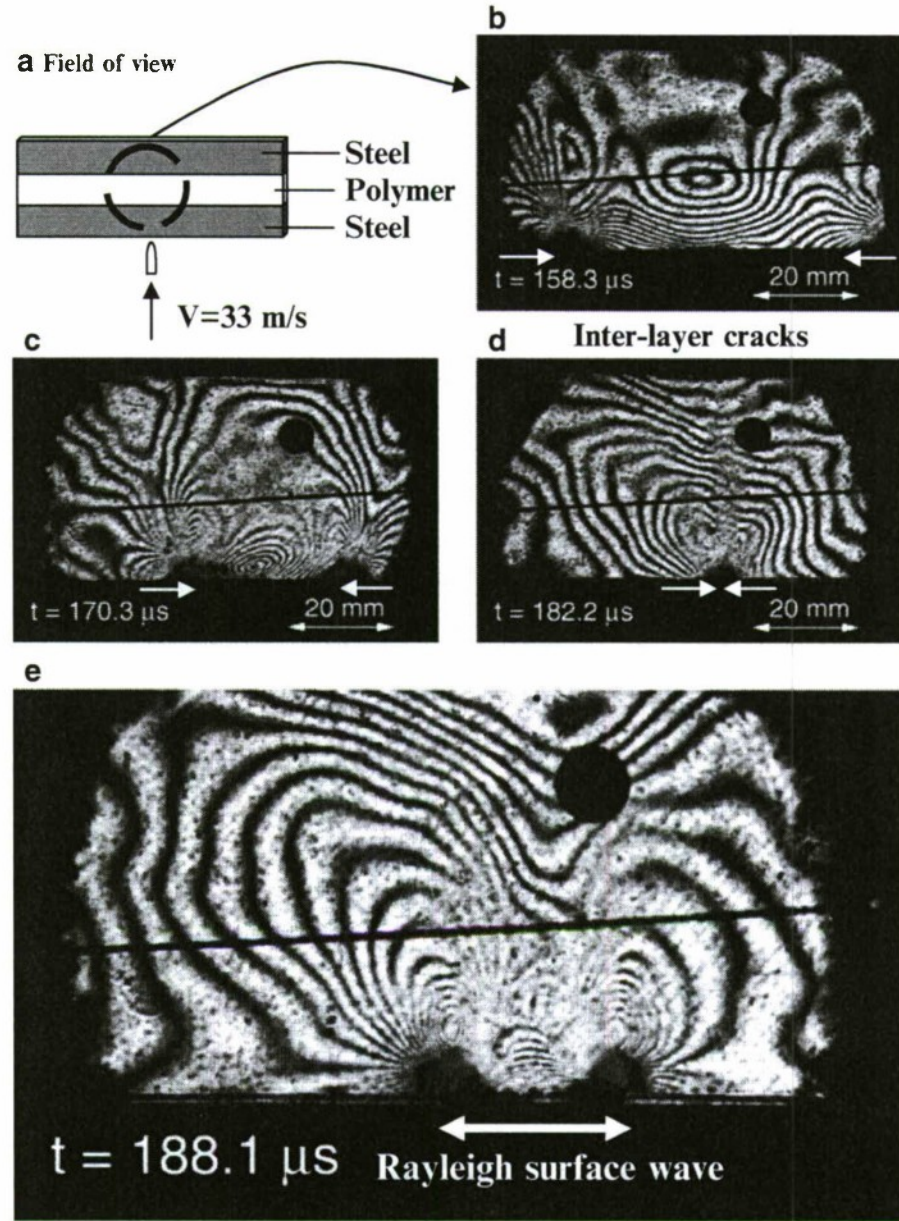


**Fig. 6** Early stages of the failure process of a three-layer specimen with equal layer widths. The central field of view reveals the early occurrence of shear-dominated delamination at the lower interface. At later times (Fig. 6e), the debonding becomes clearly visible at the lower interface

previous researchers often initiates when a crack in a homogeneous solid reaches high fractions of the shear wave speed [24], for example, 30–40% shear wave speed of Homalite-100.

Based on experimental observations from different fields of view, the major dynamic failure modes and sequence in model three-layer materials can be summarized in Fig. 8. After the stress wave reaches the free edges, two shear-dominated inter-layer cracks initiate and propagate towards the specimen center. These shear cracks separate the whole lower interface and a Rayleigh surface wave forms on the

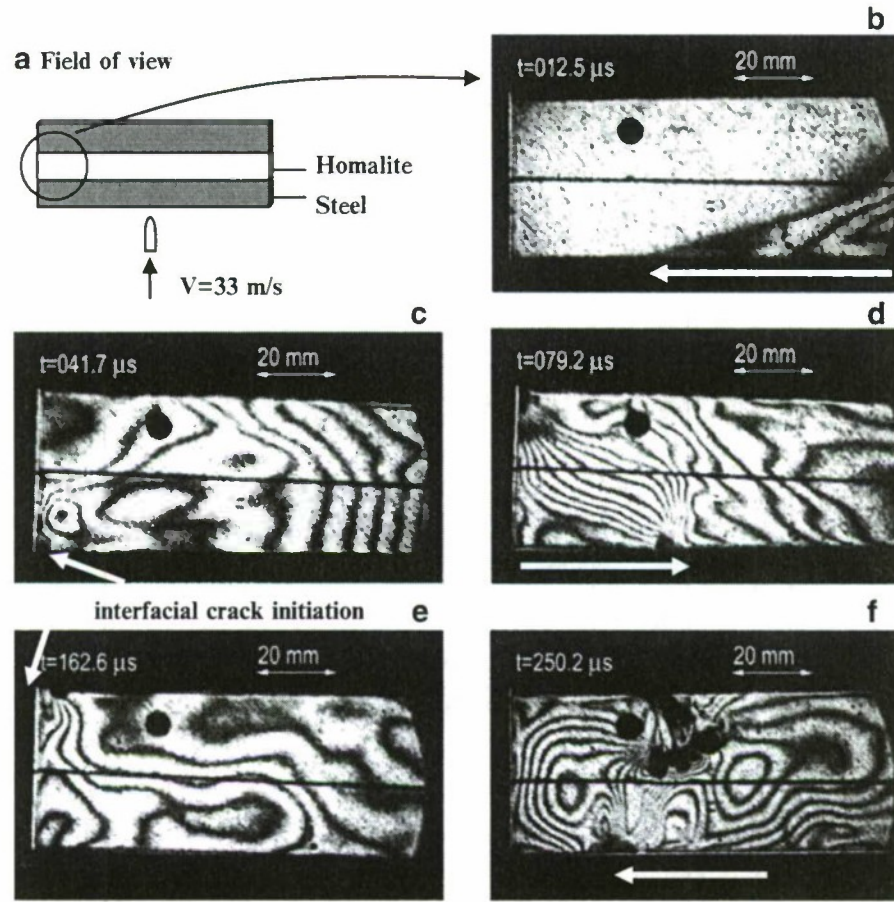


**Fig. 7** Edge view of damage evolution: delaminations are shown to form at the intersection of first lower, and then upper interfaces with the specimen edge. A fan of kinked intra-layer cracks branches into the core layer from the upper interface

separated free surface. At a later stage, inter-layer cracks also originate from the upper interface at the free edge and travel towards the specimen center. However, these upper inter-layer cracks soon kink into the core layer to form opening-dominated intra-layer cracks. Under certain circumstances (e.g., if the core material is very brittle), such kinked cracks may also branch into a fan of multiple branches fragmenting the core. The model experiments described here seem to capture the basic nature of the post-mortem impact failure modes observed in real sandwich structures. Indeed, the kinked matrix crack of the core layer of the glass fiber/foam core sandwich shown in Fig. 8e seems to follow the same initiation and propagation process as the kinked intra-layer crack in the model three-layer specimens schematically shown in Fig. 8d.

### 3.2 Failure Process in Long Model Sandwich Specimens

In type A specimens, inter-layer cracks always initiated from the specimen free edges due to the bi-material stress concentration at such locations. In order to study

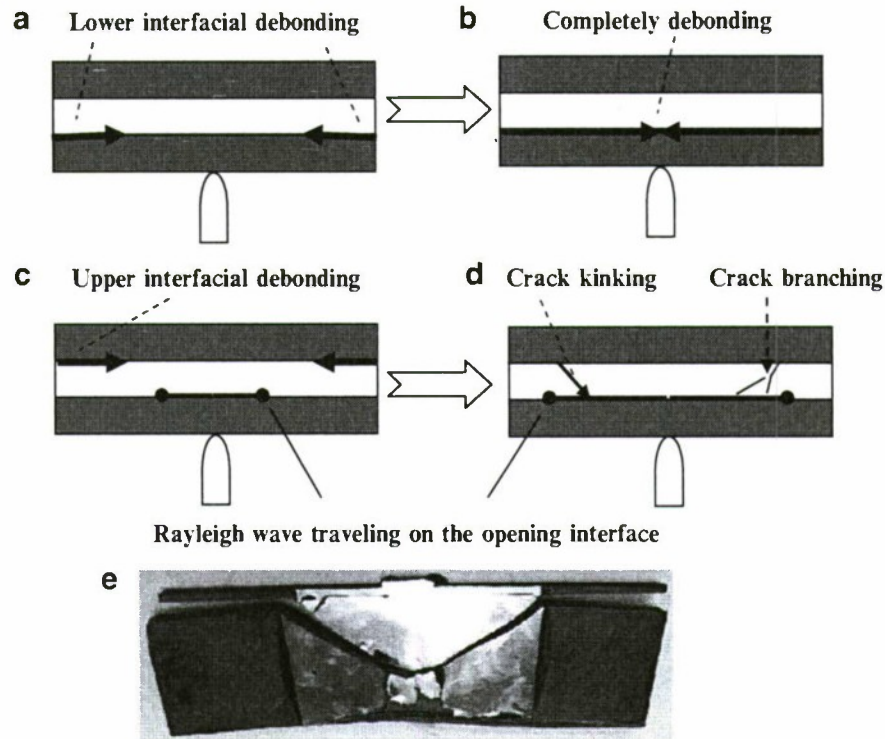


**Fig. 8** Conceptual summary of typical failure modes and sequence (a–d) in a short three-layer specimen with equal layer widths. (e) Is a comparison with a post-impact picture of a real sandwich specimen

the impact damage modes and failure sequence in either very large structures or ones that are clamped along the edges, our model specimens featured long specimens. These specimens were long enough such that any damage from the edges, such as inter-layer cracks induced by the edge effect, arrived in the area of observation long after the local damage sequence had been completed near the impact point. To study this effect, we tested long sandwich style specimens of type C (see Fig. 9).

As shown in Fig. 9d, at  $79 \mu\text{s}$  after impact, an inter-layer crack tip is seen at the lower interface (fringe concentration within the dashed circle). This crack is similar in nature to our previously observed inter-layer fractures but has not originated at the specimen free edge, which for type C specimens is far away from our field of view. Indeed, if this crack originated from the specimen free edge, it would take at least  $150 \mu\text{s}$  to enter the field of view. Closer scrutiny reveals that this crack originates from a much closer location to the impact point. This location is marked here by the circle in Fig. 9c within which a concentration of photoelastic fringes points to the concentration of shear stresses that is responsible for its nucleation. Indeed the crack nucleates at a location where the inter-layer shear stress reaches a local maximum, whose value equals the shear strength of the bond. To rationalize this, one should consider the symmetry of our impact configuration and recall the strong wave speed mismatch between the lower faceplate and the core material. The shear stress component  $\sigma_{12}$  at the specimen centerline will always vanish because of this symmetry but is expected to anti-symmetrically increase away from the centerline as compressive waves begin to spread along the steel faceplate. As a result of these

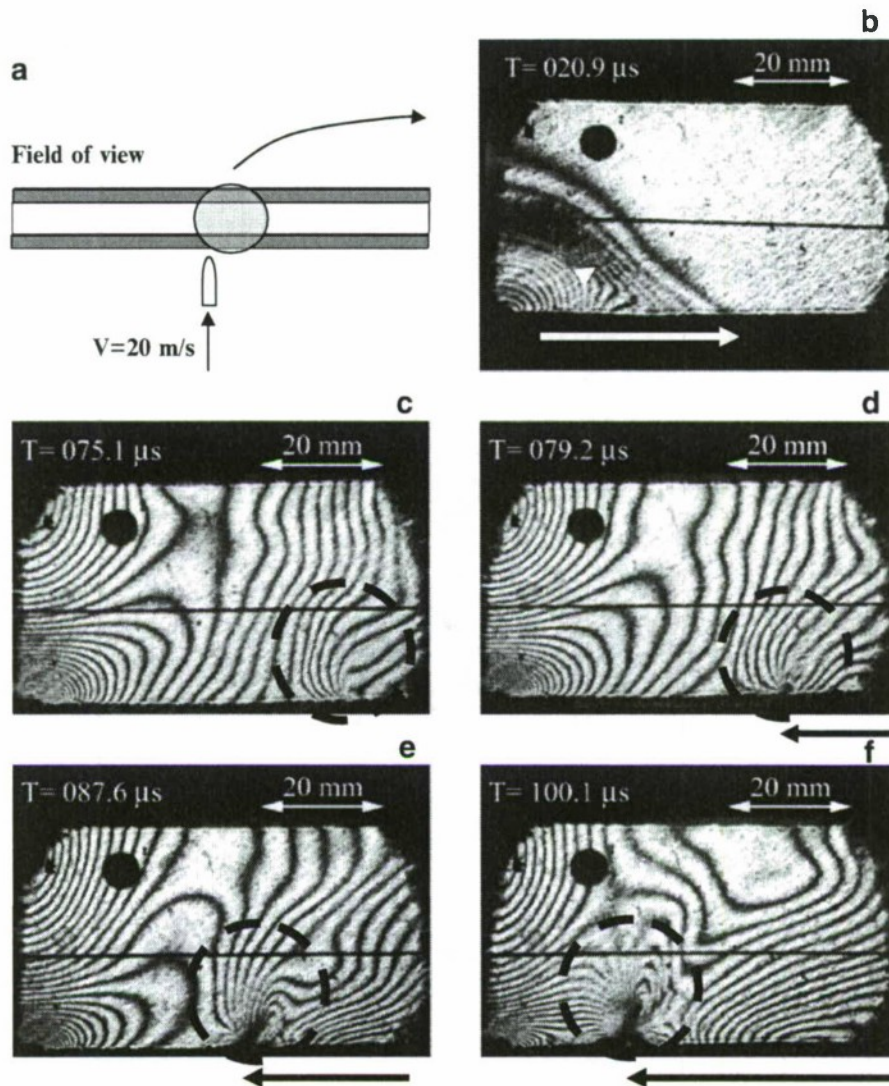


**Fig. 9** Nucleation of an intersonic inter-layer crack at the vicinity of the impact area of a long model sandwich specimen

observations, the scenario that seems to be emerging is as follows: shear-dominated cracks are generated at two points to the right and left of the center line and more backwards towards the impact point. A series of photographs confirming the existence of an inter-layer crack coming from the right-hand side of the impact point is shown in Fig. 9. Indeed Fig. 9c corresponds to the nucleation of this crack while Fig. 9d-f confirm its high-speed motion towards the impact site. As this inter-layer crack and its symmetric companion from the left meet above the impact point, they create a central shear delamination between the core and the bottom faceplate. The speed of this crack is very high as evident from the shear shock wave that appears as a dark inclined line radiating from its moving tip (Fig. 9e, f).

Figure 10 corresponds to another impact experiment which featured the same load condition as shown in Fig. 9. The end point of the central delamination

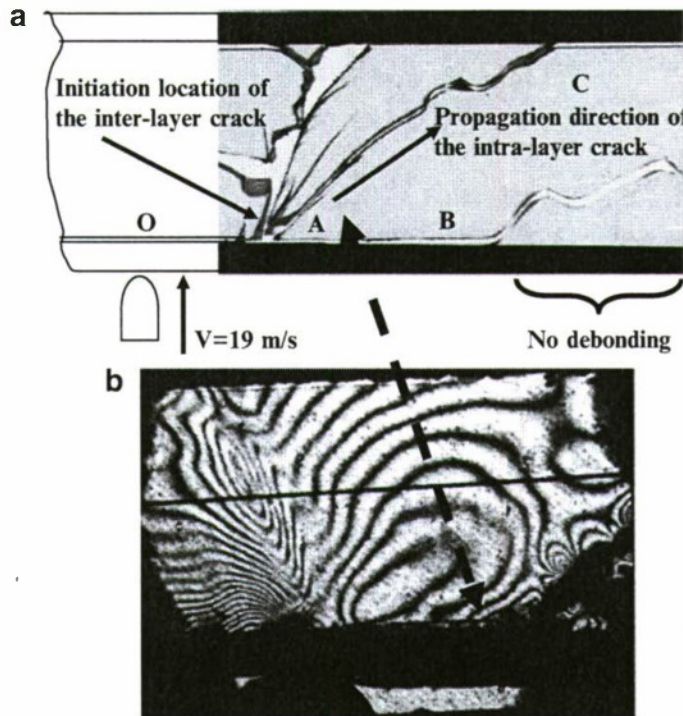


**Fig. 10** Local view of the post-mortem damage in a long sandwich specimen (a) and high-speed snap shot capturing the formation of intra-layer cracks (b)

described above is denoted by A. Yu et al. [25] show that the inter-layer normal stresses near the impact point are compressive while the inter-layer shear stresses exhibit two clear peak values (same magnitude) moving symmetrically away from the centerline. Point A in Fig. 10 is corresponding to the old location of the maximum inter-layer shear stress. This point can now act as a stress concentration from which further damage (to the core as well as to the rest of the interface) will subsequently evolve. Indeed as seen in Fig. 10, intra-layer cracks now are generated and propagated into the core (along AC), also accompanied by a new inter-layer debond (along AB) also originating at point A. The high-speed snapshot that appears in the same photograph confirms this scenario.

Figure 11 summarizes the proposed failure evolution sequence for the long sandwich style specimens described above. One point that should be made clear here is that following the formation of the central (shear) delamination, the choice of the inclination angle  $\beta$  and the possibility of further delamination along the bottom interface depend on the impact speed and on the relative values of the matrix material and interfacial bond strengths. The same is true for the exact locations of points A and B. However, we expect that if impact speeds are high enough to promote this localized failure mode, the general features described here will continue appearing even as the projectile speed increases further. For the initiation of intra-layer cracks (matrix cracks), previous researchers theorized that such cracks initiated from the center of the weak layer and propagated toward adjacent interfaces to lead to inter-layer cracks or delaminations [26]. However, no real-time experimental evidence was

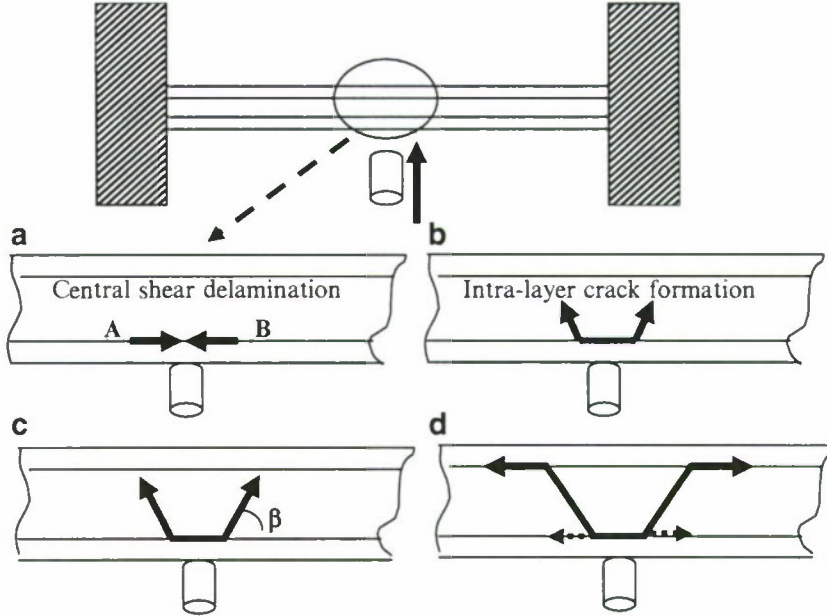


**Fig. 11** Failure sequence observed in long sandwich-style specimens with minimal edge effects

ever observed to support such a scenario. Here, we clearly show that the intra-layer cracks always initiate at the interfaces following the shear-dominated delamination, which kinks into the core layer resulting in intra-layer cracking.

### 3.3 Effect of Impact Speeds

In Section 3.1, we investigated the nature and sequence of failure mechanisms in relation to model sandwich specimens subjected to an impact speed of 33 m/s, as seen in Fig. 6. This impact speed situation will be taken as the baseline for our comparisons. Figure 12 describes an experiment of the same geometry that corresponds to an impact speed is 45 m/s [16]. As seen from Fig. 12b, two inter-layer cracks appeared at the lower interface and propagated towards the center, racing towards each other with intersonic speeds. At a later time, inter-layer cracks at the upper interface also appeared propagating towards the center (Fig. 12c). The locations of these four inter-layer cracks (two at the top and two at the lower interfaces) are indicated by the white arrows. As clearly seen from Fig. 12e, intra-layer damage also spreads from the interface in to the core in the form of a periodic series of mode-I cracks inclined at a small angle to the vertical axis. These cracks are nucleated at the upper interface at locations that are behind the horizontally moving inter-layer shear crack. Their nucleation and growth result in the eventual fragmentation of the specimen core. The inter-layer cracks propagating at the lower bimaterial interface and facing towards each other in Fig. 12d–e feature clearly formed shock-like or Mach-like discontinuities (shear shock waves) which are emitted from their crack tips. These discontinuities in photoelastic patterns represent traveling discontinuities

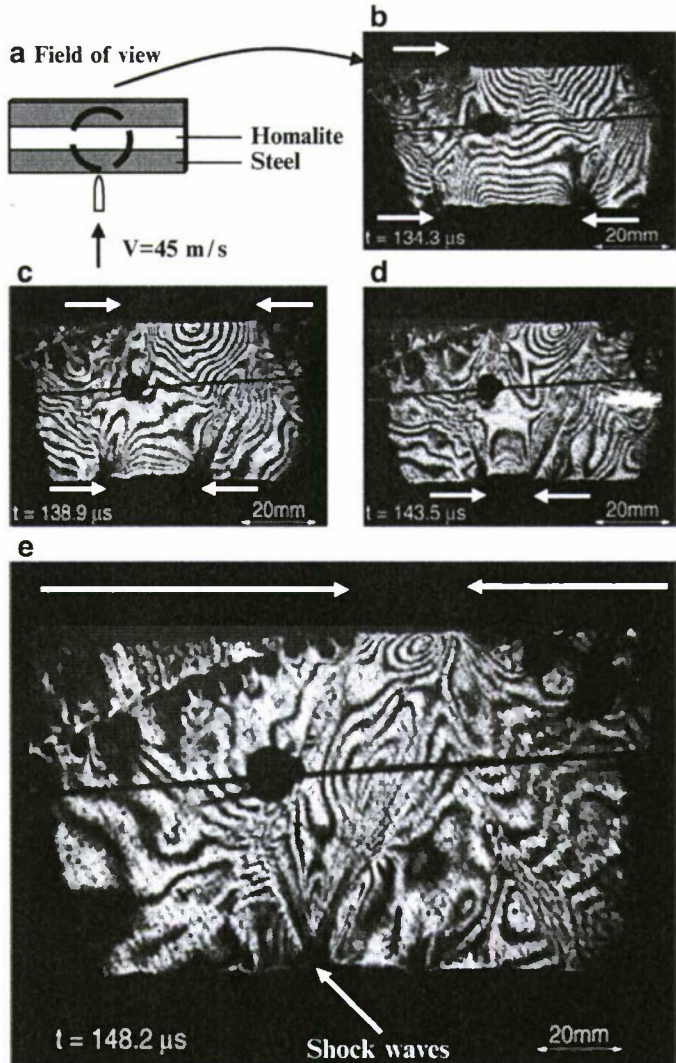


**Fig. 12** Growth of four inter-layer cracks at the center of a three-layer specimen

in maximum shear stress and are clear proofs that crack tips have exceeded the shear wave speed of Homalite [19]. These shock waves formed a clear testimony to the intersonic nature of the inter-layer crack growth even before any detailed crack measurement was ever attempted. The crack speed history for the lower, right inter-layer crack is plotted in Fig. 13 as a function of distance from the free edge. The figure shows that the crack speed of the higher impact speed case (45 m/s) is always higher than the baseline equivalent remaining always intersonic within the window of observation.

### 3.4 Dynamic Failure Mode Transition

From the above experimental observation, we find that different dynamic failure modes and their transition are very interesting. As seen in Fig. 11b, an interface

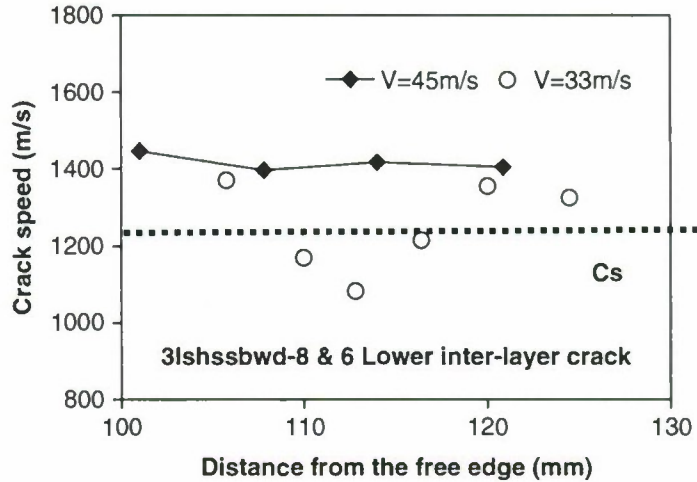


Fig. 13 Comparison of crack speed distributions of two identical specimens subjected to different impact speeds. The *dash line* is the dynamic shear wave speed of the Homalite-100

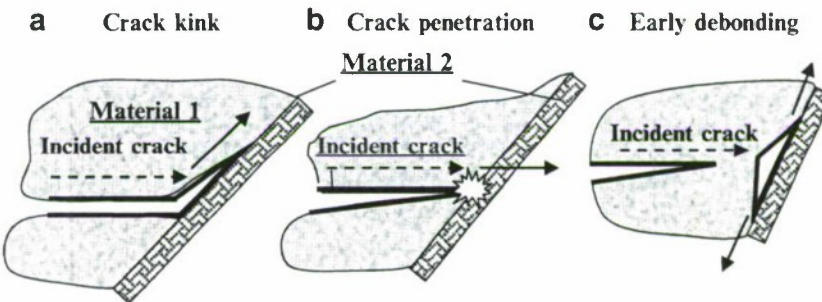


Fig. 14 Common failure modes when a crack encounters an interface

crack kinks from the interface to form a matrix or intra-layer crack. While this matrix/intra-layer will deflect at the second interface to form a inter-layer crack again. Generally, when a crack propagates in elastic solids and encounters an interface, one of the three situations may occur as seen in Fig. 14: (a) after the crack reaches the interface, it kinks out of its original path and continues to propagate along the interface [27]. This phenomenon is often called “crack kinking or deflection” [28]; (b) the crack penetrates the interface and continues to propagate along its original path, i.e., crack penetration [29, 30]; (c) early interface debonding initiates before the incident crack reaches the interface, or it refers to the “Cook-Gordon mechanism” [31–33]. In the open literature, efforts have been primarily focused on analyzing the first two cases, crack kinking and crack penetration [1]. The energy release rate ratios of the incident and kinked interfacial cracks, and the fracture toughness ratios of the matrix material and the interface are identified as major parameters to govern crack deflection/penetration [34].

Recently, Xu et al. [30] experimentally and analytically studied the dynamic crack deflection/penetration phenomena. They also presented an energy-based

criterion to investigate the competition between the dynamic crack penetration and deflection. The criterion for interfacial dynamic crack kinking is a ratio comparison between two energy release rates for the deflected/kinked crack along the interface, and the incident crack inside the matrix (driving force) and the fracture toughness values (material resistance):

$$\frac{G^d(\beta, v_2)}{G_I^P(v_1)} \geq \frac{\Gamma_c^{IT}(v_2)}{\Gamma_{Id}^{MA}(v_1)} \quad (2)$$

where  $\beta$  is the crack kinking angle or interface angle, and  $v_1$  and  $v_2$  are the incident parent crack speed and the kinked daughter crack speed respectively (Freund [40]).  $\Gamma_{Id}^{MA}(v_1)$  is the dynamic fracture toughness of the matrix material and  $\Gamma_c^{IT}(v_2)$  is the interfacial fracture toughness. If the left side is less than the right side, a dynamic crack penetration will occur.

However, in order to apply the energy-based criterion, putative crack deflection and crack penetration lengths are needed to evaluate the corresponding energy release rates. Several researchers [29, 35] have demonstrated that the two putative lengths have a significant effect on the energy release rate ratios, and sometimes the energy-based criterion fails to predict the crack deflection or crack penetration. For these cases, “Cook-Gordon mechanism” provides an alternative explanation since a crack may not kink right after it reaches the interface as shown in Fig. 14a. The case (interface debonding before kinking) shown in Fig. 14c is quite possible.

### 3.5 Dynamic Interface Debonding Ahead of a Main Incident Crack

In Fig. 14c, correlations of the fracture mechanics parameters of the kinked interfacial crack and the incident crack are not easy to obtain. Therefore, in order to model the “Cook-Gordon mechanism”, we tend to use strength-based criteria to predict interfacial debonding initiation only (rather than crack growth) induced by an incident crack. In terms of the dynamic “Cook-Gordon mechanism”, only Needleman and co-workers [36–38] have simulated this problem using a cohesive element model. In their model, an artificial initial flaw was introduced so they assumed some material properties for predictions. In our investigation, a strength criterion with direct interfacial strength measurements will be used to predict the critical distance  $r_c$  of the incident crack tip to the intersection point of the incident crack path and the interface. Indeed, our work will be complementary to Needleman’s work, since our work aims to predict interfacial debonding initiation, while their efforts were focused on simulating the late interfacial crack propagation after crack initiation.

Figure 15 shows a series of photoelasticity snap shots following impact of a bonded Hormalite specimen [33]. In all experiments, the projectile impacted the center of the bottom layer on a steel buffer as shown in Fig. 15a. Figure 15b shows a fan of mode I cracks (symmetric fringe patterns) appearing from the upper free edge

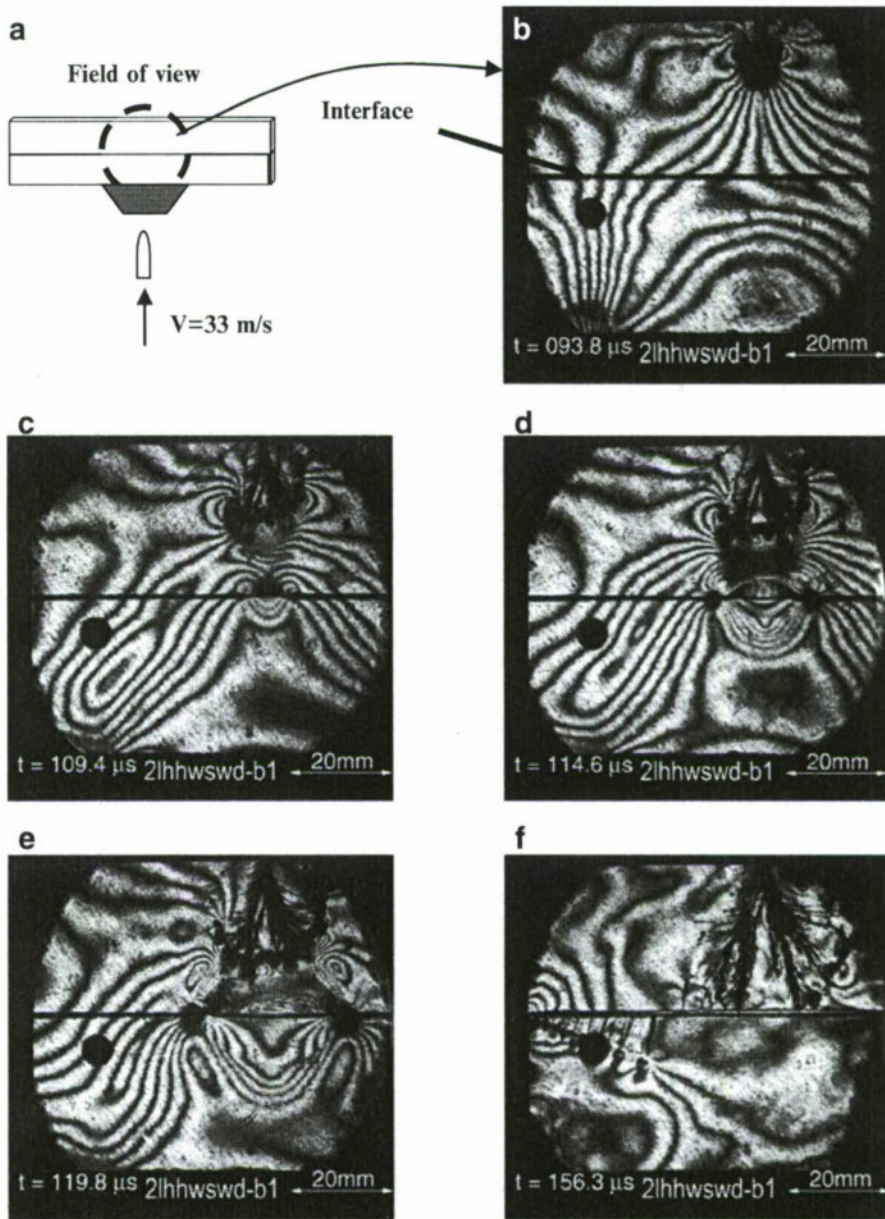


**Fig. 15** Dynamic failure process in a two-layer specimen showing the interaction of a fan of mode I incident cracks and the resulting interfacial crack. The *thin horizontal line* is the weak interface

at approximately  $93.8 \mu\text{s}$  after impact. After impact, the longitudinal compressive stress wave traveled from the lower impact side towards the upper free edge.

This compressive stress wave reflected from this edge as a tensile wave and its intensity was sufficient to nucleate a fan of branched cracks from the free edge. As time goes on (Fig. 15c-f), the nucleated fan of cracks widens significantly by producing a multiplicity of both successful and unsuccessful branches, some of which move towards the still coherent interface (for a discussion of crack branching phenomenon in bulk Homalite, see Ravi-Chandar and Knauss [24]. The average speed

of these locally mode I, branched cracks is  $0.41 C_S$ , which is the branching speed in bulk Homalite. Well before the branched cracks reached the interface, a central inter-layer crack was nucleated at the intersection of the specimen center line and the bond line as seen in Fig. 15c. This interfacial crack propagated in both directions off the center as shown in Fig. 15d. At the specimen centerline, the shear stresses vanish because of symmetry. As a result, the nucleated inter-layer crack is initially and, for a very short time, mode I dominated. Its nucleation is induced by the stress field produced by the fan of branched cracks approaching the interface. As this crack spreads symmetrically, opening up the interface (see distinct evidence of decohesion in Fig. 15f, the fan of branched cracks decelerates and arrests just before these cracks reach the decohered interface. The above described scenario is perhaps the first real-time visualization of the dynamic equivalent of the “Cook-Gordon Mechanism” describing the remote decohesion of an interface due to the approach of a matrix (intra-layer) crack. As the interfacial crack spreads away from the specimen centerline, it almost immediately encounters increasing amount of interfacial shear stress, which quickly converts it to a mixed-mode and eventually to a mode II dominated crack. Unlike propagating cracks in bulk Homalite, interfacial cracks are constrained to propagate along the weak interface and, as a result, they can do so under mixed-mode or primarily mode II conditions. They can also propagate at very high (even intersonic) speeds compared to their bulk (intra-layer) counterparts. In order to predict the dynamic crack initiation, Wang and Xu [27] proposed a strength criterion

$$(\sigma'_{22}/\sigma_t)^2 + (\sigma'_{12}/\sigma_s)^2 = 1 \quad (3)$$

where  $\sigma_t, \sigma_s$  are the interface tensile and shear strengths,  $\sigma'_{11}, \sigma'_{12}, \sigma'_{22}$  are stresses acting on the interface which are induced by an incident dynamic crack close to the interface. The stress field of a steady mode I crack inside a linear elastic solid is given by a well-known form [39, 40]:

$$\sigma_{ij}^I = \frac{K_I(t)}{\sqrt{2\pi r}} \Sigma_{ij}^I(\theta, v) + T \delta_{i1} \delta_{j1} + O(1) \quad (4)$$

where  $K_I(t)$  is the dynamic stress intensity factor of the mode I crack as a function of time  $t$ ;  $T$  is a non-singular term, which is called “the T-stress” or  $\sigma_{ox}$  [20];  $O(1)$  represents higher order terms; the functions  $\Sigma_{ij}^I(\theta, v)$  that represent the angular variation of stress components for an instantaneous crack tip speed  $v$ . For the kinked/deflected interface crack, it is a mixed-mode crack with a stress field:

$$\begin{aligned} \sigma_{ij} &= \sigma_{ij}^I + \sigma_{ij}^{II} \\ &= \frac{K_I(t)}{\sqrt{2\pi r}} \sum_{ij}^I(\theta, V) + T \delta_{i1} \delta_{j1} + \frac{K_{II}(t)}{\sqrt{2\pi r}} \sum_{ij}^{II}(\theta, V) + O(1) \end{aligned} \quad (5)$$

where  $K_{II}(t)$  is the dynamic stress intensity factor of the mode II crack as a function of time  $t$  and the functions  $\Sigma_{ij}^{II}(\theta, v)$  represents the angular variation of stress components for an instantaneous crack tip speed  $v$ .

### 3.6 New Progress on Dynamic Crack Branching

As observed in the above dynamic failure experiments, we find that dynamic crack branching is an important dynamic failure mode for brittle materials, and for ductile materials subjected to certain conditions. This phenomenon has received extensive attention in the past decades. However, previous major efforts have primarily focused on analytical and numerical studies [41–43]. Very few new experimental results were available to verify predictions or to provide guidance for modeling [24, 44]. Some important issues, such as the crack speed change before and after branching, effect of dynamic loading rate on the crack branching, and crack branching induced by stress wave loading are still open. Therefore, we try to focus on how to realize various forms of dynamic crack branching under a variety of conditions [45]. The objectives are to elucidate a series of new phenomena; and to provide guidance for developing theoretical models and validating numerical simulations.

#### 3.6.1 Special Experiments for Dynamic Crack Kinking and Branching

Two kinds of polymeric materials were used in conjunction with two kinds of optical diagnostic techniques. Homalite-100 was chosen for the photoelasticity experiments while PMMA was used in the Coherent Gradient Sensing experiments. Various types of specimens were designed and some of them had pre-notches with different radii. One major specimen used in this investigation was a novel wedge-loaded specimen, which was designed to produce a single, straight dynamic crack as shown in Fig. 16a. An aluminum wedge was inserted into a pre-notch and impacted by a projectile, causing the wedge to open the notch faces thus producing a single mode I crack [30]. The notch tip was cut using a diamond afering blade (Buehler, Series 15 LC). A strain gauge was bonded onto the wedge to trigger the high-speed camera and laser system.

#### 3.6.2 Dynamic Crack Branching and Kinking from a Weak Interface

As shown in Fig. 16, the in-plane Homalite specimen dimensions were 457 mm long, 254 mm wide and the plate thickness was 9.5 mm. In this photoelasticity experiment, the initial notch radius was 0.127 mm (0.005 in.). For a low impact speed,  $V = 19 \text{ m/s}$ , only a pure mode I crack initiated from the notch. As seen in Fig. 16b, we created an artificial interface (an inclined thin line) in front of the horizontally propagating crack. The incident mode I crack approached the interface at about  $151 \mu\text{s}$  after impact and transitioned into a mixed-mode interfacial crack. A vertical line appearing in every image is the camera streak line, which was used for positioning and reference purposes.

At approximately  $177 \mu\text{s}$ , this mixed-mode interfacial crack kinked into the right side of the interface. A significant caustics (or shadow spot) is seen in Fig. 16d to show the mode I nature of the kinked crack. The speed of the kinked crack was

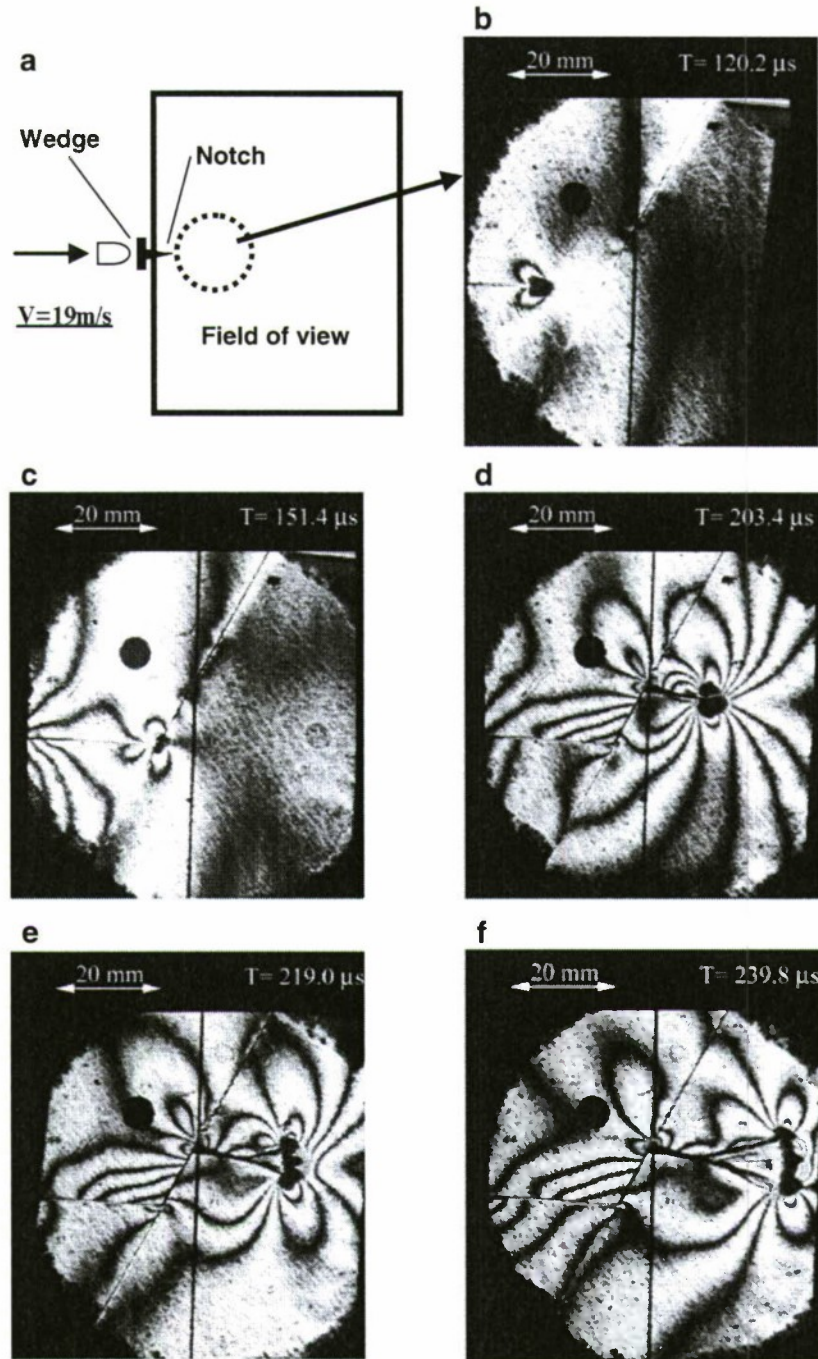


**Fig. 16** Formation and propagation of branched cracks kinked from an interfacial crack

high enough to induce multiple branches, which are visible in Fig. 16e, f. Crack length and speed records of the main crack and the branched cracks are presented in Fig. 17. Differentiation of the crack length record furnishes the tangential crack tip speed before and after crack branching. Since the differentiation process is based on a three-point-fitting procedure of the crack length history, the exact crack speed at the crack branching could not be obtained. However, it is interesting to notice that

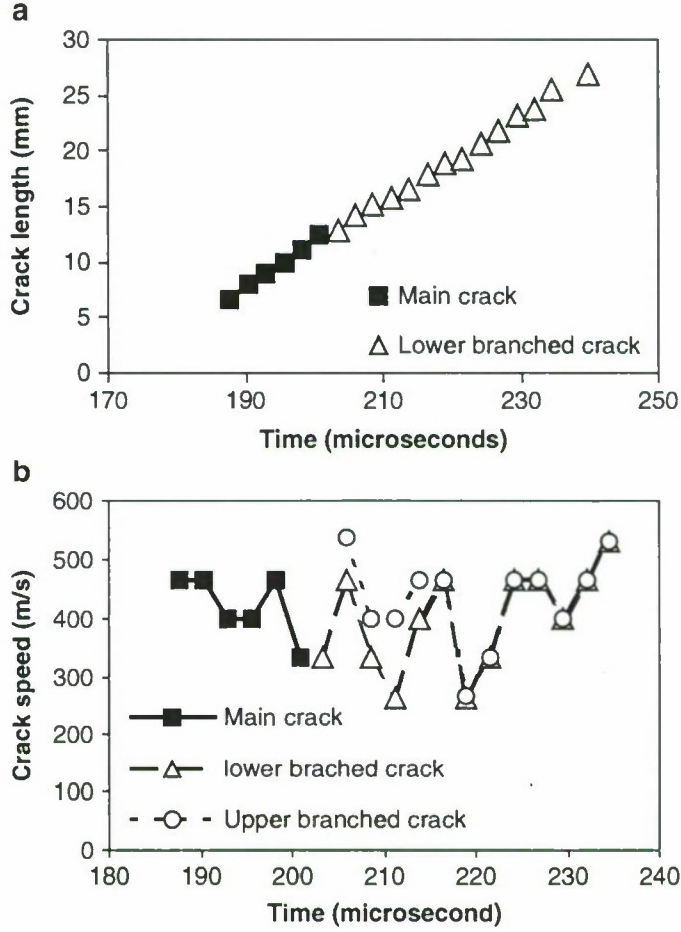
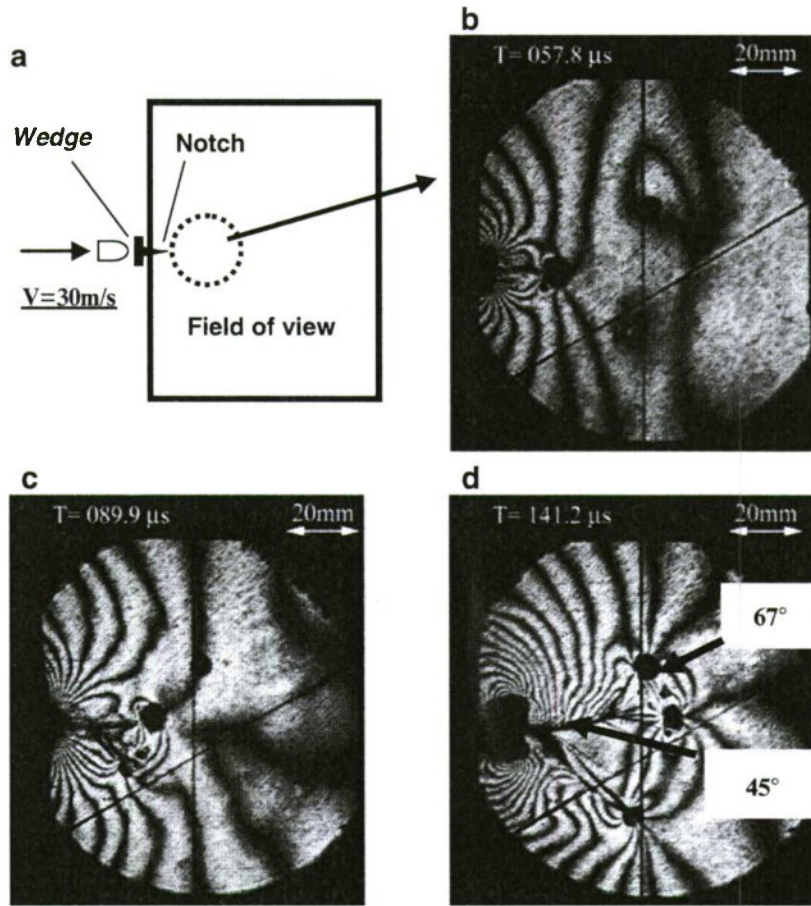


Fig. 17 Crack length history and fitted crack tip speeds of the main crack and the branched cracks

the main crack tip speed is almost equal to the branched crack tip speed under the current time resolution ( $2.6 \mu\text{s}/\text{frame}$ ). The crack branching speed was about 28% of the shear wave speed of Homalite at the high strain rate.

### 3.6.3 Dynamic Crack Branching Initiated from a Notch Subjected to High Impact Loading

If we kept all other conditions from the previous case but raised the impact speed to 30 m/s (58% increase), a mode I crack was observed at first as shown in Fig. 18b. However, this main crack soon branched into two cracks as seen in Fig. 18c. At a later time, one branched crack (upper branch) generated two new sub-branching cracks shown in Fig. 18d. Previous experiments reported that the branching angle was less than  $45^\circ$  [20, 46]. However, in our experiment, the first branching angle is around  $45^\circ$  and the second branching angle is about  $67^\circ$ , which is approximately the theoretical branching angle ( $60^\circ$ ) first reported by Yoffe [41]. The mechanism of



**Fig. 18** Crack branching after a mode I crack initiation if the notch radius was small but impact loading was high

crack branching subjected to a high loading (impact) rate can be explained using the dynamic energy release rate (driving force). The availability of kinetic energy due to high impact speed tends to create more fracture surfaces for absorbing energy. Therefore, branched cracks easily occur in a high impact loading case.

### 3.7 Dynamic Crack Kinking and Penetration at an Interface

#### 3.7.1 Weak Interfaces with Different Interfacial Angles

We define a weak interface if the strength or toughness of this interface is much less than that of the strength or toughness of the bulk material (here is Homalite). The dynamic crack kinking phenomenon as shown in Fig. 16 will be slightly different if the interface crack is changed. For the case of the interfacial angles of  $45^\circ$  [30], the incident crack reached the interface around  $153\text{ }\mu\text{s}$  after impact as seen in Fig. 19a.

It is observed that the symmetric fringe pattern of the incident mode-I crack disappeared as soon as the crack deflected into the interface. The shape of the

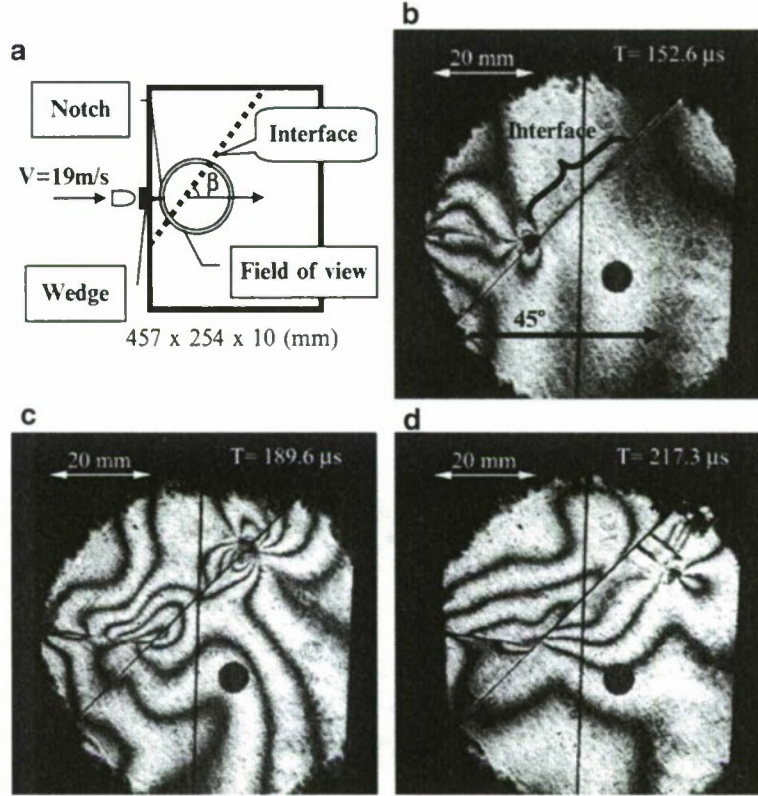


**Fig. 19** Crack deflection process at a weak interface (interface angle  $45^\circ$ )

fringe pattern of Fig. 19b suggests that this interfacial crack is shear-dominated at the latter propagation stage. In Fig. 19c, it is interesting to observe that after this shear-dominated crack propagated some distance along the interface, some secondary cracks formed at one side of the interface. These secondary cracks are locally mode-I and form on the tension side of the sheared interface.

They form after the dominant crack has propagated along the interface and thus after the interface has already failed in shear. These types of secondary cracks that are a by-product of the shear crack growth along interfaces have already been observed experimentally and are always associated with dynamic shear-dominated crack growth along weak interfaces. As the interfacial angle is changed to  $60^\circ$ , the dynamic crack deflection behavior is slightly altered, as seen in Fig. 20 on the crack speed records.

First, we notice the crack speed jump across the interface at about  $150 \mu\text{s}$ . Obviously, the initial interfacial crack speed of  $700 \text{ m/s}$  is much higher than the incident crack speed which is about  $400 \text{ m/s}$  for the interfacial angle  $60^\circ$  case. However, the interfacial crack speed reduced to  $350 \text{ m/s}$  soon after the interfacial crack kinked into the right side of monolithic Homalite (Fig. 16d). The experiment also suggests that just before the crack kinking, there was a brief crack speed reduction characteristically seen in several failure mode transition experiments [45]. In Fig. 20, the comparison of the crack speed history is made for two different interfacial angle cases. It is noticed that the interfacial crack speed for the interfacial angle  $45^\circ$  case

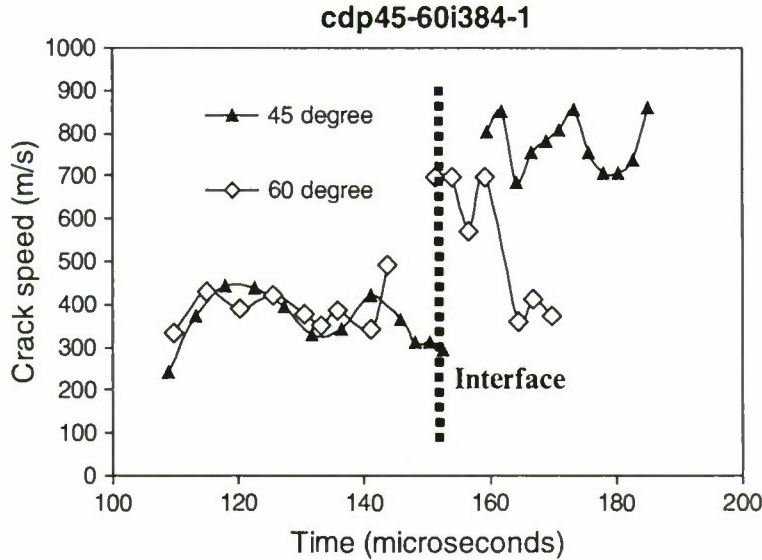


**Fig. 20** Crack speed history before and after crack deflection at a weak interface (for interfacial angles 45° and 60°)

is always higher than the crack speed for the interfacial angle 60° case. This experimental phenomenon was analyzed by the proposed dynamic fracture mechanics model [30].

### 3.7.2 Modeling of Dynamic Failure Modes Across an Interface

For the incident crack, we may use dynamic fracture mechanics theory [40] to fit the stress intensity factors  $K_I^d$ ,  $K_{II}^d$  and the T stress of the incident crack. Then, we can predict the key parameters of the kinked interfacial crack using fracture mechanics theory [47]. Our first step is to obtain the static counterparts of the dynamic stress intensity factors. After crack deflection, the static stress intensity factors of the kinked crack can be calculated using these relationships. Let  $K_I^{sk}$ ,  $K_{II}^{sk}$  denote static mode-I and mode-II stress intensity factors for the deflected (kinked) mixed-mode crack, and they are related to the static stress intensity factors of the incident dynamic cracks as a function of the kinking angle  $\beta$  [1,48]:

$$\begin{aligned} K_I^{sk} &= c_{11} K_I^s + c_{12} K_{II}^s \\ K_{II}^{sk} &= c_{21} K_I^s + c_{22} K_{II}^s \end{aligned} \quad (6)$$

where the coefficients are:

$$\begin{aligned} c_{11} &= \left( \frac{3}{4} \cos \frac{\beta}{2} + \frac{1}{4} \cos \frac{3\beta}{2} \right) & c_{12} &= -\frac{3}{4} \left( \sin \frac{\beta}{2} + \sin \frac{3\beta}{2} \right) \\ c_{21} &= \left( \frac{1}{4} \sin \frac{\beta}{2} + \frac{1}{4} \sin \frac{3\beta}{2} \right) & c_{22} &= \left( \frac{1}{4} \cos \frac{\beta}{2} + \frac{3}{4} \cos \frac{3\beta}{2} \right) \end{aligned} \quad (7)$$

Let  $K_I^{dk}$ ,  $K_{II}^{dk}$  be dynamic mode-I and mode-II stress intensity factors for the deflected (kinked) mixed-mode crack. We still assume that the universal relation between the dynamic and static stress intensity factors also holds for the deflected crack tip, i.e.,

$$\begin{aligned} K_I^{dk} &= k_I(v_2)K_I^{sk} \\ K_{II}^{dk} &= k_{II}(v_2)K_{II}^{sk} \end{aligned} \quad (8)$$

where  $k_I(v_2)$  and  $k_{II}(v_2)$  are universal functions of the crack tip speed defined by Freund [40]. Based on the above relations, if we know the dynamic stress intensity factors, the crack tip speed of the incident crack, the kinking angle as well as the crack tip speed of the kinked crack, we can get the dynamic stress intensity factors of the kinked crack and hence the crack tip stress fields around the deflected crack using Eq. 7. Then, the fringe patterns of the interfacial crack at the moment of crack deflection can be predicted using Eqs. 1 and 5. Because it is very hard to record the exact moment of crack kinking at the interface in dynamic fracture experiments, average values of the stress intensity factors of the incident crack were used to calculate the stress intensity factors of the kinked interfacial crack.

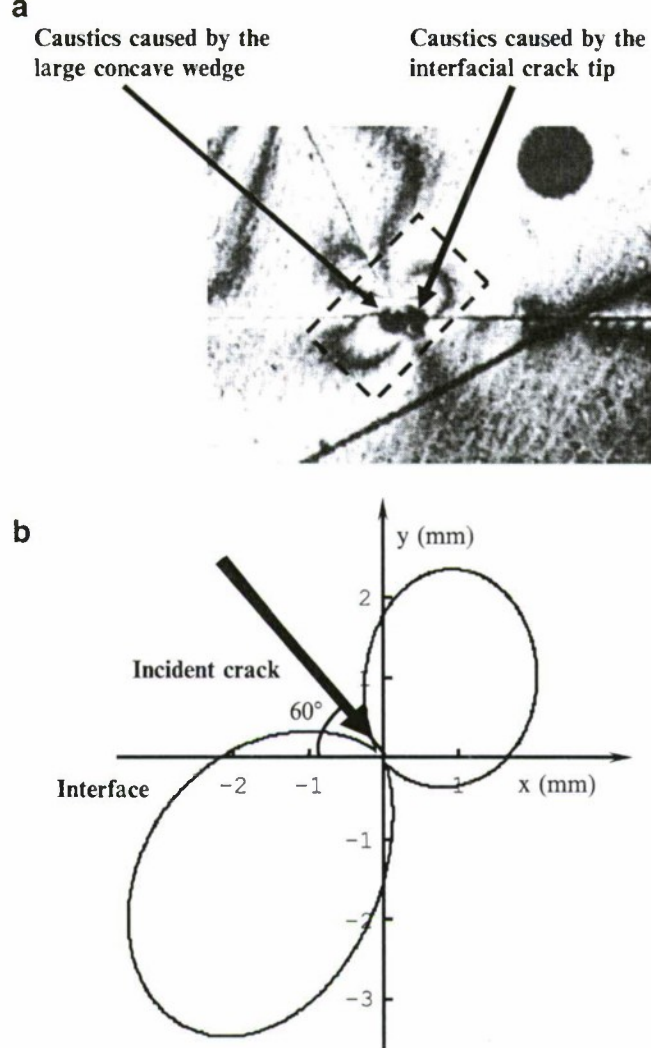
Figure 21 shows the predicted fringe pattern of a kinked interfacial crack (interfacial angle 60°). The coordinate origin is located at the intersection point of the incident crack and the kinked crack, and its x-axis is along the interface. For this case, the crack tip speed of the incident crack was around 400 m/s.

Right after crack kinking, the interfacial crack tip speed was about 700 m/s [30]. Since the T-stress of the incident crack is around 1 MPa, and there are no accurate results for the T-stress of the kinked crack [49], the T-stress of the kinked crack was assumed to be zero in all our predictions. In order to highlight our comparison of the predicted and experimental fringe patterns, only fringe order 1 was plotted. Figure 21a presents the experimental fringe showing the transition from an incident crack to an interface crack (the horizontal line was the interface). Figure 21b showed the predicted fringe and the two kinds of photoelasticity fringes were very similar so our dynamic fracture mechanics modeling and assumptions were reasonable. However, some discrepancy is also noticed because it is very hard to take one photo at the right time and right position as the theoretically predicted one.

One interesting observation is the large concave wedge effect. As seen in Fig. 21a, two caustic spots (one caused by the kinked crack tip and the other due to a large concave wedge) were clearly observed when a mode-I incident crack kinked along a weak interface with a large kinking angle (60°, see the same photo in Fig. 16c).

In most previous crack kinking analyses, researchers only considered the singular stress field due to a kinked daughter crack and ignored the singular stress field of a concave wedge. Interestingly, William's classical solution of wedge stress singularities [22] is the foundation of the full-field stress field of a traction-free crack in Linear Elastic Fracture Mechanics. Indeed, Cotterell and Rice's classical work mainly deals with a slightly kinked crack, not a large kinking angle case [50]. To authors' knowledge, only Azhdari and Nemat-Nasser provided a simple explanation to this phenomenon for a static crack kinking case [51].

**Fig. 21** Comparison of (a) experimental fringe (strong interface) and (b) predicted fringe pattern ( $v_1 = 400 \text{ m/s}$ ,  $v_2 = 700 \text{ m/s}$ ,  $N = 1$ , interfacial angle  $60^\circ$ )



### 3.7.3 Mode Mixity of the Kinked Interfacial Crack

Mode mixity is an important parameter in interface fracture analysis. It is the ratio measure of the mode II stress intensity factor/energy release rate over its mode I counterparts. There were numerous studies on mode mixity in static fracture cases but very few results were reported in dynamic fracture investigation [52, 53]. Indeed, mode mixity is a key parameter in controlling failure mode transitions along interfaces. In this investigation, when the incident mode I crack reached the interface, it kinked along the interface and became one mixed mode crack. Based on Eq. 7, for the kinked interfacial crack, its mode mixity depends on the kinked crack tip speed and the interfacial or kinking angle. Obviously, the dependence on the dynamic mode mixity on the crack tip speed is a special phenomenon in dynamic fracture mechanics. The variations of the mode mixity with the interfacial angle and the kinked crack tip speed are plotted in Fig. 22. It is not surprising to see that when

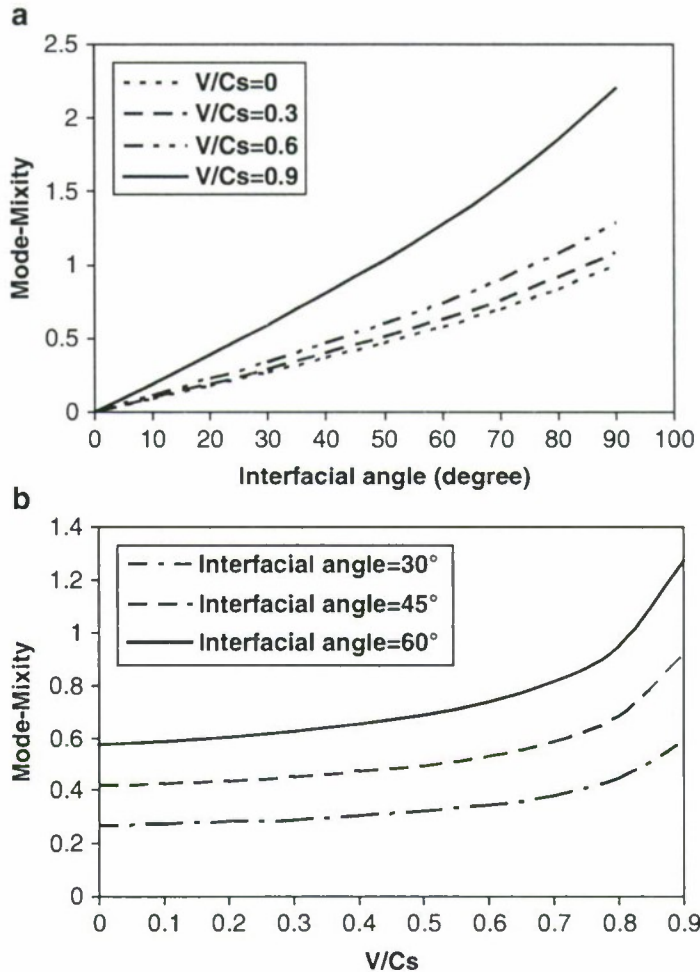


**Fig. 22** Dynamic fracture mode mixity as functions of (a) interfacial angle and (b) crack tip speed

the crack tip speed of the interfacial crack remained constant, mode mixity increased with the increase of the kinking angle. In other words, the larger of the interfacial angle, the larger is the mode II component for the mixed mode crack. This result is similar to the common conclusion in static crack kinking analysis [48].

As a special feature of dynamic crack kinking, the mode mixity increases with the increasing kinked crack speed if the interface angle is fixed. In Fig. 22a, for a fixed kinking or interfacial angle  $50^\circ$ , the mode mixity for a high crack tip speed (90% of the shear wave speed of the matrix material) is almost doubled compared to the mode mixity for a static kinked crack. Here, we should notice that the crack tip speed of the kinked crack is related to the interfacial bonding strength [30]. A weak interface will lead to a fast interfacial crack tip and a high mode-II component as a result. Figure 22b shows the mode mixity dependence on the crack tip speed for different kinking angles. It is interesting to see that each curve has a similar shape and is shifted by some amount for a different kinking angle. In this investigation, the kinking or interfacial angle is limited to  $0-90^\circ$ . Recently, Rousseau and

Rosakis [54] examined important crack kinking behavior for very large interfacial angle (greater than 90°). One important difference is that their incident crack was an inter-sonic shear crack along a weak path rather than a slow mode-I crack as in our investigation. In order to suppress possible crack branching, our incident crack speed was controlled to be less than the crack branching speed (around 30–40% of the shear wave speed for Homalite-100 [55]).

### 3.8 Two-layer Specimens with Direct Impact on the Brittle Polymeric Layer (Fig. 23)

The above discussions are focused on the three-layer specimen or the model sandwich structure. In order to understand the dynamic response and failure of general layered materials or structures, experimental investigation on the two-layer specimen is necessary [56].

In some applications of layered materials, direct impact on the brittle layer such as ceramics layer in composite armor is also very important since their failure behavior might be very different [57]. As shown in Fig. 23 a complicated stress wave propagation, projectile penetration and large deformation process was observed for a two-layer system with a weak and ductile 5083 bond. As soon as the projectile impacted the transparent Homalite layer, a series of fringe patterns related to stress waves developed around the impact site. The projectile head kept moving and complicated stress wave interaction and propagation were observed around 10  $\mu\text{s}$  after impact (Fig. 23b, c).

It should be noticed that the movement of the projectile was not obvious. In the next stage of projectile penetration, a black contact zone was observed at the impact site and an intra-layer crack initiated and propagated towards the interface. In Fig. 23e, it seemed that this intra-layer crack arrested at the interface since no significant interfacial crack propagation (moving fringe concentration) was observed in the following images. As discussed by Xu and Rosakis [33], the crack arrest mechanism by a ductile and weak adhesive layer is due to the dramatically stress wave gradient change across the adhesive layer. After 300  $\mu\text{s}$  of impact (Fig. 23f), a large contact zone appeared in a growing black zone connected to the projectile. Due to large deformation inside the contact zone, those transmitted laser rays were deflected and cannot enter the camera so only a black zone was recorded. Meanwhile, some materials were flying out from the Homalite layer because of the fragments of brittle Homalite subjected to high contact force. Compared to the impact on the strong steel layer of previous cases, direct impact on the brittle Homalite layer has more severe damage in the local impact site.

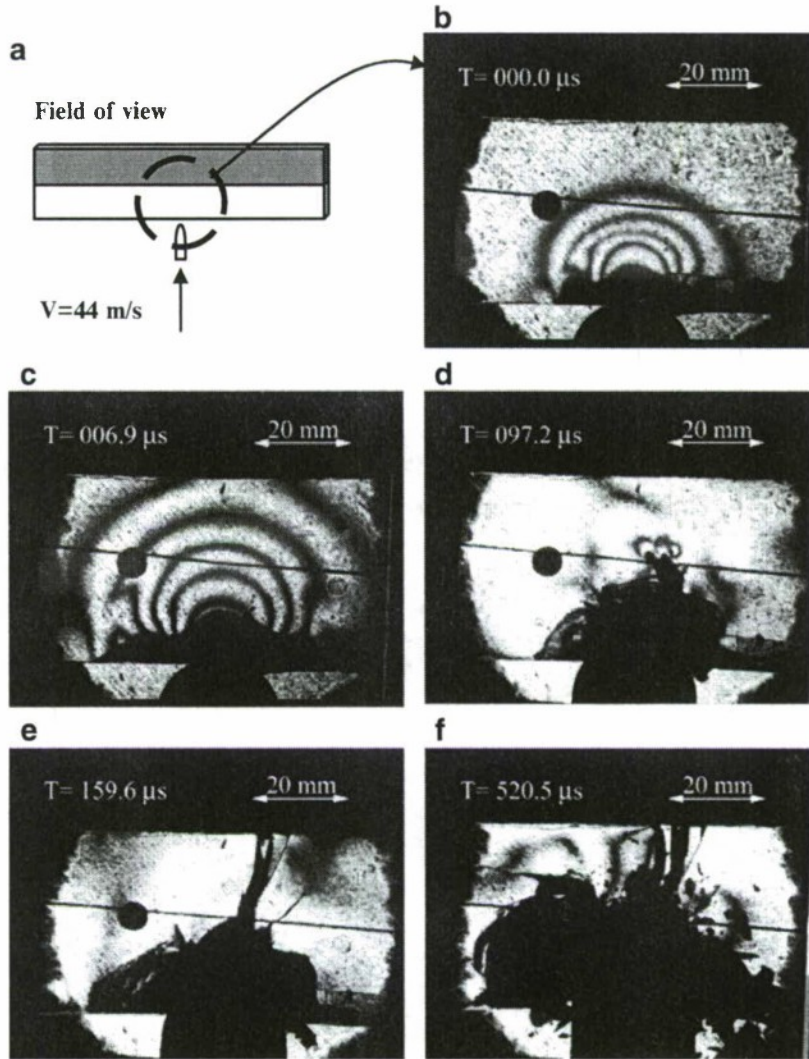


**Fig. 23** Failure sequence of a two-layer specimen (a) impacted directly on the brittle Homalite layer (b–c) show a complicated stress wave process, (d–f) reveal intra-layer crack initiation and propagation and a penetration procedure with large local deformation

#### 4 Conclusions

Inter-layer crack growth (delamination) is the dominant dynamic failure mode for layered materials and sandwich structures subjected to out-of-plane impact. These cracks appear to be shear-dominated and proceed with interersonic speeds. Intra-layer cracking always occurs soon after some amount of inter-layer delamination has already happened and proceeds through the spreading and branching of local mode I cracks into the core layer. Intra-layer or core/matrix cracking often initiates at the interface as a result of inter-layer crack kinking into the core. If the speed of the kinked intra-layer crack reaches a critical value, multiple crack branching may also occur inside the brittle core layer. If free-edge effects at the bimaterial corners

are eliminated (long model sandwich specimens), the failure sequence is slightly modified. Specifically, the inter-layer cracks initiate from positions where the inter-layer shear stress reaches a local maximum equal to the shear strength of the bond. These cracks create a local shear-driven delamination directly above the point of impact. Intra-layer cracks following this process also kink from these positions into the sandwich core.

For some individual dynamic failure modes, we find that the dynamic crack branching can exceed the limit angles  $45^\circ$  (theoretical result) for a second dynamic crack, and the crack tip speeds before and after the crack branching are almost same. Crack kink and penetration at interfaces are mainly governed by the ratio competition of the dynamic energy release rates of the incident crack and the kinked crack, and the dynamic fracture toughness ratio of the matrix (bulk material) and the interface. For the kinked crack speed, it increases if the interfacial angle and interfacial strength decrease. A strength-based criterion is proposed to predict the interfacial debonding ahead of a main crack well.

**Acknowledgements** The authors gratefully acknowledge the support of the Office of Naval Research through a MURI grant to Caltech (N00014-06-1-0730), a research grant to Vanderbilt (N00014-08-1-0137), Dr. Y.D.S Rajapakse, Program Manager of both projects.

## References

1. Hutchinson JW, Suo Z (1992) Mixed mode cracking in layered materials. *Adv Appl Mech* 29: 63–191.
2. Rajapakse YDS (1995) Recent advances in composite research for marine structures. In: Allen, HG (ed) *Sandwich Construction 3*, Proceedings of the Second International Conference. Chameleon, London, Vol. II, pp 475–486.
3. Sun CT, Rechak S (1988) Effect of adhesive layers on impact damage in composite laminates. In: Whitcomb JD (ed) *Composite materials: testing and design (eighth conference)*. ASTM STP 972, American Society for Testing and Materials, Philadelphia, pp 97–123.
4. Cantwell WJ, Morton J (1991) The impact resistance of composite materials – a review. *Comps* 22: 347–362.
5. Abate S (1994) Impact on laminated composites: recent advances. *Appl Mech Rev* 47: 517–544.
6. Gioia G, Ortiz M (1997) Delamination of compressed thin films. *Adv Appl Mech* 33: 119–192.
7. Kadomateas GA (1999) Post-buckling and growth behavior of face-sheet delaminations in sandwich composites. In: Rajapakse YDS, Kadomateas GA (eds) *Thick Composites for Load Bearing Structures*. AMD 235: 51–60.
8. Choi HY, Wu HT, Chang FK (1991) A new approach toward understanding damage mechanisms and mechanics of laminated composites due to low-velocity impact: part II – analysis. *J Comp Mat* 25: 1012–1038.
9. Lambros J, Rosakis AJ (1997) An experimental study of the dynamic delamination of thick fiber reinforced polymeric matrix composite laminates. *Exp Mech* 37: 360–366.
10. Lee JW, Daniel IM (1990) Progressive transverse cracking of crossply composite laminates. *J. Comp Mat* 24: 1225–1243.
11. Oguni K, Tan CY, Ravichandran G (2000) Failure mode transition in unidirectional E-Glass/Vinylester composites under multiaxial compression. *J Comp Mat* 34: 2081–2097.
12. Ju JW (1991) A micromechanical damage model for uniaxially reinforced composites weakened by interfacial arc microcracks. *J Appl Mech* 58: 923–930.

13. Semenki D, Rosakis AJ (1999) Dynamic crack initiation and growth in light-core sandwich composite materials. Proceedings of the 17th Danubia-Adria Symposium on Experimental Mechanics in Solid Mechanics, Prague, pp 297–300.
14. Xu LR, Rosakis AJ (2002) Impact failure characteristics of sandwich structures; Part I: Basic Failure Mode Selections. *Int J Sol Struct* 39:4215–4235.
15. Walter ME, Ravichandran G (1997) Experimental simulation of matrix cracking and debonding in a model brittle matrix composite. *Exp Mech* 37: 130–135.
16. Xu LR, Rosakis AJ (2002) Impact failure characteristics of sandwich structures; Part II: effects of impact speeds and interfacial bonding strengths. *Int J Sol Struct* 39: 4237–4248.
17. Xu LR, Sengupta H, Kuai (2004) An experimental and numerical investigation on adhesive bonding strengths of polymer materials. *Int J Adh Adhes* 24: 455–460.
18. Parameswaran V, Shukla A (1998) Dynamic fracture of a functionally gradient material have discrete property variation. *J Mat Sci* 33: 3303–3311.
19. Rosakis AJ, Samudrala O, Singh RP, Shukla A (1998) Intersonic crack propagation in bimaterial systems. *J Mech Phys Solids* 46: 1789–1813.
20. Dally JW (1979) Dynamic photoelastic studies of fracture. *Exp Mech* 19: 349–61.
21. Singh RP, Shukla A (1996) Subsonic and intersonic crack growth along a bimaterial surface. *J App Mech* 63: 919–924.
22. Williams ML (1957) Stress singularities resulting from various boundary conditions in angular corners in extension. *J Appl Mech* 19: 526–528.
23. Xu LR, Kuai H, Sengupta S (2004) Dissimilar material joints with and without free-edge stress singularities; Part I: a biologically inspired design. *Exp Mech* 44: 608–615.
24. Ravi-Chandar K, Knauss WG (1984) An experimental investigation into dynamic fracture: III. On steady-state crack propagation and crack branching. *Int J Fract* 26: 141–154.
25. Yu C, Ortiz M, Rosakis, A (2003) 3D modelling of impact failure in sandwich structures. *Fracture of Polymers, composites and adhesives, II* Elsevier and ESIS, pp 527–537.
26. Geubelle PH, Baylor JS (1998) Impact-induced delamination of composites: a 2D simulation. *Composites B29B*: 589–602.
27. Wang P, LR Xu (2006) Dynamic Interfacial Debonding Initiation Induced by an Incident Crack. *Int J Solids Struct* 43: 6535–6550.
28. Martinez D, Gupta V (1994) Energy criterion for crack deflection at an interface between two orthotropic media. *J Mech Phys Solids* 42(8): 1247–1271.
29. He MY, Hsueh CH, Becher PF (2000) Deflection versus penetration of a wedge-loaded crack: effect of branch-crack length and penetrated-layer width. *Comps Part B: Engng* 31: 299–308.
30. Xu LR, Huang YY, Rosakis AJ (2003) Dynamic crack deflection and penetration at interfaces in homogeneous materials: experimental studies and model predictions. *J Mech Phys Solids* 51: 461–486
31. Cook J, Gordon JE (1964) A mechanism for the control of crack propagation in all brittle systems. *Proc Royal Soc London* 282A: 508–520.
32. Martin E, Leguillon D, Lacroix C (2001) A revisited criterion for crack deflection at an interface in a brittle material. *Comp Sci Techn* 61: 1671–1679.
33. Xu LR, Rosakis AJ (2003) An experimental study of impact-induced failure events in homogeneous layered materials using dynamic photoelasticity and high-speed photography. *Optics Lasers Engng* 40: 263–288.
34. Evans AG, Zok FW (1994) Review the physics and mechanics of fiber-reinforced brittle matrix composites. *J Mat Sci* 29: 3857–3896.
35. Ahn BK, Curtin WA, Parthasarathy TA, Dutton RE (1998) Criterion for crack deflection/penetration for fiber-reinforced ceramic matrix composites. *Comp Sci Techn* 58: 1775–1784.
36. Siegmund T, Fleck NA, Needleman A (1997) Dynamic crack growth across an interface. I *J Fract* 85: 381–402.
37. Arata JJM, Needleman A, Kumar KS, Curtin WA (2000) Microcrack nucleation and growth in lamellar solids. *Int J Fract* 105: 321–342.
38. Xuan W, Curtin WA, Needleman A (2003) Stochastic microcrack nucleation in lamellar solids. *Engng Fract Mech* 70: 1869–1884.

39. Ramulu M, Kobayashi AS (1985) Mechanics of crack curving and branching – a dynamic fracture analysis. *Int J Fract* 27:187–201.
40. Freund LB (1990) Dynamic fracture mechanics. Cambridge University Press, New York.
41. Yoffe E H (1951) The moving Griffith crack. *Phil Mag, Series 7*, 42, 739.
42. Gao H (1993) Surface roughness and branching instabilities in dynamic fracture. *J Mech Phys Solid* 41 (23): 457–486.
43. Seelig Th, Gross D (1999) On the interaction and branching of fast running cracks – a numerical investigation. *J Mech Phys Solids* 47: 945–952.
44. Sharon E, Fineberg J (1999) Confirming the continuum theory of dynamic brittle fracture for fast cracks. *Nature* 397: 333–335.
45. Xu LR, Rosakis AJ (2003b) Real-time experimental investigation of dynamic crack branching using high-speed optical diagnostics. *Exp Techn* 27: 23–26.
46. Shukla A, Nigam H, Zervas H (1990) Effect of stress field parameters on dynamic crack branching. *Engng Fract Mech* 36: 429–438.
47. Xu LR, Wang P (2006) Dynamic fracture mechanics analysis of failure Mode transitions along weaken interfaces in elastic solids. *Engng Fract Mech* 73: 1597–1614.
48. Anderson TL (1995) Fracture Mechanics, 2nd edn. CRC, Boca Raton.
49. Li XF, Xu LR (2007) T-stresses across static crack kinking. *ASME J Appl Mech* 74: 181–190.
50. Cotterell B, Rice JR (1980) Slightly curved or kinked cracks. *Int J Fract* 16(2): 155–169.
51. Azhdari A, Nemat-Nasser S (1996) Energy-release rate and crack kinking in anisotropic brittle solids. *J Mech Phys Solids* 44: 929–951.
52. Gupta V, Argon AS, Suo Z (1992) Crack deflection at an interface between two orthotropic materials. *J Appl Mech* 59: 79–87.
53. Ravi-chandar K, Lu J, Yang B, Zhu Z (2000) Failure mode transitions in polymers under high strain rate loading. *Int J Fract* 101: 33–72.
54. Rousseau C-E, Rosakis AJ (2003) On the influence of fault bends on the growth of Sub-Rayleigh and intersonic dynamic shear ruptures. *J Geophys Res* 108: 2411–2431.
55. Broberg KB (1999) Cracks and fracture. Academic, San Diego.
56. Xu LR, Rosakis AJ (2005) Impact damage visualization of heterogeneous two-layer materials subjected to low-speed impact. *Int J Dam Mech* 14: 215–233.
57. Cheeseman B, Jensen R, Hoppe C (2004) Protecting the future force: advanced materials and analysis enable robust composite armor. *AMPTIAC* 8(4): 37–43.

# In-class Paper Demonstrations and Experiments for Solid Mechanics Courses\*

L. ROY XU\*

*Department of Civil and Environmental Engineering, VU Station B 351831, Vanderbilt University, Nashville, TN 37235, USA. E-mail: l.roy.xu@vanderbilt.edu*

*Attending in-class paper demonstrations and performing experiments in solid mechanics courses are very effective ways for students to gain an understanding of the complicated concepts of mechanics. This paper explores a few applications of dagbane tensile tests, stress concentrations and crack kinking or mixed-mode fracture. Furthermore, this handy technique can be extended to other broader areas of mechanics education. Since only simple materials and supplies are used: copy paper, staples, scissors and a paper punching machine, students can repeat these typical mechanics experiments in future in other locations, such as in an office or at home. Therefore, this simple and effective technique can have a remarkable influence on the student's long-term career.*

**Keywords:** mechanics education; mechanics of materials; solid mechanics; experimental mechanics

## INTRODUCTION

THE AUTHOR'S first-year teaching assignments at Vanderbilt University included two graduate courses: Advanced Mechanics of Solids, Parts I and II. Part I mainly covers the theory of elasticity, while Part II ranges from plasticity, buckling, and stress waves to fracture mechanics. These highly theoretical courses require a strong mathematical background and the author found that many graduate students felt overwhelmed by the derivation of equations. Therefore, the author decided to add some experimental demonstrations to enable the students to understand complex mechanics phenomena. Before teaching the Rayleigh surface wave, the author showed a vivid movie on stress wave propagation (which can now be seen on the author's Website) based on the author's previous impact mechanics research using high-speed photography [1]. The movie captured the students' interest, hence they concentrated on the long derivation involving the speed relationship between the Rayleigh wave and the shear wave. It was then that the author recalled a famous maxim, "I hear and I forget; I see and I remember; I do and I understand," (Chinese philosopher and educator Lao Tsu, 604–531 BC). Therefore, he decided to develop a few in-class demonstrations, both for the two graduate courses mentioned above, and for two other undergraduate courses: Mechanics of Materials and Statics.

## CURRENT CHALLENGE OF SOLID MECHANICS COURSES

Since traditional solid mechanics courses involve the successful applications of applied mathematics

[2–3], they are challenging for the engineering students who have less mathematical training. For example, students who have never taken a Partial Differential Equation course would find that it is difficult to understand Boundary Value Problems (BVP, a pure mathematical terminology) in the theory of elasticity [4–5]. Therefore, for modern mechanics educators, the use of too much mathematical derivation without the provision of engaging examples may turn the students' interests to other fields that they perceive to be more fun; this does not help the development of mechanics disciplines. Fortunately, new information technology provides us with excellent tools for dynamic instruction and effective visualization.

The main objective of this paper is to demonstrate that a solid mechanics course is a series of dynamic and fun events, rather than a cluster of boring equations. Indeed, in his series of classical mechanics textbooks, outstanding mechanics researcher and educator, Professor S. Timoshenko, often used experimental stress techniques such as photoelasticity to explain complicated solid mechanics problems [4]. Now, modern multimedia could be used to realize this goal more effectively. Usually, we want to expose students to three areas of mechanics—experimentation, theory and computation [6]. The use of multimedia, such as personal computers and the Internet, can be very helpful in explaining theoretical and computational aspects of mechanics, and can even be used to conduct "virtual experiments" [7]. However, for undergraduate introductory level classes such as the mechanics of materials, the impact of multimedia on teaching fundamental concepts has been less successful [8]. Therefore, effective and original experimental education such as doing tensile tests in mechanics of material courses still cannot be replaced [9–11].

\* Accepted 9th January 2007

## IN-CLASS PAPER DEMONSTRATIONS AND EXPERIMENTS

For experimental demonstrations, not every educator has sufficient laboratory facilities or experience to conduct educational experiments such as the classical photoelasticity technique [9]. In order to develop a handy education technique, the author has explored an in-class paper (A4 copy paper, etc.) experiment, which can be employed not only in classroom teaching, but also for outreach presentations. Since the mechanics of paper is a typical plane stress problem, the author has extensively used A4 copy paper in classroom lectures for mechanics of materials (dogbone tensile tests), theory of elasticity (stress concentration around a central hole), plates and shells (Kirchhoff's assumptions) and fracture mechanics (crack kinking and fracture modes). For example, a classical mixed-mode fracture experiment [12] can easily be conducted and takes only a few minutes. For a laboratory experiment to demonstrate the same mixed-mode fracture phenomenon, the process may take at least several days, from specimen preparation to the final experiment. Moreover, the cost would be much higher than that of our paper experiment. In the following sections, we will describe in detail the steps of a few typical in-class experiments from specimen preparations to final experiments, and give the related theoretical background.

### *Applications in basic mechanics courses—dogbone tensile tests and stress concentrations*

Traditional mechanics of materials courses mainly cover the mechanical response of a metal bar subjected to tension and other loadings. Therefore, the corresponding laboratory class is focused on the stress and strain measurements of a steel or aluminum cylinder specimen. With the extensive

applications of new polymers and composite materials, as well as thin films [13], dogbone specimens have become quite popular for use in tensile experiments. Figure 1 shows the preparation process of a paper dogbone specimen. The first step is to print out symmetrical axes and specimen edges using computer software such as Microsoft Word. The second step is to fold the whole paper into a quarter so that only "Part 1" can be seen. Then, using scissors, the curved edges are carefully cut. Now a dogbone specimen is ready to be tested as seen in Fig. 1(c). For comparison, a rectangular paper specimen (a strip) is also cut. Students can pull the ends of these two kinds of tensile specimens and compare their failure patterns. The final fracture of the dogbone specimen is often at the specimen center (a valid tensile test). However, the location of the final fracture of the rectangular paper specimen is random, i.e., at the specimen center or the grip location, etc.

The dogbone specimen can be used to demonstrate another important solid mechanics phenomenon: stress concentration. As shown in Fig. 2(a), a paper punch is used to punch a hole in the dogbone specimen. According to classical elasticity solutions, for an infinite plate with a circular hole of radius,  $a$ , subjected to remote uniaxial tension,  $\sigma$ , the stress components along the hole edge expressed in a polar coordinate system are [4]

$$\begin{aligned}\sigma_{rr} &= \frac{\sigma}{2} \left( 1 - \frac{a^2}{r^2} \right) + \frac{\sigma}{2} \left( 1 + \frac{3a^4}{r^4} - \frac{4a^2}{r^2} \right) \cos(2\theta) \\ \sigma_{\theta\theta} &= \frac{\sigma}{2} \left( 1 + \frac{a^2}{r^2} \right) - \frac{\sigma}{2} \left( 1 + \frac{3a^4}{r^4} \right) \cos(2\theta) \\ \sigma_{r\theta} &= -\frac{\sigma}{2} \left( 1 - \frac{3a^4}{r^4} + \frac{2a^2}{r^2} \right) \sin(2\theta).\end{aligned}\quad (1)$$

For  $\theta = \pi/2, 3\pi/2$ ,  $\sigma_{\theta\theta}$  attains its maximum value  $3\sigma$ . Here, "3" is called the stress concentration

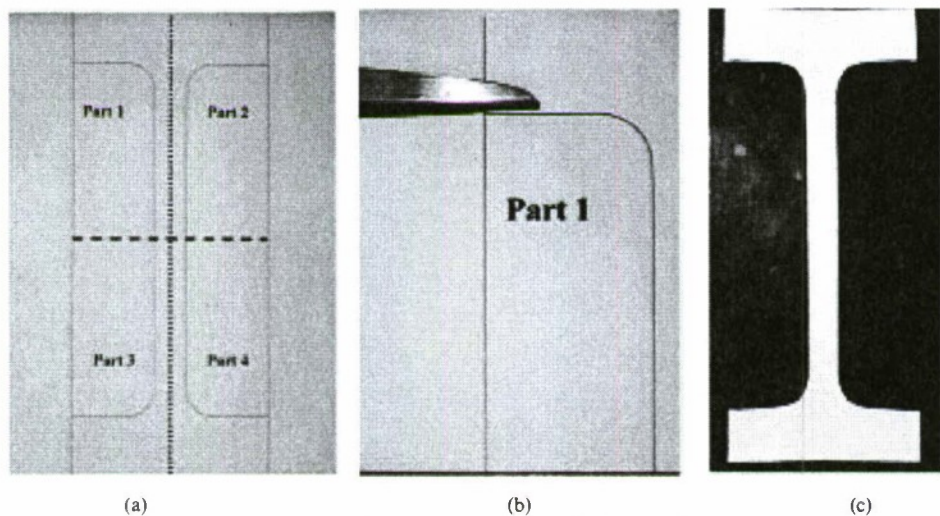


Fig. 1. Dogbone tension specimen preparation using A4 copy paper: (a) mark fold lines on A4 paper using computer software such as Microsoft Word; (b) fold the whole paper into one quarter and cut paper using scissors; (c) a complete dogbone specimen.

factor. For a finite dogbone specimen with a central hole, the stress concentration factor is less than 3. By conducting tensile tests of the dogbone specimens with and without central holes, students will be able to notice that the dogbone specimen with a central hole often fails at the hole edge due to the high stress concentration. Because these elasticity equations are usually beyond the undergraduate student curriculum, the use of the stress flow concept is more effective to explain the stress concentration phenomenon. As with fluid visualization, the tensile stress of the dogbone specimen at the far field is quite uniform as shown in Fig. 2(b). However, the stress flow becomes "very crowded" when it encounters the central hole, since the stress flow cannot pass across the hole. Therefore, a stress concentration occurs at the location with a significant flow concentration as seen in Figure 2(b). This is a clear explanation of the stress concentration for undergraduate students (even for graduate students). The stress flow concept could be more effective if students have taken the fluid mechanics course, and know how to apply the continuity or mass equation.

#### *Applications in advanced mechanics courses—fracture and fiber-reinforced composites*

For advanced solid mechanics courses, fracture mechanics is one of the most important subjects. After the theory of elasticity and plasticity, the major challenge for graduate students is to understand the concepts of the singular stress field at a crack tip (theoretical stress values are infinity, based on the elasticity solutions), and the stress intensity factor of a crack in Linear Elastic Fracture Mechanics. In experimental mechanics, the singular stress field will result in a high stress concentration at the crack tip or bi-material corner [14]. Of course, a fracture experiment using photoelasticity or other techniques may

lead to a much clearer understanding of fracture mechanics. However, many instructors do not have sufficient time and laboratory facilities to prepare these demonstrations. The author has developed a convenient paper experiment to demonstrate the concepts of the stress intensity factor and mixed-mode fracture, which are among the most important topics in fracture mechanics courses. As shown in Fig. 3, first we fold a piece of A4 copy paper and cut an initial 'crack', then we load the initial 'crack' by pulling on the paper. When the pulling load is sufficiently large, sudden crack kinking occurs, due to the mixed-mode load, as shown in Fig. 3(c). This experiment is easy to conduct and one can change the fold angle of the initial crack, and obtain different crack kinking patterns. Indeed, the crack kinking phenomenon involves an interesting theoretical background.

A crack will propagate away from its original path due to any change in local fracture mode mixity (a mechanics factor) or fracture toughness (a material factor). This phenomenon is often called "crack kinking or deflection" [15–18]. For a two-dimensional elastic solid, the full-field stress tensor of a mixed-mode main crack as seen in Fig. 3(b), can be expressed in a polar coordinate system as in Williams [19] and Anderson [20].

$$\sigma_{ij}^m(r, \theta) = \frac{K_I^m}{\sqrt{2\pi r}} \sum_{ij}^I(\theta) + T\delta_{i1}\delta_{j1} + \frac{K_{II}^m}{\sqrt{2\pi r}} \sum_{ij}^{II}(\theta) + O(r^{\frac{1}{2}}) \quad (i, j = 1, 2)$$

where  $m$  and  $k$  denotes "main crack" and "kinked crack" respectively.  $K_I$  and  $K_{II}$  are mode I and mode II stress intensity factors;  $T$  is a nonsingular term;  $O(r^{\frac{1}{2}})$  represents higher order terms of the length scale  $r$  and will be dropped if the kinked crack length  $l$  is very small; and known functions  $\Sigma_{ij}^I(\theta), \Sigma_{ij}^{II}(\theta)$  represent the angular variations of

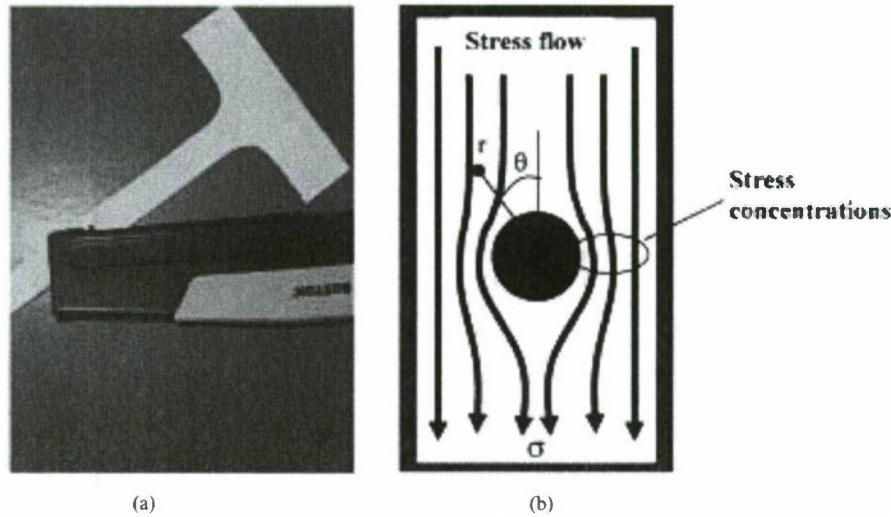


Fig. 2. Stress concentrations during tension experiments: (a) punch a hole in a dogbone specimen using a paper punching machine; (b) stress flow around the circular hole.

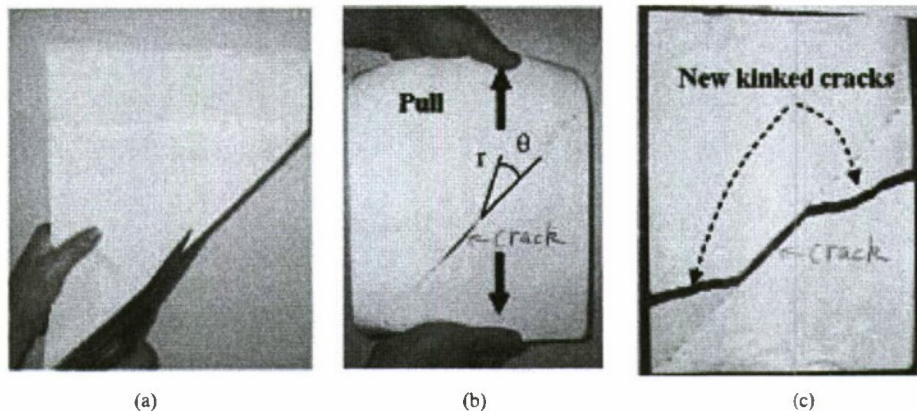


Fig. 3. Paper experiment to demonstrate the crack kinking phenomenon: (a) folding paper and cut an initial 'crack'; (b) loading the initial 'crack' by pulling paper; (c) crack kinking due to mixed-mode loading.

stress components. Previous research on crack kinking reveals that there is a relation between the stress intensity factors before and after crack kinking, which can be expressed in a combined way as [16, 21]:

$$K_I^k = c_{11}K_I^m + c_{12}K_H^m + b_1 T \sqrt{I} \quad (3)$$

$$K_H^k = c_{21}K_I^m + c_{22}K_H^m + b_2 T \sqrt{I}. \quad (4)$$

Numerous results have been reported to determine the coefficients  $c_{ij}$  and  $b_i$  ( $i,j = 1,2$ ). From the above relations it is obvious that the stress intensity factors of the kinked crack depend on the stress intensity factors of the initial main crack. Furthermore, we can use stress or energy criteria to predict the crack kinking initiation load and its angle of kink [12, 22]. Therefore, by using different kinds of paper materials and differently inclined angles of

the main cracks, a course project on mixed-mode fracture allows students to obtain a deep understanding of the concepts of fracture mechanics. In addition to demonstrating the mixed-mode fracture phenomenon, paper with an edge crack as shown in Fig. 4(a) can be used to demonstrate mode I-opening, mode-II in-plane shear and mode-III out-of-plane shear, by holding the two edges and applying different kinds of load (in-plane tension; tearing, etc).

The edge-cracked paper could be slightly modified to demonstrate the mechanics of fiber-reinforced composites. As seen in Fig. 4(a), several staples fixed in front of a main crack are used to increase the local fracture resistance of the paper material. These stiff and strong staples are analogous to short micro/nano fibers used in composites [23–24]. In Fig. 4(b), after we pull the paper with an edge crack, the main crack kinks along the ends of the short staples, since the local fracture toughness

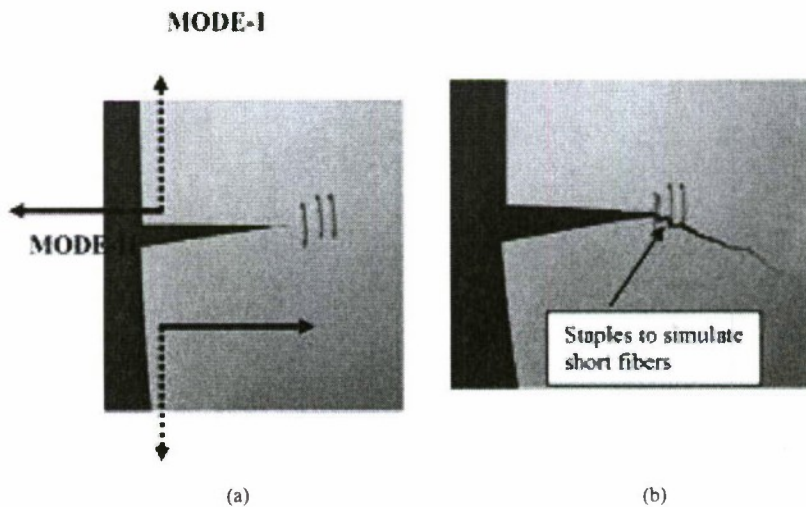


Fig. 4. Demonstration of fracture modes and fiber-reinforced composites using paper and staples: (a) mode-I opening and mode-II in-plane shear modes; (b) short fibers can provide high fracture resistance.

of the paper is significantly increased by these strong staples. This experiment demonstrates a fracture mechanics conclusion: a crack tends to choose a path of low fracture resistance (toughness).

These paper experiments and demonstrations used in the classroom may have a long-term influence on the student's future career. Since we need only simple materials and supplies: copy paper, staples, scissors and paper punching machines, students can repeat these experiments elsewhere in the future, such as in an office or their homes. Therefore, the general public can easily understand the important role of solid mechanics in scientific research.

## CONCLUSIONS

In-class paper experiments for solid mechanics courses are an effective way for students to learn to understand complicated mechanics concepts. This paper explores a few such applications in dogbone tensile tests, stress concentrations and crack kinking or mixed-mode fracture. This handy technique of solid mechanics education can be used to demonstrate the impact of solid mechanics research to the general public.

*Acknowledgement*—The author gratefully acknowledges the support from the National Science Foundation and the Office of Naval Research.

## REFERENCES

1. <http://people.vanderbilt.edu/~l.roy.xu/mv.html>
2. Y. C. Fung, *Foundations of Solid Mechanics*, Prentice-Hall, Englewood Cliffs, NJ, (1965).
3. L. B. Freund, *Transitions of Engineering Education and Research: An Interim Report from the Field*, p. 203–223. RIT, Stockholm, (1998).
4. S. P. Timoshenko and J. N. Goodier. *Theory of Elasticity*, 3rd edn, McGraw-Hill, (1970).
5. N. I. Muskhelishvili, Some basic problems of the mathematical theory of elasticity, Noordhoff International Publishing Company, Leyden, The Netherlands, (1975).
6. C. J. Lissenden and N. J. Salamon, Design project for advanced mechanics of materials, *Int. J. Eng. Educ.*, **20**, 2004, pp. 103–112.
7. S. M. Holzer and R. H. Andruet, Experimental learning in mechanics with multimedia, *Int. J. Eng. Educ.*, **16**, 2000, pp. 372–384.
8. T. A. Philpot, MDSolids: Software to bridge the gap between lectures and homework in mechanics of materials, *Int. J. Eng. Educ.*, **16**, 2000, pp. 401–407.
9. A. S. Kobayashi (ed.) *Handbook on Experimental Mechanics*, Society of Experimental Mechanics, Prentice-Hall, New Jersey, (1987).
10. J. W. Dally, Dynamic photoelastic studies of fracture, *Experimental Mechanics*, **19**, 1979, pp. 349–61.
11. T. Belendez, C. Neipp and A. Belendez, Numerical and experimental analysis of a cantilever beam: a laboratory project to introduce geometrical nonlinearity in mechanics of materials, *Int. J. Eng. Educ.*, **6**, 2003, pp. 885–892.
12. F. Erdogan and G. Sih, On the crack extension in plates under plane loading and transverse shear, *Journal of Basic Engineering*, **85**, 1963, 519–527.
13. L. B. Freund and S. Suresh, *Thin film Materials: Stress, Defect Formation and Surface Evolution*, Cambridge University Press, Cambridge, UK, (2003).
14. L. R. Xu, H. Kuai, and S. Sengupta, Dissimilar material joints with and without free-edge stress singularities: Part I. a biologically inspired design, *Experimental Mechanics*, **44**, 2004, pp. 608–615.
15. K. B. Broberg, *Cracks and Fracture*. Academic Press, San Diego, (1999).
16. M. Y. He and J. W. Hutchinson, Crack deflection at an interface between dissimilar elastic materials, *International Journal of Solids and Structures*, **25**, 1989, pp. 1053–1067.
17. V. Gupta, A. S. Argon and Z. Suo, Crack deflection at an interface between two orthotropic materials, *J. of Applied Mechanics*, **59**, 1992, pp. s79–s87.
18. L. R. Xu, Y. Y. Huang and A. J. Rosakis, Dynamic crack deflection and penetration at interfaces in homogeneous materials: experimental studies and model predictions, *Journal of Mechanics and Physics of Solids*, **51**, 2003, pp. 425–460.
19. M. L. Williams, On the stress distribution at the base of stationary crack, *Journal of Applied Mechanics*, **24**, 1957, pp. 109–114.
20. T. L. Anderson, *Fracture Mechanics*, 2nd edn, CRC Press, Boca Raton, (1995).
21. B. Cotterell and J. R. Rice, Slightly curved or kinked cracks, *International Journal of Fracture*, **16**, 1980, pp. 155–169.
22. A. Azhdari and S. Nemat-Nasser, Energy-release rate and crack kinking in anisotropic brittle solids, *Journal of the Mechanics and Physics Solids*, **44**, 1996, pp. 929–951.
23. I. M. Daniel, and O. Ishai, *Engineering Mechanics of Composite Materials*, Oxford University Press, New York, (1994).
24. L. R. Xu, V. Bhamidipati, W.-H. Zhong, J. Li, C. M. Lukehart, E. Lara-Curzio, K. C. Liu and M. J. Lance, Mechanical property characterization of a polymeric nanocomposite reinforced by graphitic nanofibers with reactive linkers, *J. of Composite Materials*, **38**, 2004, pp. 1563–1582.

**L. R. Xu** is an Assistant Professor of Civil Engineering and Materials Science at Vanderbilt University. He received his Ph.D. degree in Aeronautics and Materials Science from the California Institute of Technology in 2002. He was an Office of Naval Research Young Investigator (Structural Mechanics) in 2003. As an author of 32 journal papers, his research covers advanced composite materials, impact and interfacial mechanics, experimental mechanics and fracture/failure mechanics.

## Effect of the Interfacial Stress Distribution on the Material Interfacial Shear Strength Measurement

A. Krishnan · L.R. Xu

Received: 2 September 2009 / Accepted: 10 November 2009 / Published online: 26 November 2009  
© Society for Experimental Mechanics 2009

**Abstract** An integrated experimental and numerical analysis is carried out to study the interfacial shear strength of bonded materials. Two types of shear tests, namely the Iosipescu shear test, and the short-beam shear test are employed to understand the effect of interfacial stress on the interfacial shear strength measurements. The measured average shear strengths are very close, even though the interfacial shear stress distributions of these two kinds of specimens are very different. Therefore, we conclude that the interfacial stress distribution has the least effect on the interfacial strength measurement if the interfacial shear stress is non-singular.

**Keywords** Adhesion · Interfacial strength · Photo-elasticity · Finite element simulations · Monte Carlo simulations · Shear failure

### Introduction

Composite materials find extensive applications in many engineering fields [1]. Since composites are made of two or more materials, there exists an interface between the different types of materials. This interface is usually the weakest link and hence it becomes very important to characterize its mechanical properties [2]. For example, the

interfacial strength is an important parameter which determines the interface failure subject to dynamic loading [3–5]. Recent atomistic simulations show that the interfacial shear strength of the copper-niobium interface is always lower than the shear strength of perfect crystals, and is spatially non-uniform [6]. There are several different approaches to measure the interfacial shear strength of composites and bonded materials such as the fiber push-out test for the fiber/matrix interface [7, 8]. Recently, the issues on the free-edge stress singularity and the highly non-uniform stress distribution have been raised for this type of an experiment [9]. An important question arising out of this discussion would be to determine if the interfacial stress distribution has an influence on the interfacial strength measurement. In order to get rid of the bimaterial free-edge stress singularity and address this fundamental issue, here a same material joint with a weakening interface is used intentionally. This type of material joint was proposed to investigate the dynamic fracture [10, 11]. In case of shear specimens, the Iosipescu shear and short-beam shear specimens will be employed as shown in Fig. 1.

The Iosipescu shear test provides a region of uniform shear stress in the test zone compared to a parabolic shear stress variation shown by the short-beam shear specimen. The Iosipescu shear test was developed to measure the strength of composites and has been extensively modified before coming to its present state [12–15]. Concurrently, the short-beam shear test is also used widely to measure the shear strength of composite materials. The Iosipescu specimen shows a near constant variation of interfacial shear stress, which might be seen as a major advantage over other types of shear tests. Therefore, if we use these two

A. Krishnan · L.R. Xu (✉, SEM member)  
Department of Civil and Environmental Engineering  
and Materials Science Program, Vanderbilt University,  
Nashville, TN 37235, USA  
e-mail: luoyu.r.xu@gmail.com

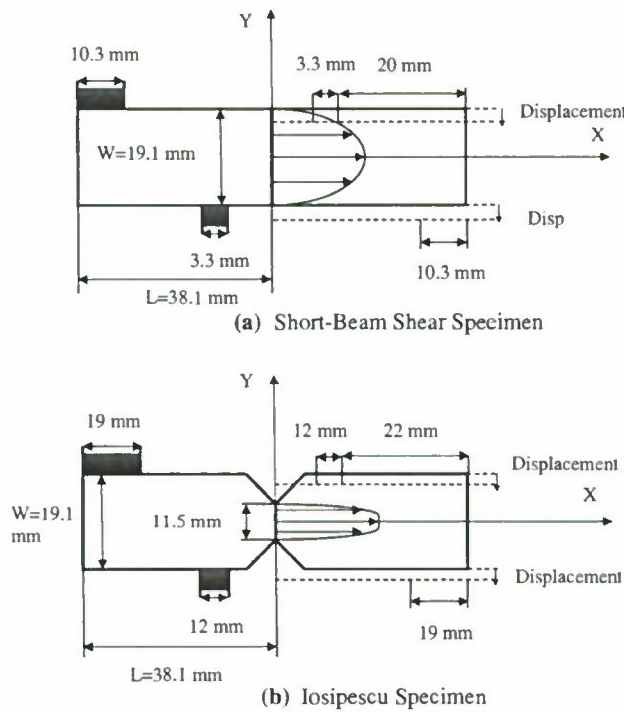


**Fig. 1** Variation of interfacial shear stress for (a) Short-beam shear specimen (Parabolic shear stress variation) and (b) Iosipescu shear specimen (Near constant shear stress variation). A schematic of the boundary conditions used in finite elements (anti-symmetric) is also shown

different approaches to measure the interlaminar shear strength of the same graphite/epoxy material system, should we get very different shear strengths using these two approaches due to very different interfacial shear stress distributions, or almost the same strength because the interfacial shear stress distribution has the least effect on the final shear strength?

Surprisingly no one has explored this important and fundamental issue over the past 40 years (Adams DF, Private Communications, 2003). Therefore, in-depth mechanics and materials work are much needed since there are several other approaches to measure the shear strengths of composite materials [1, 16]. The objective of this study is to analyze the effect of the interfacial stress distribution on the strength measurements. In order to avoid complicated failure modes during shear tests [17], and to only focus on the shear failure of an interface, we design and test bonded polymers and metals such that the bonded interface is the only weak path leading to the final shear failure.

### Experimental Investigation

Test specimens were made of three different types of materials including Aluminum, Polymethyl methacrylate

(PMMA) and Polycarbonate. The specimens were not monolithic and were bonded from individual halves. The adhesive used in this experiment is Loctite 384. One of the key requirements in choosing the adhesive was that its bonding strength should be far lesser than that of the bulk material. The specimens were bonded at room temperature using a special fixture to guarantee their dimensionality. The individual halves were sandblasted at the bonding surfaces in order to provide good adhesion.

The test set-up consists of three parts including a mechanical system to load the specimen, an optical system to develop fringe patterns and an imaging system to record the images [18]. The mechanical testing system included an MTS 810 test machine and an Iosipescu test fixture. The fringe patterns developed only in case of the transparent Polycarbonate specimens, and the isochromatic fringe patterns are the contours of the maximum in-plane shear stress [19]:

$$\tau_{\max} = \frac{(\sigma_1 - \sigma_2)}{2} = \frac{Nf_{\sigma}}{2h} \quad (1)$$

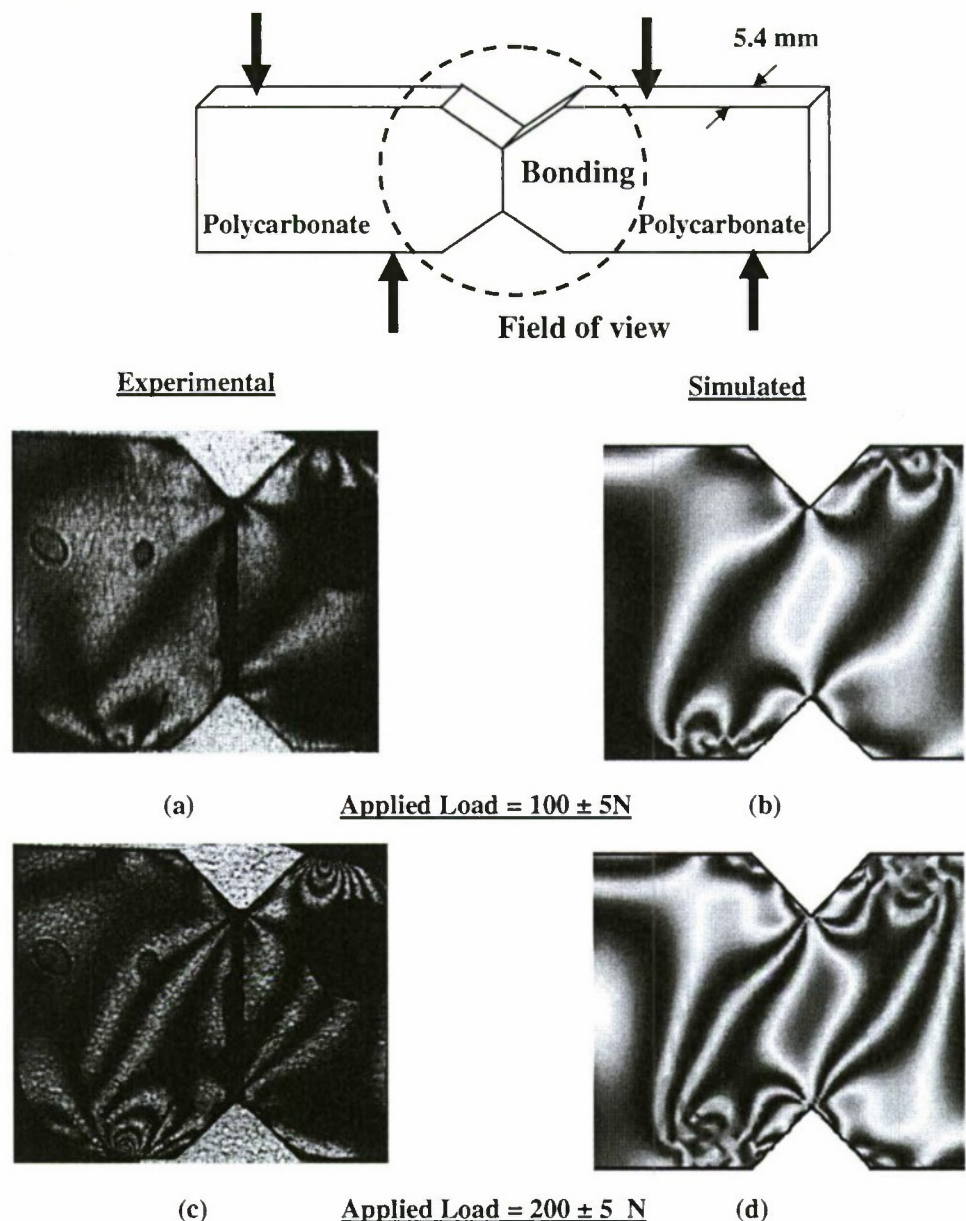
where  $\sigma_1$  and  $\sigma_2$  are the in-plane principal stresses, N is the fringe order,  $f_{\sigma}$  is the stress-fringe constant, and h is the thickness of the specimen. The imaging system included a high-resolution digital camera to capture the fringe development and a density filter in front of the camera to reduce the laser intensity.

Load was applied to the movable half of the Iosipescu test fixture in the form of displacement at a rate of 1 mm/min until failure. About 25–35 specimens of each type (Iosipescu and short-beam shear) were tested in order to ensure repeatability. Almost all of the specimens failed due to shear at the interface which was necessary in this case as we measure the shear strengths. Pictures of the fringe patterns at load levels of 12.5 % (100 N) and 25 % (200 N) of failure load were taken for Polycarbonate as seen in Figs. 2 and 3, and videos depicting the development of fringes from the beginning of loading till failure were recorded.

### Finite Element Modeling

A finite element model of the specimen was built using the software ANSYS 11.0 to obtain the stress distribution of the bonded specimen. A two dimensional analysis was considered for bonded Polycarbonate materials (Elastic Modulus of 2.4 GPa, and a Poisson's Ratio of 0.35). A linear elastic and isotropic material model was used in this analysis. The dimensions of the specimen were: width of 76.2 mm (individual parts have a width of 38.1 mm) and a

**Fig. 2** Comparison between experimental and finite element generated fringe patterns for Iosipescu specimen made of Polycarbonate

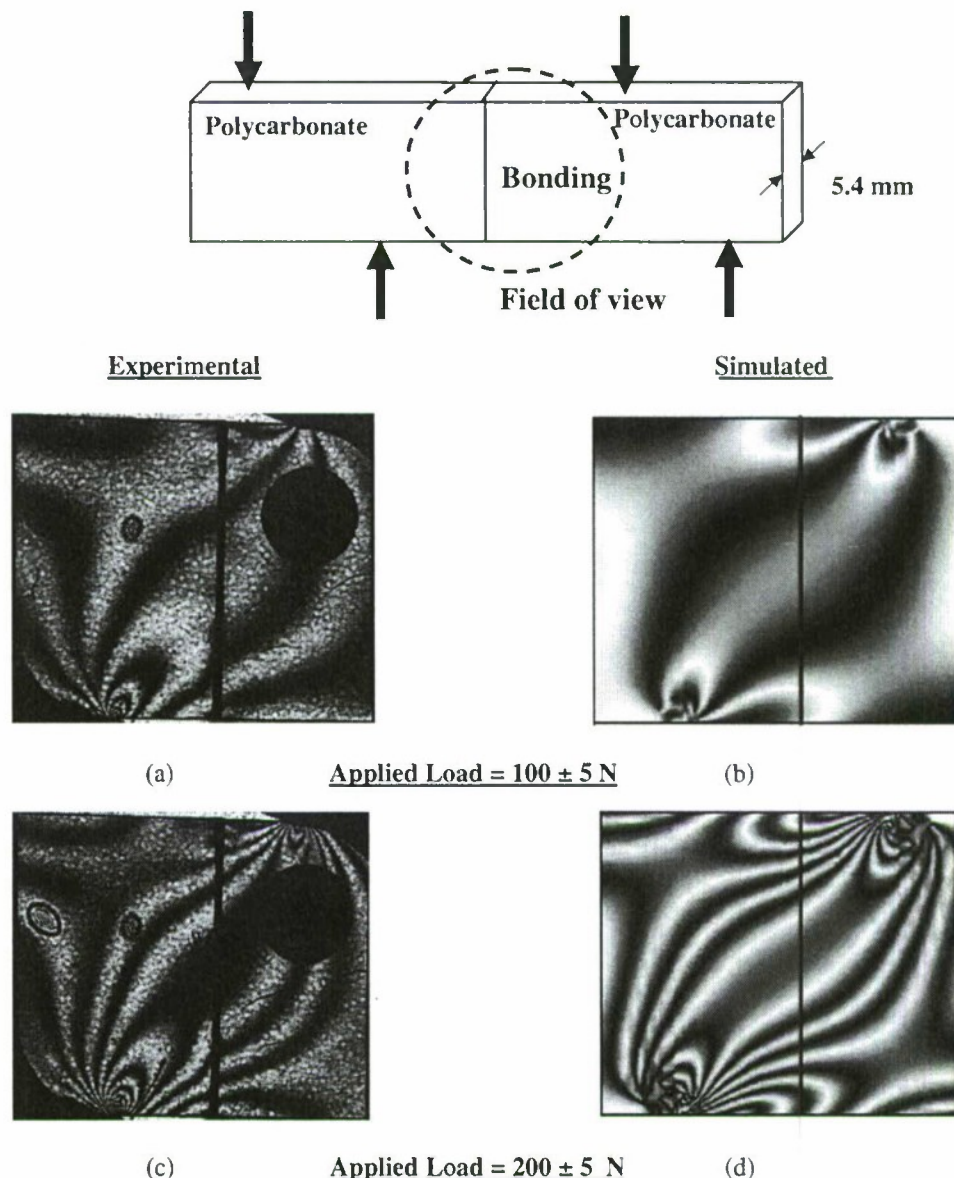


height of 19.1 mm. Plane 42 elements were exclusively used in order to meet the requirements of the plotting software Tecplot. The procedure for simulating the boundary conditions was adopted similar to the method reported in [17].

In order to incorporate a realistic simulation of the load transfer from the fixture to the specimen, an iterative procedure was adopted. Displacement constraints are applied, similar to what is observed in reality. The left portion of the specimen is fixed and cannot move in the vertical dimension. The top left edge node is restrained from moving in both x and y directions in order to prevent rigid body movements. On

the right portion, an initial vertical uniform displacement is applied. Now the reaction loads at each of the nodes with a constraint is checked to verify that they are not in tension (in real experiments, only compressive loading is obtained). The constraint was removed from those nodes which showed a tensile reaction force instead of a compressive one, and a new analysis with the updated set of boundary conditions was carried out. This was done until convergence and the total applied load was obtained by integrating the shear stress across the bonded interface of the specimen. This procedure was iteratively carried until the required load (for matching the fringe patterns) was obtained. It should

**Fig. 3** Comparison between experimental and finite element generated fringe patterns for short-beam shear specimen made of Polycarbonate



be noted that the loading is anti-symmetric and remains so after every iteration.

The numerical photoelasticity fringe patterns were obtained by plotting the stress distribution from the finite element analysis using the plotting software Tecplot. The maximum shear stress was obtained from the finite element analysis by using the principal stress values. Using equation (1), this stress value was then converted to a fringe order  $N$  which in turn was converted into a grayscale value. Half order fringes (0.5, 1.5, 2.5, etc.) were given a value of 255 and full order fringes (0, 1, 2, etc.) were assigned a value of 0 on the grayscale spectrum.

## Results and Discussion

A direct comparison between the experimental fringe patterns and the fringe patterns is obtained from the numerical analysis as shown by the results presented in Fig. 2 for the Iosipescu specimen and in Fig. 3 for the short-beam shear specimen. At lower loading levels (around 100 N), the fringes begin to appear from the points of stress concentration (loading point) and begin to spread out towards the ends of the shear specimens. More fringes continue to appear as the loading is increased and the patterns are recorded on a video camera until failure. The finite element analysis captures

all the major features seen in the experimental patterns thereby validating our finite element model and loading simulation.

The interfacial shear strengths of the three kinds of bonded materials are presented in Table 1. It was observed that the average shear strengths of the two types of different shear tests were close. In the case of bonded aluminum specimens it is seen that the difference in means (between Iosipescu and short-beam shear specimens) is much lesser compared to the other two bonded specimens. In general, acrylic materials (PMMA) and metals show a better bonding in comparison with Polycarbonate which consistently gives a lower value of the interfacial shear strength. Since these two types of shear tests lead to very similar results, the short-beam shear test will have advantages like low machining and fixture cost, and shorter time for preparation. In order to provide mechanics insight into the shear failure process at the interface, Monte Carlo simulations using the initial interfacial flaw assumption were carried out [20]. The interfacial shear stress distributions at failure loads of the Iosipescu (with same cross-sectional area as the short-beam shear specimen) and the short-beam shear specimens from the finite element analysis are shown in Fig. 4. It can be seen that the variation in shear stress at the interface is parabolic for the short-beam shear specimen, but almost constant for the Iosipescu specimen. Therefore, we should briefly review the strength conception, and the stress distribution of the specimens to measure the strength.

The tensile strength definition of a homogeneous material is quite straightforward: it is defined as the failure stress of a specimen with a uniform stress distribution across the cross section. Since the final failure of the material is associated with the initial defect distribution (e.g., Weibull strength distribution) at the cross section, specimens with different sizes will yield different strength data. This phenomenon may be defined as ‘the material size effect.’ In this investigation, we employed homogeneous materials but with artificial interfaces to ensure that failure will occur along these weak interfaces, thereby avoiding complicated bi-material problems in obtaining useful fundamental results [21].

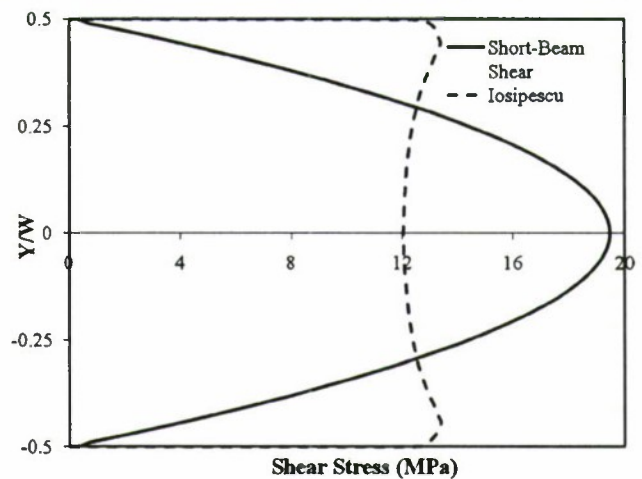


**Fig. 4** Comparison of the interface shear stress distributions at failure load of 728 N between the short-beam shear specimen and the Iosipescu shear specimen from the finite element analysis

However, for bi-materials specimens, the interfacial strength measurement becomes quite complicated due to existence of possible free-edge stress singularity [18]. Therefore, it is necessary to examine any interfacial strength experiment carefully, as otherwise it might yield meaningless data [9]. For example, the mechanics size effect (related to the stress singularity) might become coupled with the material size effect, and thus lead to complexities in interfacial strength measurement data. Hence, the measured nominal interfacial strengths cannot be used in mechanics predictions because the interfacial properties obtained from laboratory tests are very different from the real values of structures in service (size-dependent). If the free-edge stress singularity were to be successfully removed [21], a question would be whether a uniform interface stress distribution is required to measure the interfacial strength. The current investigation pointed out that the interfacial stress distribution has the least effect on the interfacial strength measurement as long as the stress is not singular. More experimental investigations are needed to verify whether this is a correct statement for all kinds of materials or not. The current work provides design guidance for future development of all interfacial strength approaches.

**Table 1** Measured interfacial bonding strengths (MPa)

Specimen Type	Iosipescu Shear	Short-Beam Shear	Difference
Aluminum-Aluminum	10.75±2.39	10.16±2.41	5.5 %
Polycarbonate-PC	10.99±1.45	8.51±1.13	22.5 %
PMMA-PMMA	11.58±2.15	10.19±0.57	12 %

**Acknowledgements** The authors acknowledge the support from the Office of Naval Research (Program manager Dr. Yapa D.S. Rajapakse) and the National Science Foundation.

## References

1. Daniel IM, Ishai O (2005) Engineering mechanics of composite materials, 2nd edn. Oxford University Press, New York
2. Sun C, Thouless MD, Waas AM, Schroeder JA, Zavattieri PD (2008) Ductile-brittle transitions in the fracture of plastically-deforming, adhesively-bonded structures. Part I: experimental studies. *Int J Solids Struct* 45(10):3059–3073
3. Singh RP, Lambros J, Shukla A, Rosakis AJ (1997) Two optical techniques applied to the investigation of the mechanics of crack propagation along a bimaterial interface. *P R Soc Lond A* 453:2649–2667
4. Xu LR, Rosakis AJ (2002) Impact failure characteristics in sandwich structures. Part II: effects of impact speed and interfacial strength. *Int J Solids Struct* 39:4237–4248
5. Kitey R, Tippur HV (2008) Dynamic crack growth past a stiff inclusion: optical investigation of inclusion eccentricity and inclusion-matrix adhesion strength. *Exp Mech* 48(1):37–54
6. Wang J, Hoagland RG, Hirth JP, Misra A (2008) Atomistic simulations of the shear strength and sliding mechanisms of copper-niobium interfaces. *Acta Mater* 56:3109–3119
7. Bechel VT, Sottos NR (1998) Comparison of calculated and measured debond lengths from fiber push-out test. *Compos Sci Technol* 58:1727–1739
8. Li Z, Bi X, Lambros J, Geubelle PH (2002) Dynamic fiber debonding and frictional pushout in model composite systems: experimental observations. *Exp Mech* 42:417–425
9. Xu LR, Kuai H, Sengupta S (2005) Free-edge stress singularities and edge modifications for fiber pushout experiments. *J Compos Mater* 39(12):1103–1125
10. Rosakis AJ, Samudrala O, Coker D (1999) Cracks faster than the shear wave speed. *Science* 284:1337–1340
11. Xu LR, Huang YY, Rosakis AJ (2003) Dynamic crack deflection and penetration at interfaces in homogenous materials: experimental studies and model predictions. *J Mech Phys Solids* 51:461–486
12. Walrath DE, Adams DF (1983) The Iosipescu shear test as applied to composite materials. *Exp Mech* 23(1):105–110
13. Ho H, Tsai MY, Morton J, Farley GL (1993) Numerical analysis of the Iosipescu specimen for composite materials. *Compos Sci Technol* 46:115–128
14. Grédiac M, Pierron F, Vautrin A (1994) The Iosipescu in-plane shear test applied to composites: a new approach based on displacement field processing. *Compos Sci Technol* 51:409–417
15. Melin LN, Neumister JM (2006) Measuring constitutive shear behavior of orthotropic composites and evaluation of the modified Iosipescu test. *Compos Struct* 76:106–115
16. El-Hajjar R, Haj-Ali R (2004) In-plane shear testing of thick-section pultruded FRP composites using a modified Arcan fixture. *Compos B* 35:421–428
17. Xu LR, Sengupta S, Kuai H (2004) An experimental and numerical investigation of adhesive bonding strengths of polymer materials. *Int J Adhes Adhes* 24:455–460
18. Xu LR, Kuai H, Sengupta S (2004) Dissimilar material joints with and without free-edge stress singularities: Part I. A biologically inspired design. *Exp Mech* 44(6):608–615
19. Kobayashi AS (ed) (1987) Handbook on experimental mechanics. Society of Experimental Mechanics, Inc. Prentice-Hall, New Jersey
20. Krishnan A (2008) Comparison of interfacial shear strength measurements for bonded materials and composite materials. MS Dissertation, Vanderbilt University
21. Wang P, Xu LR (2006) Convex interfacial joints with least stress singularities in dissimilar materials. *Mech Mater* 38:1001–1011

Submitted to *International Journal of Fracture* (2010)

## An efficient approach to measure the Mode II fracture toughness of materials with preferred interfaces

*Arun Krishnan and L. Roy Xu\**

Department of Civil and Environmental Engineering

and Materials Science Program

Vanderbilt University

Nashville, TN 37235, USA

### **Abstract**

In this paper, an efficient method to characterize the mode II fracture toughness,  $K_{IIC}$  of materials with preferred interfaces such as wood, fiber composite materials and bonded materials based on the Iosipescu fixture is developed. Our method is easy to implement and is free of friction between the cracked faces thereby offering a more reasonable value of  $K_{IIC}$  than previous methods. Another feature of our new approach is the measurement of accurate crack initiation load. Additionally, a calibration chart for composite materials is generated. Finite element analysis along with cohesive elements is used to validate experimental load-displacement curves which are obtained by testing bonded polymers.

### **1. Introduction**

The mode II fracture toughness has long been a difficult property to quantify for isotropic materials as a mode II crack tends to kink away from the main crack (Anderson, 2004), and thereby makes the measured fracture toughness indeed the mode I fracture toughness. A mode II crack is possible only for special materials with preferred interfaces like wood, bonded materials or composite materials. For unidirectional composite materials with fiber/matrix interfaces, a

---

\* Corresponding author, E-mail: [luoyu.r.xu@gmail.com](mailto:luoyu.r.xu@gmail.com)

mode II crack is possible due to the strong constraining of fibers to suppress any kinked cracks, as has been shown in recent dynamic shear crack experiments by Coker and Rosakis (2001). Therefore, several experimental approaches have been proposed to measure the mode II interlaminar fracture toughness of fiber-reinforced composite materials such as the end-notched flexure test (Daniel and Ishai, 2005). But, these beam bending tests usually require numerical procedures like data reduction methods to correct for the shear and crack tip deflection (Yoshihara and Satoh, 2009). These issues tend to complicate the experimental measurement of the mode II fracture toughness which is a fundamental material property.

A critical issue in beam bending experiments in conjunction with Linear Elastics Fracture Mechanics (LEFM) analysis is the significant absence of the “K-dominance zone” in these thin composite beams (Rosakis and Ravi-Chandar, 1986; Sun, 2008; Qian and Sun, 2008; Sun and Qian, 2009). On the other hand, most of these beam bending methods are unable to eliminate friction between the cracked faces, behind the crack tip. This can cause a significant increase in values of  $K_{IIC}$  which become higher than the intrinsic values. For other non-beam bending methods, it has been shown that the compressive stresses ahead of the crack tip significantly affect the mode II fracture toughness of composite materials (Bing and Sun, 2007). Also, the values of the measured mode II fracture toughnesses are strongly dependent on the type of test used and show a wide variation. With the extensive applications of composite materials, it is very important to develop new approaches to measure the mode II fracture toughnesses.

The losipescu shear test has been developed and extensively modified to measure the shear strength of composites and bonded polymers (Walrath and Adams, 1983). This fixture has been

used to characterize the shear strength of short-beam shear specimens; and the average shear strengths are found to be very close to the shear strengths of the Iosipescu shear specimens in spite of very different interfacial shear stress distributions (Krishnan and Xu, 2010). In this investigation, the advantage of having zero interfacial normal stress (zero bending moment) at the specimen center is used to develop an efficient experimental method in determining the mode II fracture toughness of bonded polymers. This method, which is based on the Iosipescu fixture, minimizes the effect of friction on the mode-II fracture toughness. A theoretical formula is derived and is verified using finite element analysis. This formula is extended to include composite materials and a calibration chart is provided. Experimental specimens of bonded polymers are tested to measure fracture toughness values and the load-displacement curves are verified numerically using cohesive element simulation. Indeed, Bansal and Kumosa (1998) have proposed a “Double Edge-Crack” Iosipescu shear specimen to measure the mixed-mode fracture toughness of composite materials subjected to biaxial loads. The current objective, however, is to measure the mode-II fracture toughness alone with our approach, which is much easier to use than previous ones.

## **2. Theoretical Background**

### **2. 1 Formula for the homogenous materials**

The stress intensity factors of an asymmetric four-point bend specimen (Fig. 1) have been calculated by Suresh et al., (1990)

$$K_I = 6\tau\sqrt{\pi a} \frac{S}{W} F_I\left(\frac{a}{W}\right) \quad (1)$$

$$K_{II} = \tau\sqrt{\pi a} F_{II}\left(\frac{a}{W}\right) \quad (2)$$

Where  $K_I$  and  $K_{II}$  are the mode I and mode II stress intensity factors respectively;  $\tau$  is the shear stress across the interface,  $W$  is the specimen width,  $a$  is the crack length and  $S$  is the off-set distance between the crack plane and the loading point.  $F_I$  and  $F_{II}$  are dimensionless functions of  $a/W$  and are provided in Suresh et al. (1990). Additionally, the shear stress per unit thickness can be expressed as

$$\tau = \frac{P}{W} \frac{A - B}{A + B} \quad (3)$$

Here,  $P$  is the applied load,  $A$  and  $B$  are distances of the loading points from the center as shown in Fig.1.

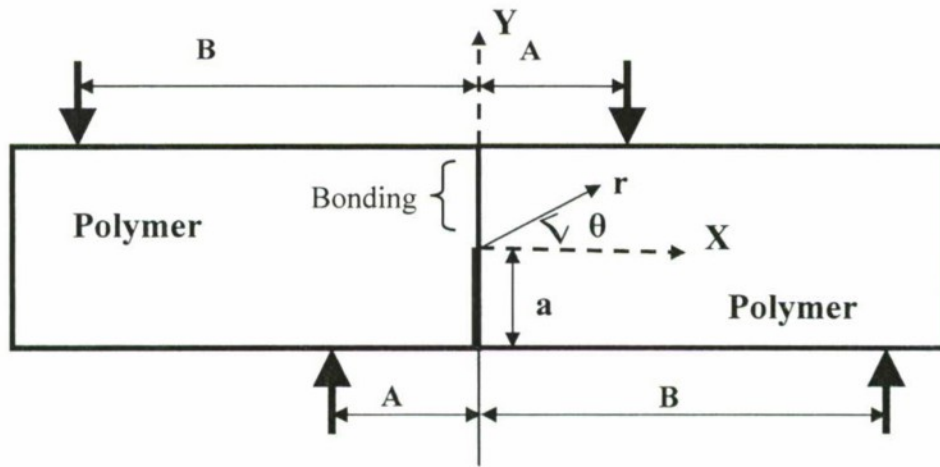


**Fig. 1** Schematic diagram of the short-beam shear test with equivalent applied loading at distances  $A$  and  $B$

In this investigation, a short-beam shear specimen with a bonded interface is chosen to match those dimensions required for a widely used Iosipescu test fixture (Krishnan and Xu, 2010). The short-beam shear test is indeed an anti-symmetric four point bend test. We choose specific

adhesives with similar Young's modulus as the bonded polymers ( $E=1-5\text{GPa}$ ). Also, the actual thickness of the adhesive interface is only of the order of the micrometers, which is negligible in comparison with other dimensions of the specimen. Thus, the same-material bonded specimen is treated as homogenous materials, however is not isotropic as the strength along the adhesive interface will be different from the strength of the bulk material. The loads on the Iosipescu fixture are applied in the form of displacements on anti-symmetric loading blocks. The corresponding loads are not point loads and are applied from the loading blocks in the form of highly non-linear line loads. However, these loads can be expressed as equivalent point loads acting at a specific distance from the center line as shown in Fig. 1. For a short-beam shear specimen,  $A$  and  $B$  are calculated to be 16 mm and 34.5 mm for isotropic materials. These values are calculated from finite element simulations with the corresponding procedure outlined in Section 4. In every case the moment about the center line (along the interface) is calculated to be zero which is critical in ensuring that  $S$  from equation (1) is zero. The short-beam set-up works perfectly well for the case of the pure mode II determination of same-material specimens due to the fact that the moment about its center line is always zero based on static balance analysis.

In the present case, there is no off-set of the loads from the center; therefore  $S$  is 0. Hence,  $K_I$  is 0 and we obtain a pure mode II condition. Further, from equations (2) and (3), we obtain a formula for  $K_{II}$  as

$$K_{II} = \frac{P}{Wt} \frac{A-B}{A+B} \sqrt{\pi a} F_{II}\left(\frac{a}{W}\right) \quad (4)$$

Here,  $t$  is the thickness of the specimen. Also, in the present case, we use  $a/W$  of 0.5 for the convenient purpose of specimen preparations. This gives a  $F_{II}$  value of 1.3 (Suresh et al. 1990). Hence, equation (4) can be further expressed as

$$K_{II} = 1.3 \frac{P}{Wt} \frac{A-B}{A+B} \sqrt{\pi a} \quad (5)$$

Now, the energy release rate  $G_{II}$  can be expressed as

$$G_{II} = \frac{K_{II}^2}{E^*} \quad (6)$$

Here,  $E^*$  is the effective plane elastic modulus for both plane stress and strain cases. Combining equations (5) and (6), the critical energy release rate  $G_{IIC}$  can be expressed as

$$G_{IIC} = \frac{1.69}{E^*} \left( \frac{P_C}{W} \right)^2 \left( \frac{A-B}{A+B} \right)^2 \frac{\pi a}{t^2} \quad (7)$$

where  $P_C$  is the critical load at the crack initiation in the specimen. Applying the values of  $A$  and  $B$  for our new type of experiments as shown in Fig.1, we get,

$$G_{IIC} = \frac{0.7125}{E^*} \left( \frac{P_C}{W} \right)^2 \frac{a}{t^2} \quad (8)$$

The applicability of equation (8) is tested over a wide range of elastic moduli and applied displacements. This validity is checked by obtaining values of  $A$  and  $B$  over a variety of elastic moduli and applied displacements. As shown in Fig.2, values of  $A$  and  $B$  remain constant for a wide range of Young's moduli (at a constant applied displacement of 0.2 mm), thereby showing that equation (5) is valid for most engineering materials. Fig. 3 shows there is no variation in  $A$  and  $B$  with different applied displacement at a constant elastic modulus of 2.4 GPa (Young's modulus of polymer materials in this investigation).

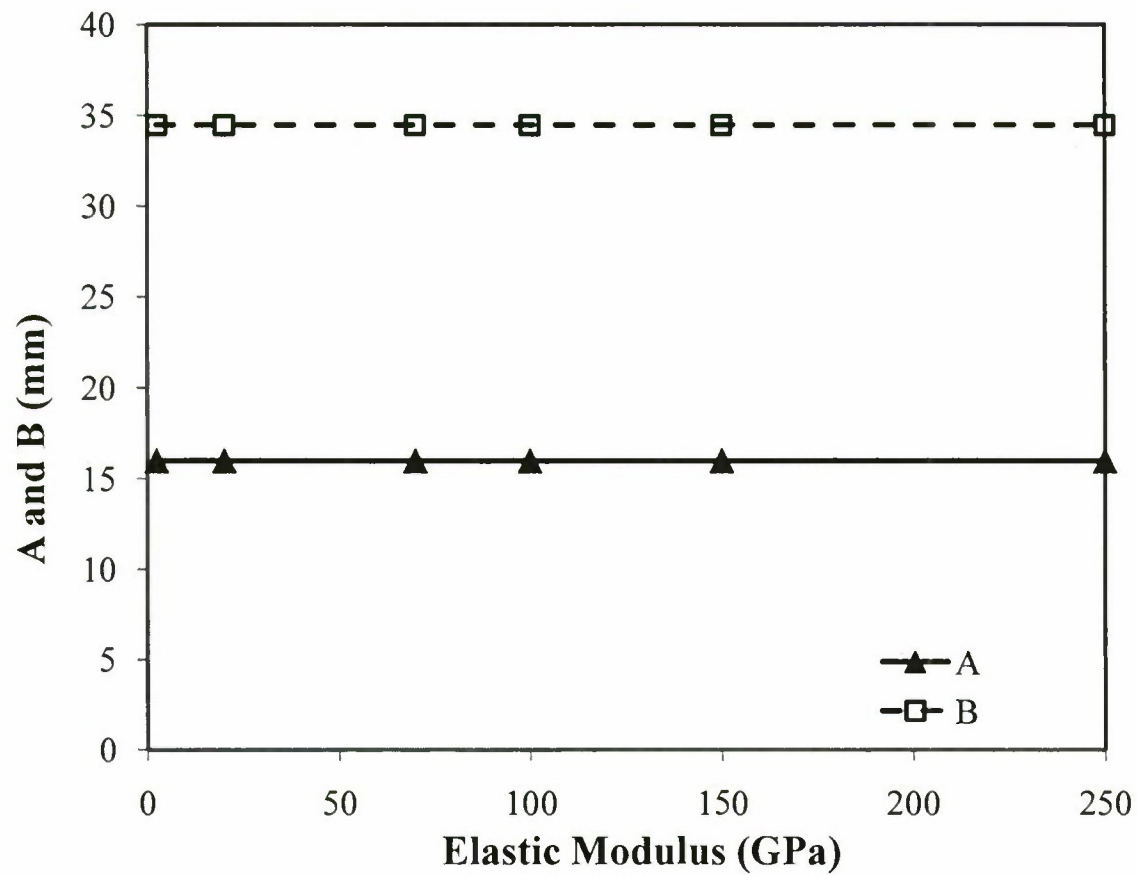


**Fig. 2** Finite element analysis results showing very small variations of  $A$  and  $B$  with a wide range of elastic moduli under an applied displacement of 0.2 mm

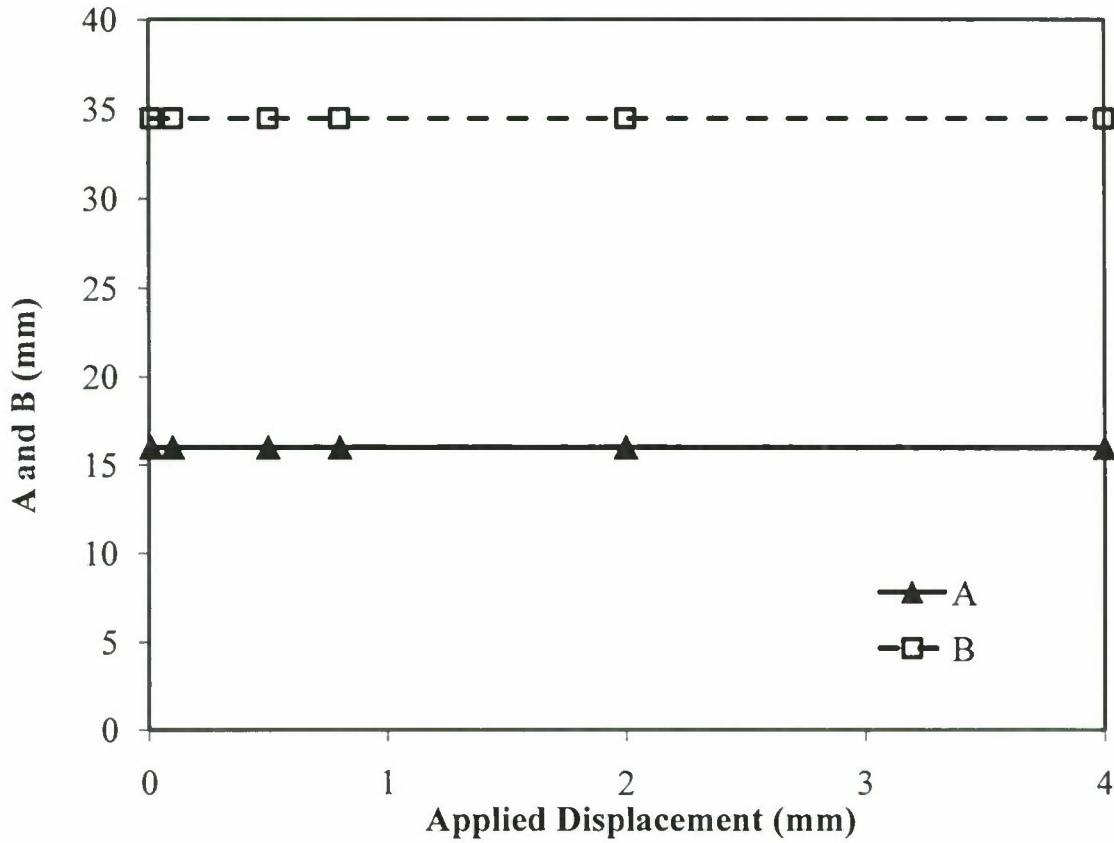


**Fig. 3** Finite element analysis results showing very small variations of  $A$  and  $B$  with a wide range of applied displacements for polymeric specimen with an elastic modulus of 2.4 GPa

## 2.2 Formula for orthotropic fibrous composite materials

The above discussion can be extended to orthotropic materials such as unidirectional fiber composite materials as shown in Fig. 4. A similar analysis to determine the fracture toughness of composite materials is conducted. First, the effective plane elastic modulus of the composite materials is calculated by using the formula presented below (Sih et al., 1965; Xu et al., 1996)

$$\frac{1}{E^*} = \frac{1}{\sqrt{2}E_{22}} \sqrt{\sqrt{\frac{E_{22}}{E_{11}}} + \left( \frac{1}{G_{12}} - \frac{2\nu_{12}}{E_{11}} \right) \frac{E_{22}}{2}} \quad (9)$$

Here,  $E_{11}$  and  $E_{22}$  are the elastic moduli of the composite in the fiber (longitudinal) and transverse directions. In this investigation, the mode-II crack path should be the same direction with the fiber, or equivalently the fibers should be along the y direction. The local 1-2 coordinate system is shown in Fig. 4.  $G_{12}$  is the shear modulus of the composite and  $\nu_{12}$  is the Poisson's ratio of the composite. The fracture toughness can then be calculated by using the same relationship in equation (6), but by using the effective Young's modulus of the composites. The values of  $A$  and  $B$  in case of composites are calculated from finite elements to be 15.5 mm and 32.5 mm and are found to be slightly different from same-material specimens. In order to determine values of  $A$  and  $B$  the loads on the specimen are calculated using finite elements. A similar approach as in case of same-material specimens is used. The equivalent loading points for  $A$  and  $B$  are found to be constant and are plotted against the ratio of the typical composite elastic moduli  $E_{11}$  and  $E_{22}$  in Fig. 5.

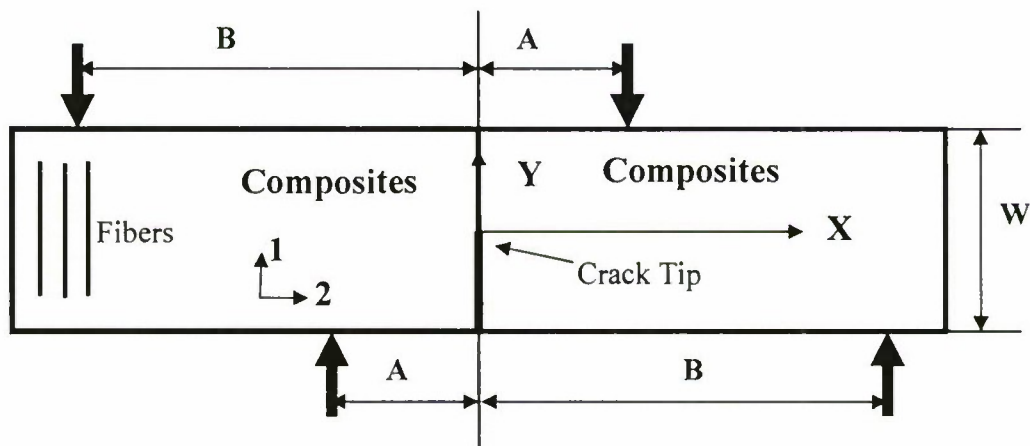


**Fig. 4** Schematic diagram of a short-beam shear specimen for unidirectional composite materials

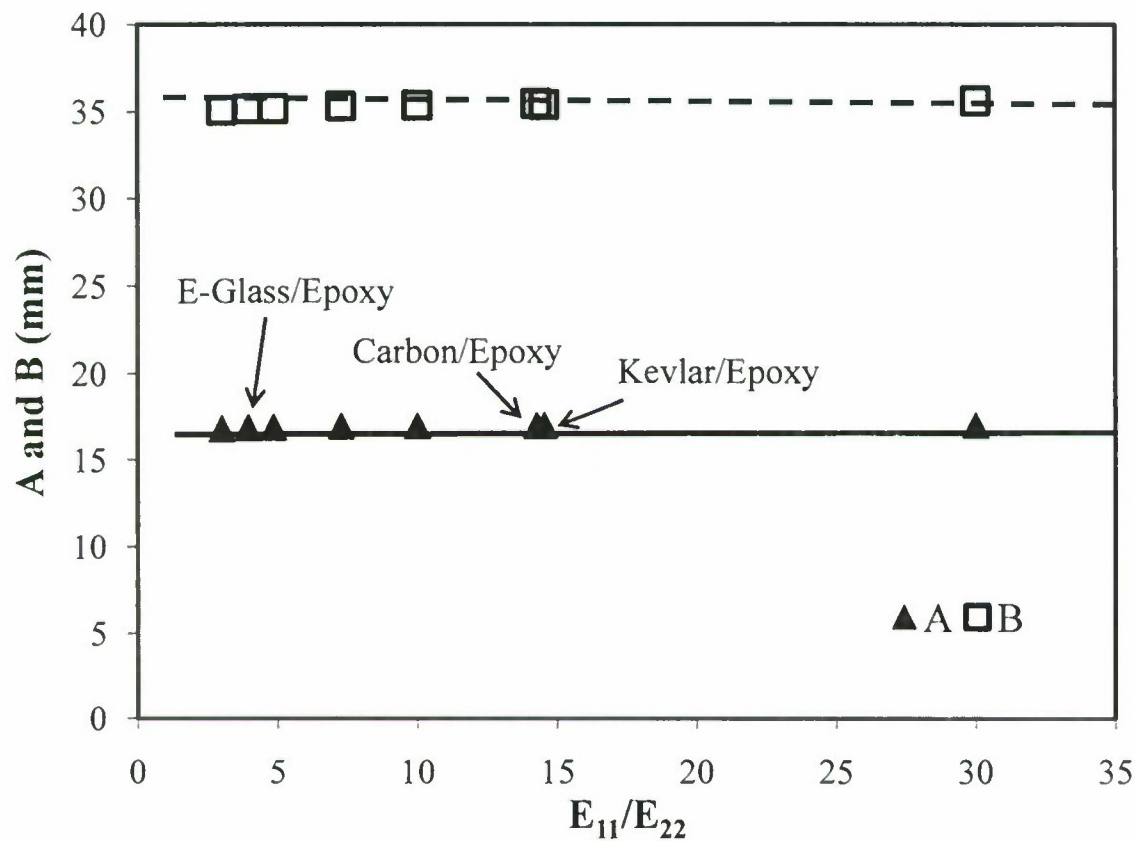


**Fig. 5** Finite element analysis results showing very small variation in  $A$  and  $B$  with elastic modulus ratio for different types of orthotropic composite materials.

### 3. Experimental investigation

#### 3.1 Specimen preparation and test procedure

Specimens were made of polycarbonate and PMMA. Each specimen was made of two individual halves of length 38.1 mm and width (W) 19.1 mm and was bonded at the interface using an adhesive to enable interfacial failure. Each specimen had a thickness of 5.5 mm. The bonding surfaces of the individual halves were sand-blasted to improve the bonding quality. While Weldon-10 was used to provide strong bonding, Loctite 384 was used to provide weak bonding. These adhesives were specifically chosen such that their elastic modulus when cured was close

to that of polycarbonate and PMMA (2-4 GPa). This was done to simplify the mechanics of the polymer/adhesive/polymer interface. Each specimen had an initial crack ( $a/W=0.5$ ) which was made by covering one half of the adhesive using a thin tape. The adhesive was then applied to the other half and the specimen was bonded using a special fixture to guarantee dimensionality. The specimens were left to cure for a period of 24 hours to achieve the bonding strength.

The experimental set-up consisted of three parts including a mechanical system to load the specimens, an optical system to capture fringe patterns and an imaging set-up to record the images (Xu et al., 2004a). The fringes were solely used to observe the failure process and to determine the crack path. The mechanical system consisted of a MTS 810 test machine and an Iosipescu fixture. Load was applied to the movable part of the Iosipescu fixture in the form of displacements at a rate of 1 mm/min until failure. About seven specimens were tested to ensure repeatability.

### **3.2 Experimental Results for $G_{IIC}$**

The experimental results are presented in Table 1. Two fracture modes were observed: 1) if the interfacial bonding was strong, the initial crack, although loaded in shear, kinks from the original crack path and forms a mode-I crack (its symmetrical stress field was verified by optical techniques); and 2) a pure mode-II crack propagates along the interfacial bonding (a self-similar crack) if the interfacial bonding was weak. However, in case of the strongly bonded polycarbonate specimens, kinking starts away from the crack tip. The crack was observed (during the experiment by optical methods and after failure by observation of the failure surfaces) to originate as a mode II crack and then kink away as a mode I crack. Hence, it is concluded that the intrinsic mode II fracture toughness for polycarbonate specimens is obtained.

In case of PMMA, the crack was observed to kink from the crack tip itself. So, a lower bound for the  $K_{IIC}$  value is obtained, and not the mode II fracture toughness, as indicated in Table 1.

**Table. 1** Experimental results for same-material specimens

Bonded materials	Bonding	Crack initiation load (N)	$K_{IIC}$ (MPa m <sup>0.5</sup> )	$G_{IIC}$ (J/m <sup>2</sup> )
Polycarbonate	Weak	$417 \pm 49$	$0.33 \pm 0.04$	45.8
Polycarbonate	Strong	$1002 \pm 57$	$0.76 \pm 0.05$	260.8
PMMA	Weak	$451 \pm 100$	$0.35 \pm 0.08$	34.6
PMMA	Strong	$975 \pm 81$	$\geq 0.77 \pm 0.06$	$\geq 155.6$

The values of  $K_{IIC}$  are seen to be equal or less than the values of  $K_{IC}$  for the same material types obtained from our previous experimental research (Krishnan and Xu, 2009). This indicates that there is less friction between the cracked faces obtained in our experiments.

### 3.3 Analysis on the crack kinking

An initial crack seeks the path of least resistance to propagate (Anderson, 2004). In the present case, a pure mode II crack is needed, rather than a kinked mode I crack. The angle of the crack kinking can be calculated theoretically (Erdogan and Sih, 1963; Williams and Ewing, 1972). The kinking angle has been calculated for a mixed mode case by Bhattacharjee and Knott (1995). A schematic diagram of crack kinking along with the conventions is shown in Fig. 6. The criterion for an initial crack to kink along an angle can be expressed as

$$\frac{\partial \sigma_{\theta\theta}}{\partial \theta} = 0, \quad \frac{\partial^2 \sigma_{\theta\theta}}{\partial \theta^2} < 0 \quad (10)$$

Where the shear stress is zero and the hoop stress is maximized. The hoop stress and shear stress close to a crack tip can be expressed in polar coordinates as (Anderson, 2004)

$$\sigma_{\theta\theta} = \frac{K_{II}}{\sqrt{2\pi r}} \left( -\frac{3}{4} \sin\left(\frac{\theta}{2}\right) - \frac{3}{4} \sin\left(\frac{3\theta}{2}\right) \right) \quad (11)$$

$$\tau_{r\theta} = \frac{K_{II}}{\sqrt{2\pi r}} \left( \frac{1}{4} \cos\left(\frac{\theta}{2}\right) + \frac{3}{4} \cos\left(\frac{3\theta}{2}\right) \right) \quad (12)$$

The condition in equation (10) is solved for  $\theta$  and the predicted angle of the kink is calculated as 19.5° from the x-axis. This is close to the angle of kink obtained experimentally from polycarbonate and PMMA. It should be noted that the kinking angle is independent of the material used if the T-stress is neglected. The effect of the T-stress before and after crack kinking has been reported by Li and Xu (2007). A typical strongly bonded polycarbonate specimen showing a kinking angle of about 25° from the x-axis is presented in Fig. 7.

In order to predict which failure mode will occur at first, the energy release rates and fracture toughnesses of two failure modes should be compared (Hutchinson and Suo, 1992; Xu and Rosakis, 2003; Xu et al., 2003). The energy release rate of the initial crack is a function of the potential crack path or a function of  $\theta$ . For the kinked mode-I crack, the energy release rate,  $G(\theta=\theta_c)$  should exceed the mode-I fracture toughness of the polymer material  $\Gamma_{IC}^{PM}$ , i.e.,

$$\frac{G(\theta = \theta_c)}{\Gamma_{IC}^{PM}} \geq 1 \quad (13)$$

Where the crack kinking angle  $\theta_c$  is around  $20^\circ$  from the x axis based on Erdogan and Sih (1963).

For the pure mode-II crack initiation and propagation, the energy release rate,  $G(\theta=90^\circ)$  should

exceed the mode-II fracture toughness of the interface  $\Gamma_{IIc}^{IT}$ , i.e.,

$$\frac{G(\theta = 90^\circ)}{\Gamma_{IIc}^{IT}} \geq 1 \quad (14)$$

So, the competition of the energy release rate and the fracture toughness leads to different failure modes. Here, if equation (13) is satisfied at first, a crack loaded in shear will kink as a mode-I crack. If equation (14) is satisfied at first, a crack loaded in shear will propagate as a mode-II crack along the interface.

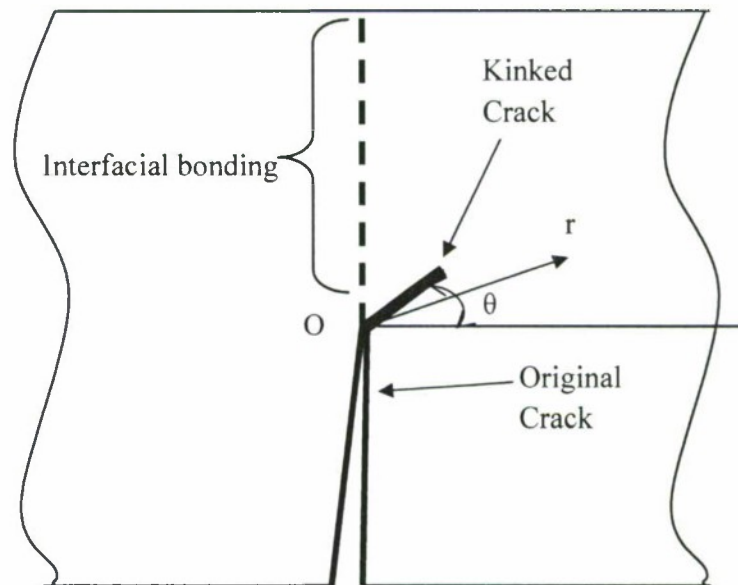


**Fig. 6** Schematic diagram showing the crack kinking

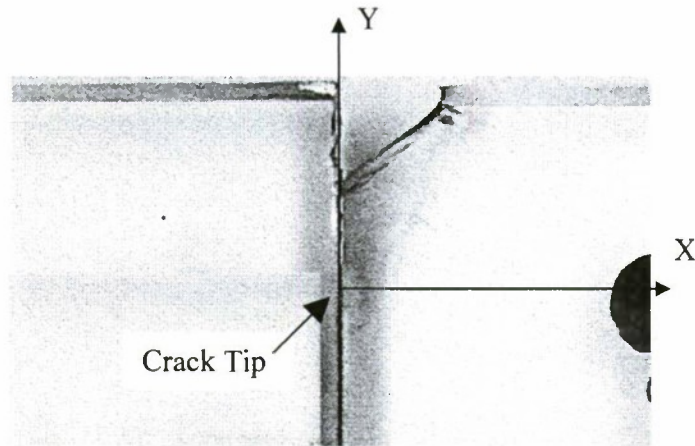


**Fig. 7** Picture of a typical strongly bonded polycarbonate specimen showing crack kinking from the interface

#### 4. Numerical Methods

##### 4.1 Finite element model to compare with formula for same-material specimens

A two-dimensional finite element analysis was conducted using Abaqus® 6.9.1. The mesh is progressively graded in order to reduce computational cost, and is refined near the crack tip to best capture the stress singularity. Polycarbonate specimens with an elastic modulus of 2.4 GPa and a Poisson's ratio of 0.37 are chosen for the analysis. The dimensions of the model are the same as the experimental specimens as described in Section 2. The geometry of each individual part is symmetric while the loading on the material is anti-symmetric. The model is assumed to be monolithic with the zero thickness of the adhesive layer.

The loading is applied in the form of loading block on the specimen edges similar to what is observed in reality. In order to incorporate a realistic simulation of the loads on the specimen an iterative procedure is adopted (Xu et al., 2004b; Krishnan and Xu, 2010). The loads in the form of displacements are applied to the movable part of the specimen while the other part is held

fixed. After each analysis the reaction forces on the loading edges are checked to see if they are in compression or not, because in experiments, only compressive loading is observed. The constraints are removed from those nodes which showed tensile reaction forces and the analysis is repeated until convergence. The stress intensity factors,  $K_I$  and  $K_{II}$  are calculated from the finite element analysis and are compared with the results from equation (5). The results are presented in Table 2. It can be seen that the  $K_I$  is negligibly small in comparison with  $K_{II}$  as is expected from the theoretical results presented earlier. Also, the values of  $K_{II}$  from finite element analysis agree well with the values calculated from our formula for same-material specimens. This validates our theoretical formula for same-material specimens.

**Table 2.** Variation of mode I and mode II stress intensity factors  $K_I$  and  $K_{II}$  with applied load for same-material polycarbonate specimen

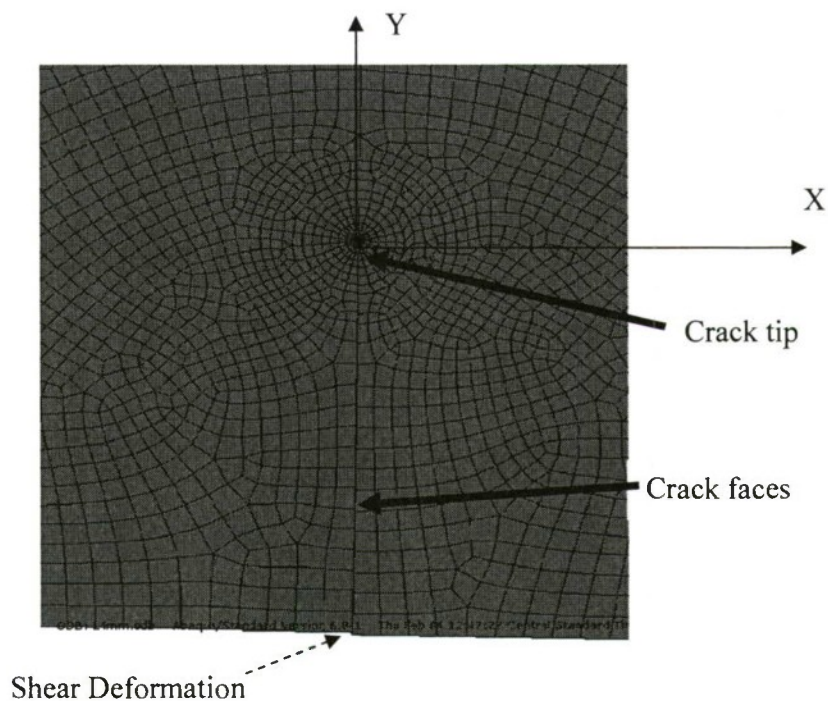
Load (N)	Finite Element Analysis		Formula	
	$K_I$ (MPa $m^{0.5}$ )	$K_{II}$ (MPa $m^{0.5}$ )	$K_I$ (MPa $m^{0.5}$ )	$K_{II}$ (MPa $m^{0.5}$ )
135	0.0019	0.1067	0	0.1060
405	0.0057	0.3199	0	0.3179
675	0.0097	0.5333	0	0.5299
1350	0.019	1.067	0	1.0598

A snapshot of the deformed mesh near the crack tip at failure load is presented in Fig. 8. It can be seen that there is no crack surface separation (opening mode-I), and only sliding along the crack face (shear mode-II). This confirms that there is no mode I component from our finite element analysis. The shear and normal stresses along the interface at a failure load of 1000 N are plotted in Fig. 9. The graph demonstrates the singularity of the stresses at the crack tip. Also, there is no

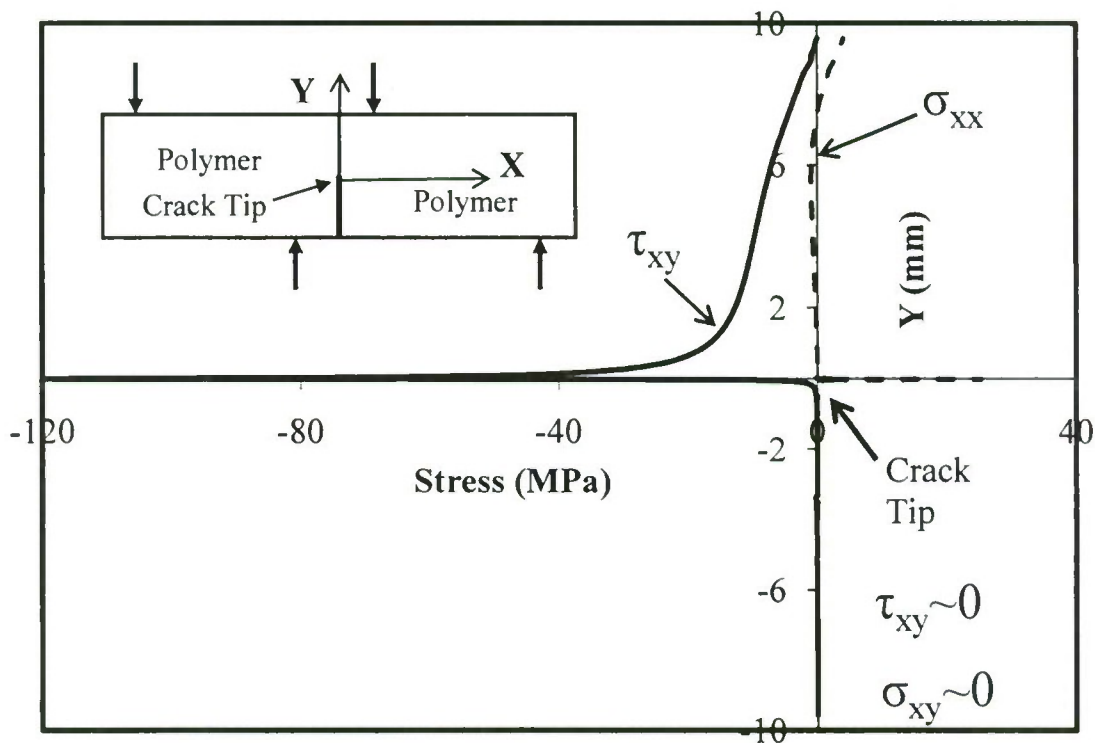
contact between the crack lips indicating that there is little friction involved during experiments.

Fig. 10 shows a comparison of shear stresses along the crack faces for different loading cases.

These values are seen to be close to zero even at higher loads (beyond failure loads) demonstrating the absence of friction between the crack faces.



**Fig.8** Snapshot of deformed mesh (near the crack tip) at failure load. This mesh is used for modeling short-beam shear specimen



**Fig.9** Variation of shear stress and normal stress along the interface for polycarbonate same-material bonding at a failure load of 1000 N.

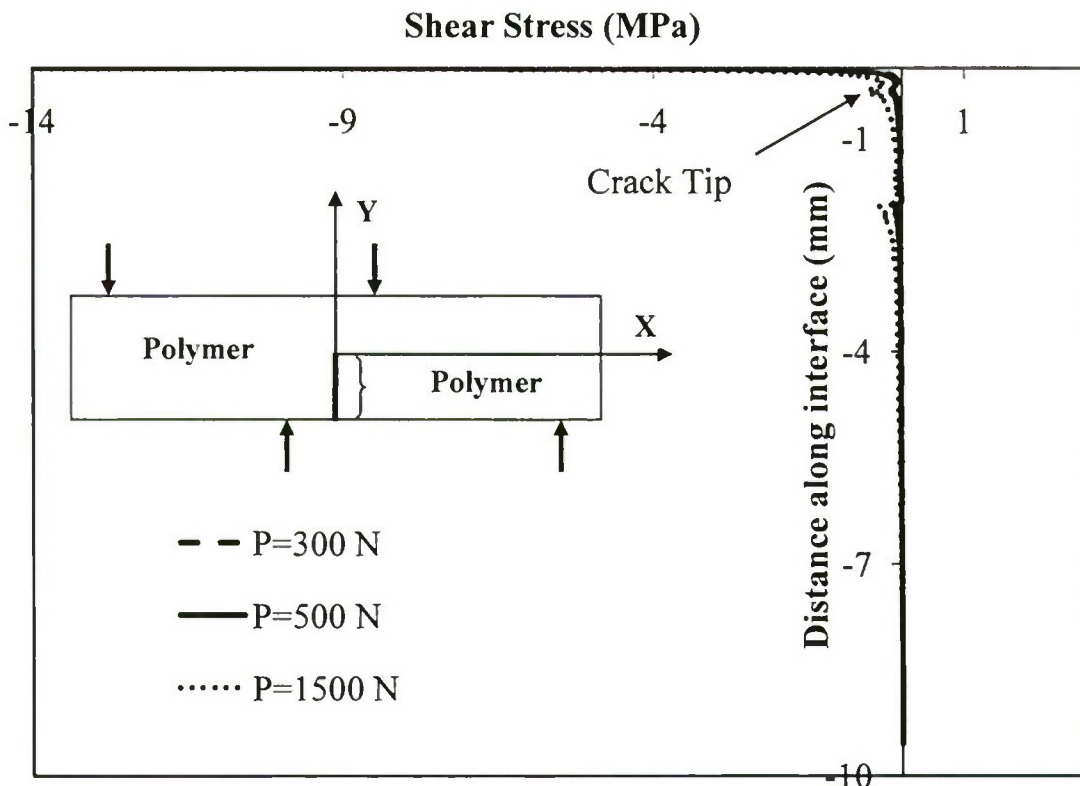


**Fig. 10** Variation of shear stresses along the interface for polycarbonate same-material bonding with increase in applied loading. There is negligible friction observed beyond the crack tip.

#### 4.2 Numerical modeling for composites

A similar model as described in above is made for composite materials with fiber direction along the y-direction as shown in Fig.4. This type of unidirectional composite materials ensures that the mode-II crack will not kink and will propagate along the fiber-matrix interface due to strong constraint of the fiber. Three kinds of typical composite material data are chosen from Daniel and Ishai (2005) to conduct the numerical analysis (Table 3).

However, in case of orthotropic unidirectional composite materials, we do not have the graph of  $F_{II}$  which has been provided for same-material specimens by Suresh et al. (1990) and for bi-

material specimens by O'Dowd et al. (1992). Hence, the plot of  $F_{II}$  as a function of  $a/W$  is calculated for three different types of composite materials, viz. E-Glass/Epoxy (55 % volume percent of fibers, unidirectional GFRP), Kevlar 49/Epoxy (60% volume percent of fibers, unidirectional KFRP) and AS4/3501-6 Carbon/Epoxy (63% volume percent of fibers, unidirectional CFRP). The plot of  $F_{II}$  as a function of  $a/W$  is presented in Fig. 11. It is seen that this plot is almost constant for these three types of typical composites. While calculating the mode II stress intensity factors for composites, this chart becomes necessary to use the current approach and is complementary to the one presented in Suresh et al. (1990). Also, the numerically calculated values of  $K_I$ ,  $K_{II}$  and  $F_{II}$  at different values of  $a/W$  ratios are presented in Table 4 for the three typical composite types chosen. The ratio of  $K_I/K_{II}$  remains negligibly small indicating that the crack is indeed a pure mode II crack in unidirectional composites. The applied loads on each composite specimen (corresponding to a fixed applied displacement of 0.5 mm) are also presented in Table 4. The different types of composites take different loads (in spite of a fixed applied displacement) due to their different elastic properties. However, the dimensionless stress intensity factor,  $F_{II}$ , remains very similar for the different kinds of composites.

**Table 3.** Properties for three typical composites (Daniel and Ishai, 2005)

Materials	Fiber volume percent (%)	$E_{11}$ (GPa)	$E_{22}$ (GPa)	$G_{12}$ (GPa)	$G_{23}$ (GPa)	$v_{12}$	$v_{23}$
Carbon/Epoxy	63	147	10.3	7	3.7	0.27	0.54
E-Glass/Epoxy	55	41	10.4	4.3	3.5	0.28	0.5
Kevlar/Epoxy	60	80	5.5	2.2	1.8	0.34	0.4

**Table 4.** Variation of  $F_{II}$  with  $a/W$  for different types of composites.  $K_I$  and  $K_{II}$  are expressed in MPa m<sup>1/2</sup> (A=15.49 mm, B=32.44 mm)

## CFRP

<b>a/W</b>	<b>Load (N)</b>	<b><math>K_I</math>(MPa m<sup>1/2</sup>)</b>	<b><math>K_{II}</math>(MPa m<sup>1/2</sup>)</b>	<b><math>K_{II}/K_I</math></b>	<b><math>F_{II}</math></b>
0.2	1009	0.0124	1.2412	0.0099	0.3836
0.3	1008	0.0090	2.1345	0.0042	0.6603
0.4	1004	0.0026	3.0042	0.0009	0.933
0.5	1001	0.0006	3.8580	0.0001	1.2018
0.6	991	0.0083	4.7118	0.0018	1.4825
0.7	979	0.0146	5.6605	0.0026	1.8029

## GFRP

<b>a/W</b>	<b>Load (N)</b>	<b><math>K_I</math>(MPa m<sup>1/2</sup>)</b>	<b><math>K_{II}</math>(MPa m<sup>1/2</sup>)</b>	<b><math>K_{II}/K_I</math></b>	<b><math>F_{II}</math></b>
0.2	709	0.0405	0.9645	0.0419	0.4242
0.3	708	0.0281	1.6286	0.0173	0.7173
0.4	704	0.0072	2.2927	0.0031	1.0155
0.5	698	0.0095	2.9410	0.0032	1.3138
0.6	687	0.0263	3.5418	0.0075	1.6075
0.7	671	0.0361	4.2058	0.0086	1.9544

## KFRP

<b>a/W</b>	<b>Load (N)</b>	<b><math>K_I</math>(MPa m<sup>1/2</sup>)</b>	<b><math>K_{II}</math>(MPa m<sup>1/2</sup>)</b>	<b><math>K_{II}/K_I</math></b>	<b><math>F_{II}</math></b>
0.2	420	0.0058	0.5139	0.0113	0.3815
0.3	420	0.0039	0.8854	0.0044	0.6573
0.4	418	0.0006	1.2491	0.0005	0.9318
0.5	417	0.0004	1.6128	0.0003	1.2059
0.6	413	0.0043	1.9606	0.0022	1.4802
0.7	408	0.0063	2.3401	0.0027	1.7884

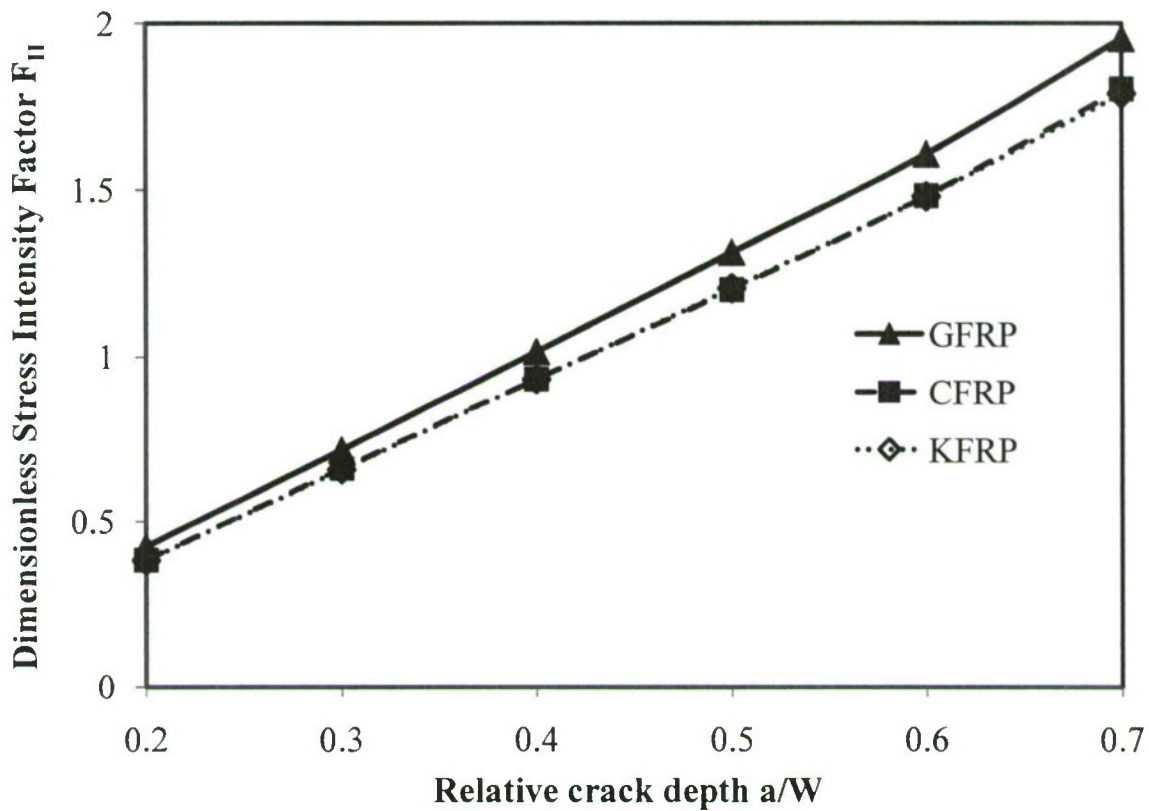


**Fig. 11** Variation of dimensionless stress intensity factor  $F_{II}$  with relative crack depth for different types of composites.

#### 4.3 Cohesive element simulation

In order to simulate the experimental load-displacement curves and the failure load, a cohesive element analysis is employed. Cohesive elements are exclusively used along the bonded interface in order to model the failure process. Cohesive elements with zero thickness are used in the model. A bi-linear cohesive law is considered for this case and a representative law for strongly bonded polycarbonate is shown in Fig. 12. Such types of cohesive laws have been used successfully in the past to model mixed mode failure in brittle materials (Camacho and Ortiz, 1996; Ruiz et al., 2001). The four types of specimens in Table 1 are modeled using a similar

bilinear cohesive law but with different values of constants (shown in Fig. 12). The value of fracture toughness,  $G_{IIc}$ , obtained from the current experimental results (Table 1) is used here and equals the total area enclosed by the cohesive law. The elastic modulus of the bulk material is used as the slope of the initial linear part of the traction separation law. The maximum value of traction ( $\tau$ ) is obtained from our previous measurements for interfacial shear strengths of bonded polycarbonate systems (Krishnan and Xu, 2009). The critical opening displacement ( $\delta_c$ ) can then be calculated from these known values. The finite element model used is similar to the one described in the previous sections except in the inclusion of the cohesive elements. Loads are then applied to the finite element model as described previously. The simulated load-displacement curves are plotted along with the experimental load-displacement curves in Fig. 13. Three different experimental curves are shown to depict the variation in the experiments. The cohesive element model is seen to capture the initial slope of the experimental load-displacement curves. There is only a reasonable amount of error for the value of the final failure load as shown by the cohesive model. A similar analysis, albeit with a different cohesive law, is carried out for weakly bonded polycarbonate specimens and the corresponding results are shown in Fig. 14. Different values of fracture toughness and maximum traction are used in this case and these data were from our previous measurement for the same material system. This model predicts the crack initiation load and failure displacement with a reasonable amount of error. The graphs in Figs. 13 and 14 are plotted on the same scale to allow for a fair comparison between the crack initiation loading of the strong and the weak bonds.

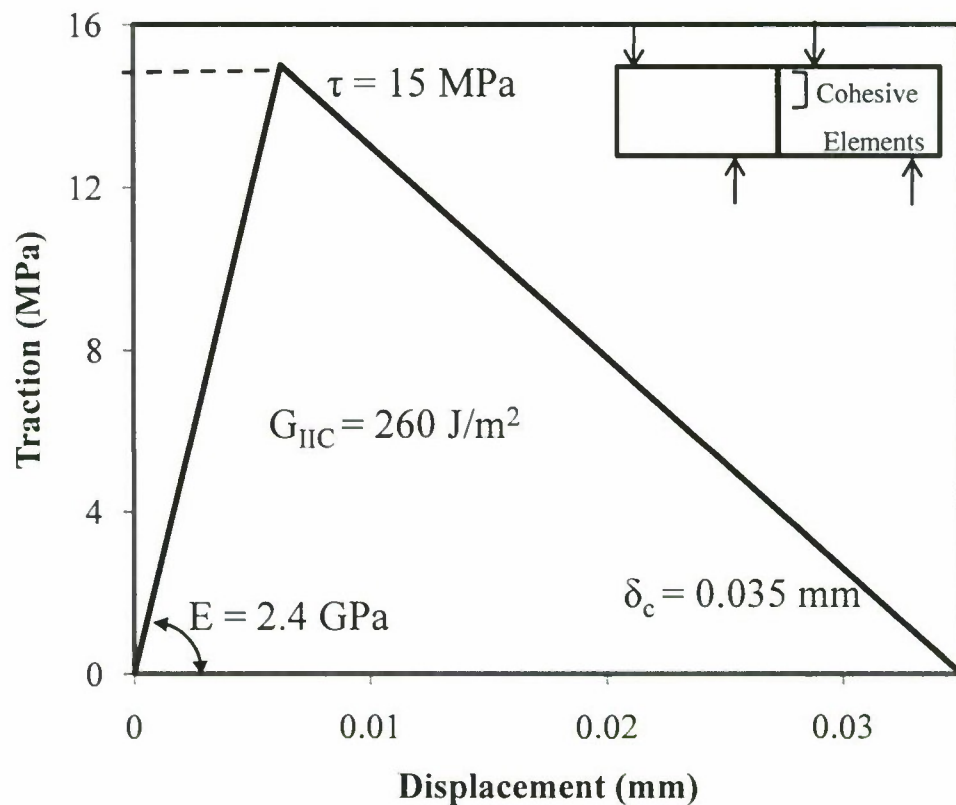


**Fig. 12** Traction-Separation law used for strongly bonded Polycarbonate

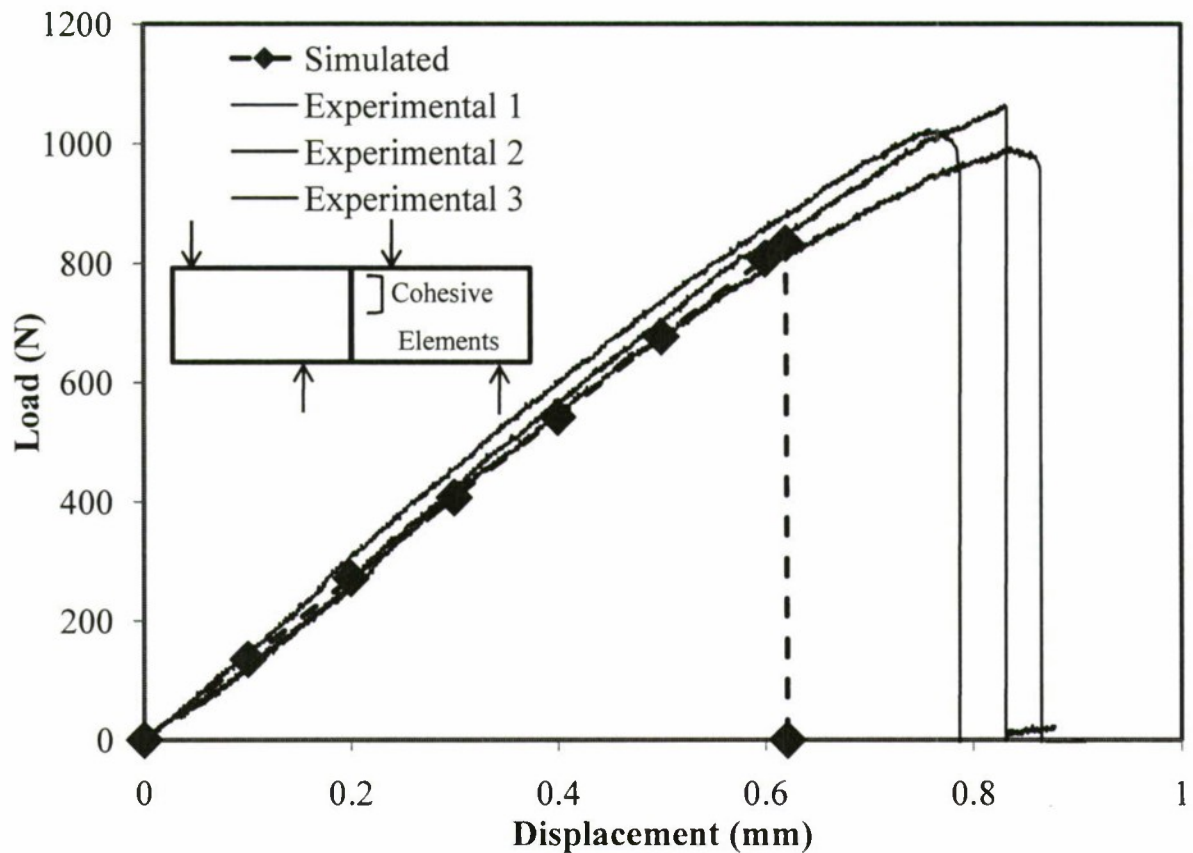


**Fig. 13** Simulated and experimental load-displacement graphs for strongly bonded polycarbonate systems.

The load-displacement curves obtained from the proposed new approach show a sudden and clear drop as seen in Figs. 13 and 14. The crack initiation and the final failure loads coincide. This is very accurate in finding the crack initiation load and is a major advantage of our new approach. For other methods involving beam bending, the crack initiation load is not obvious as the beam compliance change involving short crack propagation is small (Xu and Kou, 1994). This is a possible reason for overestimation of the mode II fracture toughness of composite

materials. Future work involves extending this approach to measure the fracture toughness of unidirectional composites.

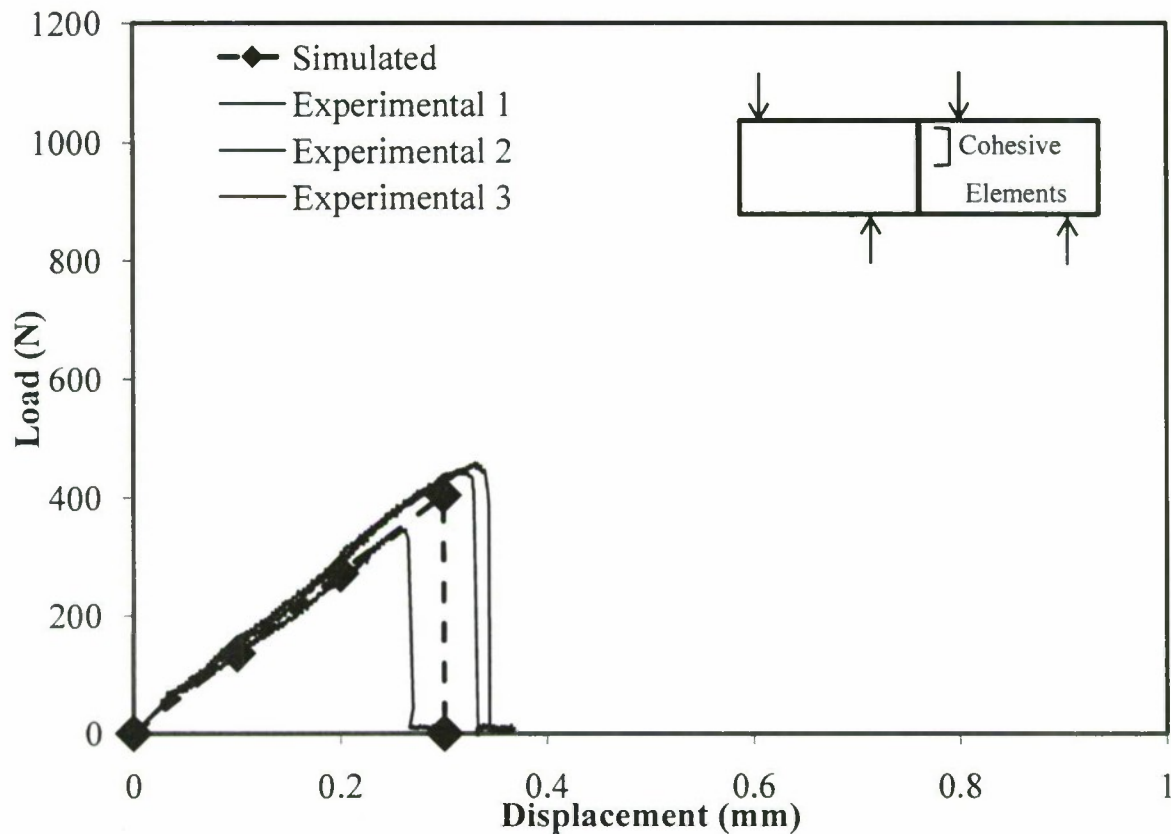


**Fig. 14** Simulated and experimental load-displacement graphs for weakly bonded polycarbonate systems.

## 5. Conclusions

The mode II fracture toughness of materials with preferred interfaces can be measured by using the proposed short-beam shear approach. The amount of friction between the cracked surfaces behind the crack tip is negligible, and hence an intrinsic value of the pure mode-II fracture toughness is obtained. Another feature of our new approach is the accurate measurement of crack initiation load which is not available in previous techniques. The current method is justified by

the use of numerical techniques (finite element analysis and cohesive element analysis), and comparison with experimental data. This method can also be extended to unidirectional composite materials.

### **Acknowledgements**

The authors acknowledge the support from the Office of Naval Research and the National Science Foundation.

## References

1. Anderson TL (2004) Fracture mechanics: Fundamentals and applications, 3<sup>rd</sup> Edn. CRC Press.
2. Bansal A, Kumosa M (1998) Analysis of double edge-cracker losipescu specimens under biaxial loads, *Engineering Fracture Mechanics*, 59(1), 89-100.
3. Bhattacharjee D, Knott JF (1995) Effect of mixed mode I and II loading on the fracture surface of polymethyl methacrylate (PMMA), *International Journal of Fracture*, 72, 359-381.
4. Bing Q, Sun CT (2007) Effect of compressive transverse normal stress on mode II fracture toughness in polymeric composites, *International Journal of Fracture*, 145, 89-97.
5. Camacho GT, Ortiz M (1996) Computational modeling of impact damage in brittle materials, *International Journal of Solids and Structures*, 33, 2899-2938.
6. Coker D, Rosakis AJ (2001) Experimental observations of intersonic crack growth in asymmetrically loaded unidirectional composite plates, *Philosophical Magazine A*, 81(3), 571-595.
7. Daniel IM, Ishai O (2005) Engineering mechanics of composite materials, 2<sup>nd</sup> edn. Oxford University Press, New York.
8. Erdogan F, Sih GC (1963) On the crack extension in plates under plane loading and plane shear, *Journal of Basic Engineering*, 85, 519-527
9. Hutchinson J, Suo Z, (1992) Mixed-mode cracking in layered materials, *Advances in Applied Mechanics* 29, 63-191.
10. Krishnan A, Xu LR (2009) Systematic evaluation of bonding strengths and fracture toughnesses of adhesive joints, *Submitted to Journal of adhesion*.
11. Krishnan A, Xu LR (2010) Effect of the interfacial stress distribution on the material interfacial strength measurement, *Experimental Mechanics*, 50, 283-288.
12. Li XF, Xu LR (2007) T-Stresses across static crack kinking, *ASME Journal of Applied Mechanics*, 74, 181-190.
13. O'Dowd NP, Shih CF, Stout MG (1992) Test geometries for measuring interfacial fracture toughness, *International Journal of Solids and Structures*, 29(5), 571-589.
14. Rosakis AJ, Ravi-Chandar K (1986) On crack-tip stress state: An experimental evaluation of three-dimensional effects, *International Journal of Solids and Structures*, 22, 121-134.
15. Ruiz G, Pandolfi A, Ortiz M (2001) Three-dimensional cohesive modeling of dynamic mixed-mode fracture, *International Journal Numerical Methods in Engineering*, 52, 97-120.
16. Qian H, Sun CT (2008) Effect of bondline thickness on mode I fracture in adhesive joints, *Proceedings of the 2008 AIAA SDM Conference*, Schaumburg, IL.
17. Sih GC, Paris PC, Irwin GR (1965) On cracks in rectilinearly anisotropic bodies, *International Journal of Fracture*, 1, 189-203.
18. Sun CT (2008) Why LEFM is not applicable for bonded joints, 23<sup>rd</sup> Technical Conference, American Society for Composites, Memphis TN.

19. Sun CT, Qian H (2009) Brittle fracture beyond the stress intensity factor, *Journal of mechanics of materials and structures*, 4(4), 743-753.
20. Suresh S, Shih CF, Morrone A, O'Dowd NP (1990) Mixed mode fracture toughness of ceramic materials, *Journal of American Ceramic Society*, 73(5), 1257-67.
21. Walrath DE, Adams DF (1983) The Iosipescu shear test as applied to composite materials, *Experimental Mechanics*, 23(1), 105-110.
22. Williams JG, Ewing PD (1972) Fracture under complex stress-The angled crack problem, *International Journal of Fracture Mechanics*, 8, 441-446
23. Xu S, Reinhardt HW, Gappoev M (1996) Mode II fracture testing method for highly orthotropic materials like wood, *International Journal of Fracture*, 75, 85-214.
24. Xu, L and C.H. Kou (1994) Effect of Interfacial Interleaf to the Interlaminar Fracture and Intralaminar Fracture in A New Bismaleimide MatrixHistry Composites System, *Journal of Reinforced Plastics and Composites*, 13, 509-540.
25. Xu LR, Huang YY, Rosakis AJ (2003) Dynamic crack deflection and penetration at interfaces in homogenous materials: experimental studies and model predictions, *Journal of Mechanics and Physics in Solids*, 51, 461-486.
26. Xu LR, Rosakis AJ (2003) An experimental study on dynamic failure events in homogenous layered materials using dynamic photoelasticity and high-speed photography, *Optics and Laser in Engineering*, 40, 263-288.
27. Xu LR, Sengupta S, Kuai H (2004a) Dissimilar material joints with and without free-edge stress singularities: Part I. A biologically inspired design, *Experimental Mechanics*, 44(6) 608-615.
28. Xu LR, Sengupta S, Kuai H (2004b) An experimental and numerical investigation of adhesive bonding strengths of polymer materials, *International Journal of Adhesion and Adhesives*, 24, 455-460.
29. Yoshihara H, Satoh A (2009) Shear and crack tip deformation correction for the double cantilever beam and three-point end-notched flexure specimens for mode I and II fracture toughness measurement of wood, *Engineering Fracture Mechanics*, 76(3), 335-346.

## List of Figures

**Fig. 1** Schematic diagram of the short-beam shear test with equivalent applied loading at distances A and B

**Fig. 2** Finite element analysis results showing very small variations of A and B with a wide range of elastic moduli under an applied displacement of 0.2 mm

**Fig. 3** Finite element analysis results showing very small variations of A and B with a wide range of applied displacements for polymeric specimen with an elastic modulus of 2.4 GPa

**Fig. 4** Schematic diagram of a short-beam shear specimen for unidirectional composites materials

**Fig. 5** Finite element analysis results showing very small variation in A and B with elastic modulus ratio for different types of orthotropic composite materials.

**Fig. 6** Schematic diagram showing the crack kinking

**Fig. 7** Picture of a typical strongly bonded polycarbonate specimen showing crack kinking from the interface

**Fig. 8** Snapshot of deformed mesh (near the crack tip) at failure load. This mesh is used for modeling short-beam shear specimen

**Fig. 9** Variation of shear stress and normal stress along the interface for polycarbonate same-material bonding at a failure load of 1000 N.

**Fig. 10** Variation of shear stresses along the interface for polycarbonate same-material bonding with increase in applied loading. There is negligible friction observed beyond the crack tip.

**Fig. 11** Variation of dimensionless stress intensity factor  $F_{II}$  with relative crack depth for different types of composites.

**Fig. 12** Traction-Separation law used for strongly bonded Polycarbonate

**Fig. 13** Simulated and experimental load-displacement graphs for strongly bonded polycarbonate systems.

**Fig. 14** Simulated and experimental load-displacement graphs for weakly bonded polycarbonate systems.

## List of Tables

**Table. 1** Experimental results for same-material specimens

**Table 2.** Variation of mode I and mode II stress intensity factors  $K_I$  and  $K_{II}$  with applied load for same-material polycarbonate specimen

**Table 3.** Properties for three typical composites (Daniel and Ishai, 2005)

**Table 4.** Variation of  $F_{II}$  with  $a/W$  for different types of composites.  $K_I$  and  $K_{II}$  are expressed in  $\text{MPa m}^{1/2}$  ( $A=15.49 \text{ mm}$ ,  $B=32.44 \text{ mm}$ )

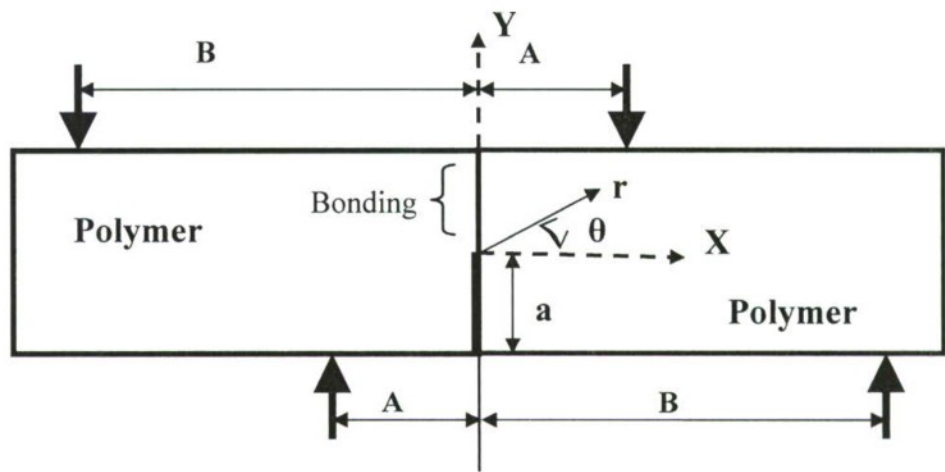


**Fig. 1** Schematic diagram of the short-beam shear test with equivalent applied loading at distances A and B

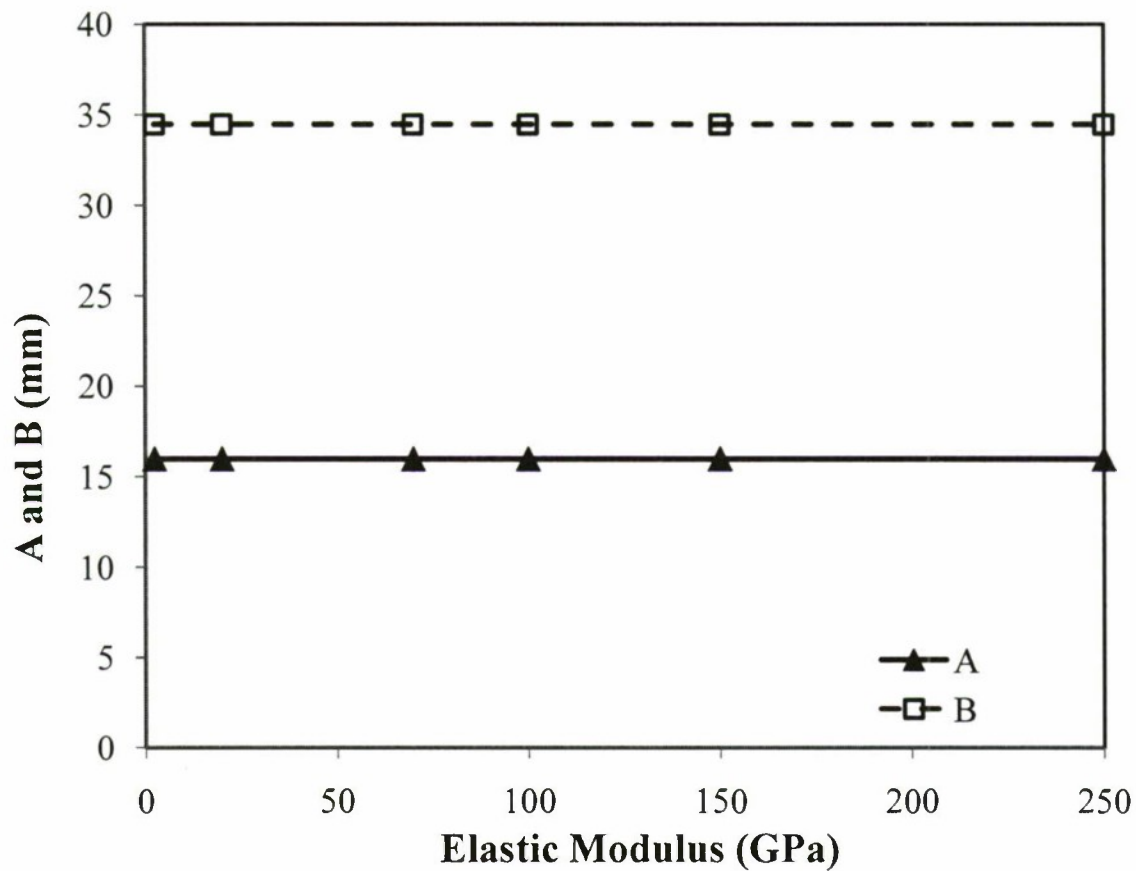


**Fig. 2** Finite element analysis results showing very small variations of  $A$  and  $B$  with a wide range of elastic moduli under an applied displacement of 0.2 mm

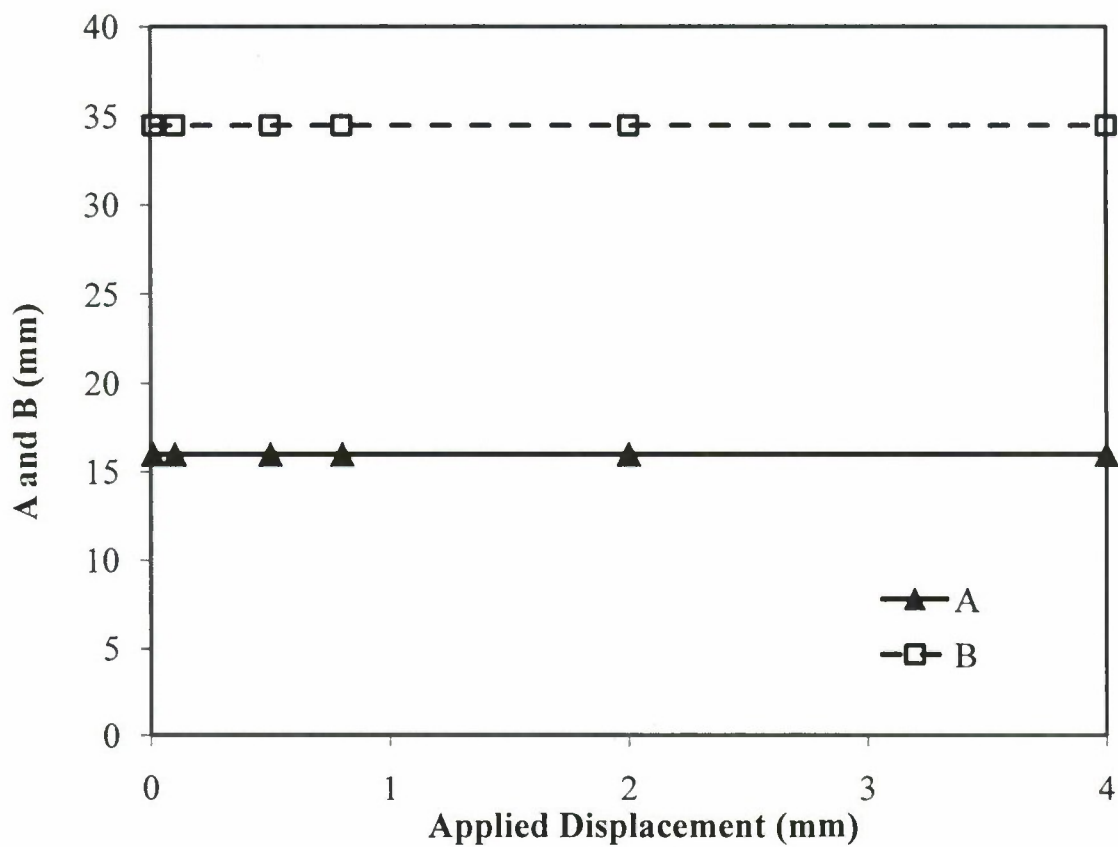


**Fig. 3** Finite element analysis results showing very small variations of  $A$  and  $B$  with a wide range of applied displacements for polymeric specimen with an elastic modulus of 2.4 GPa

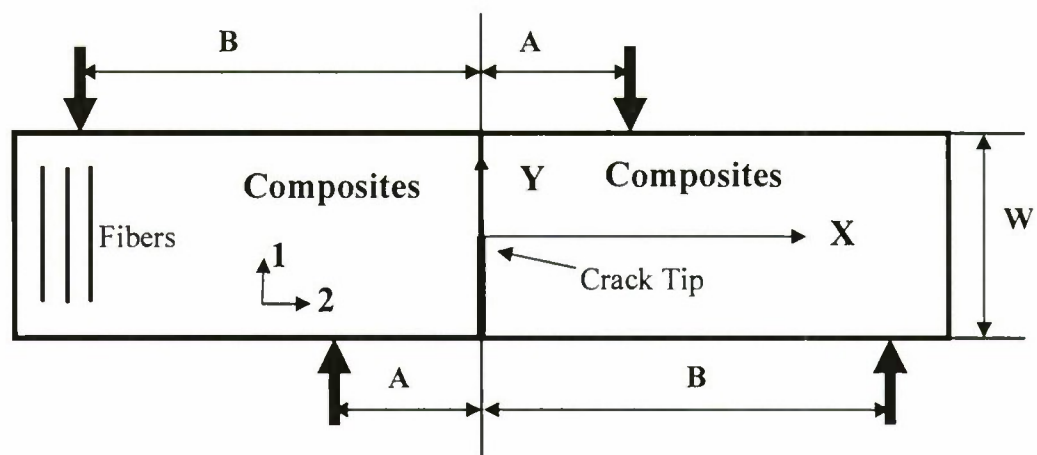


**Fig. 4** Schematic diagram of a short-beam shear specimen for unidirectional composites materials

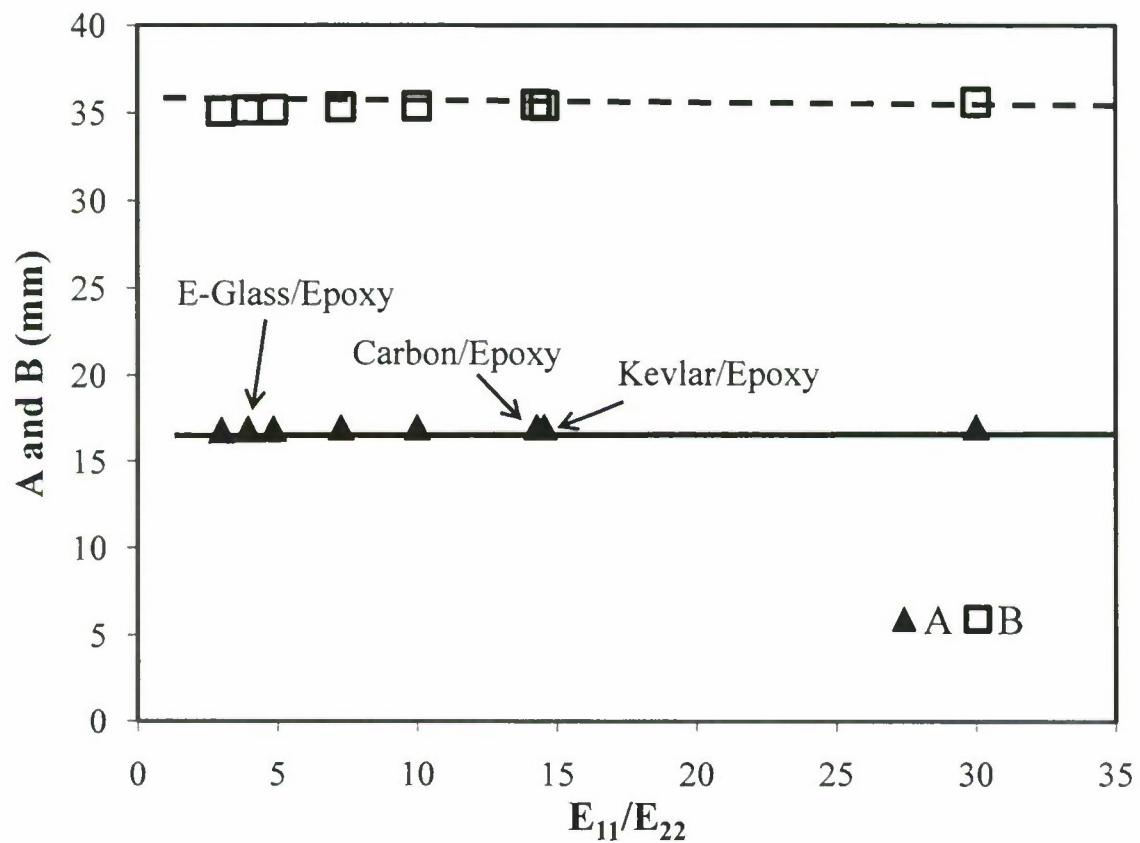


**Fig. 5** Finite element analysis results showing very small variation in  $A$  and  $B$  with elastic modulus ratio for different types of orthotropic composite materials.

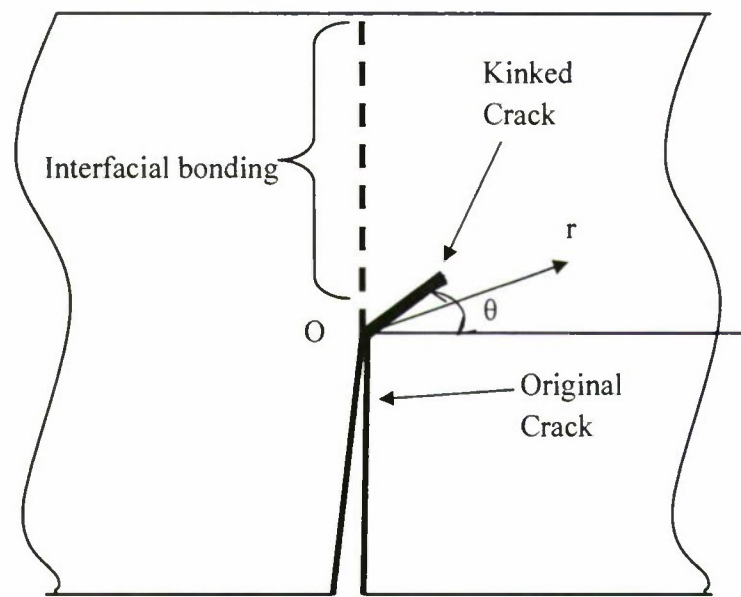


**Fig. 6** Schematic diagram showing the crack kinking

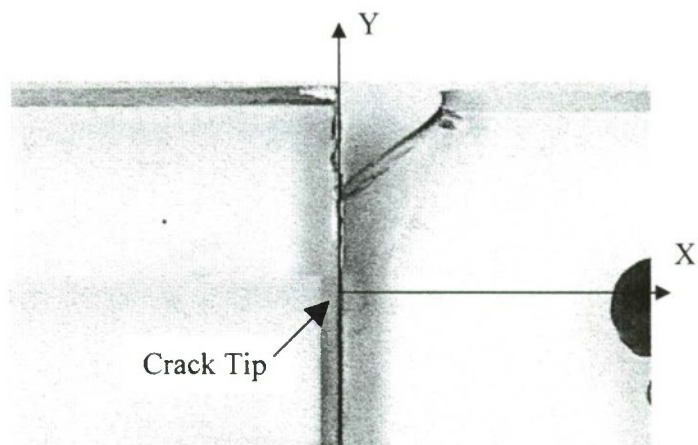


**Fig. 7** Picture of a typical strongly bonded polycarbonate specimen showing crack kinking from the interface

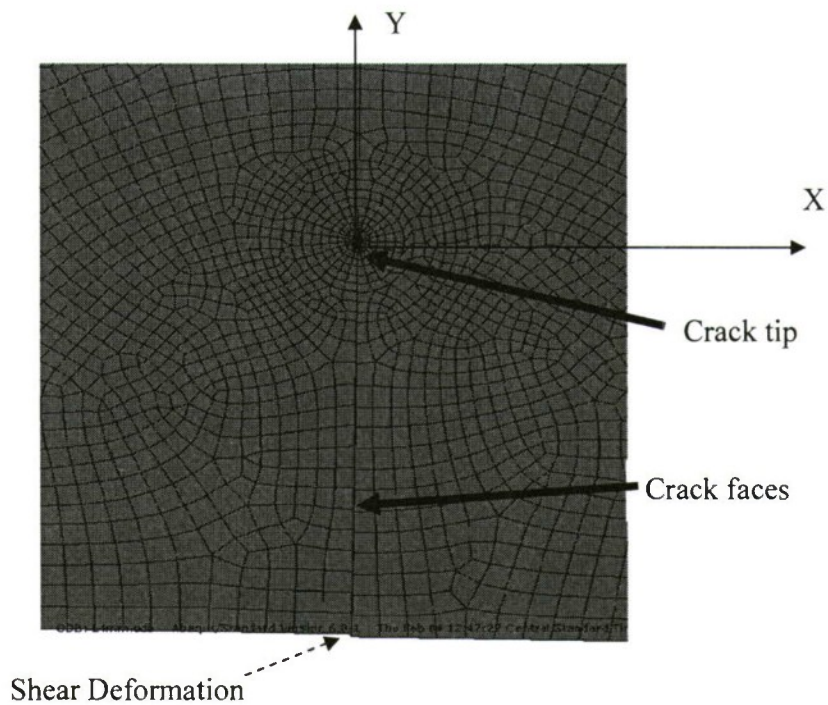


**Fig.8** Snapshot of deformed mesh (near the crack tip) at failure load. This mesh is used for modeling short-beam shear specimen

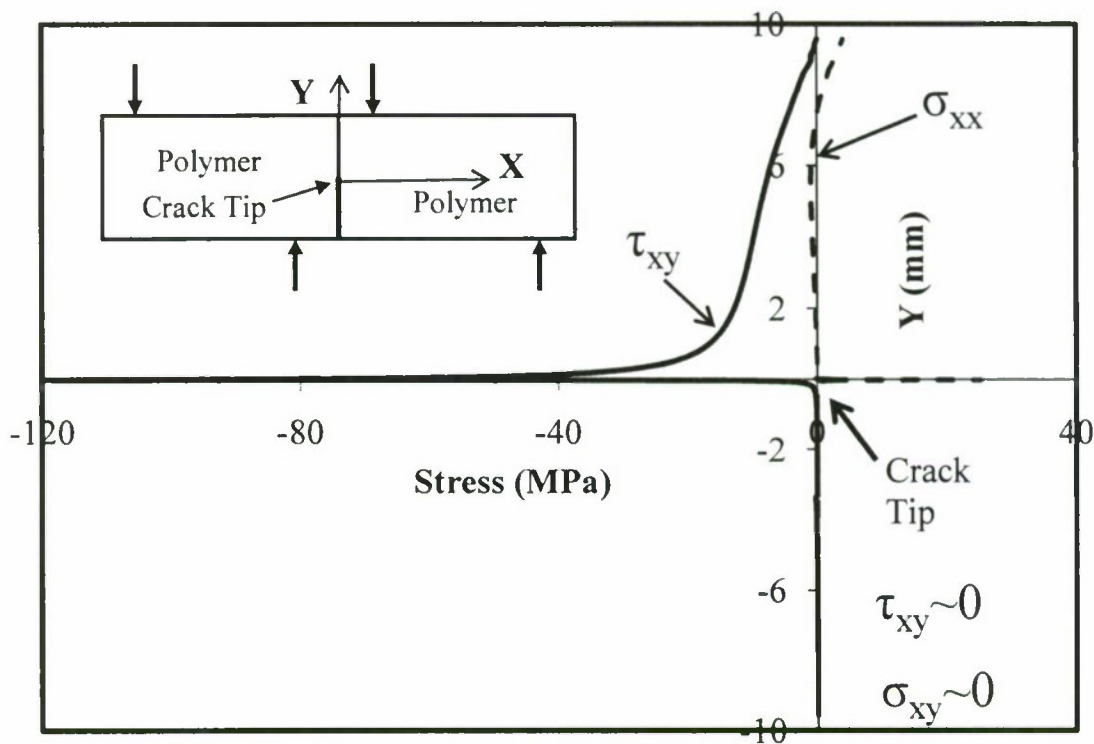


**Fig.9** Variation of shear stress and normal stress along the interface for polycarbonate same-material bonding at a failure load of 1000 N.

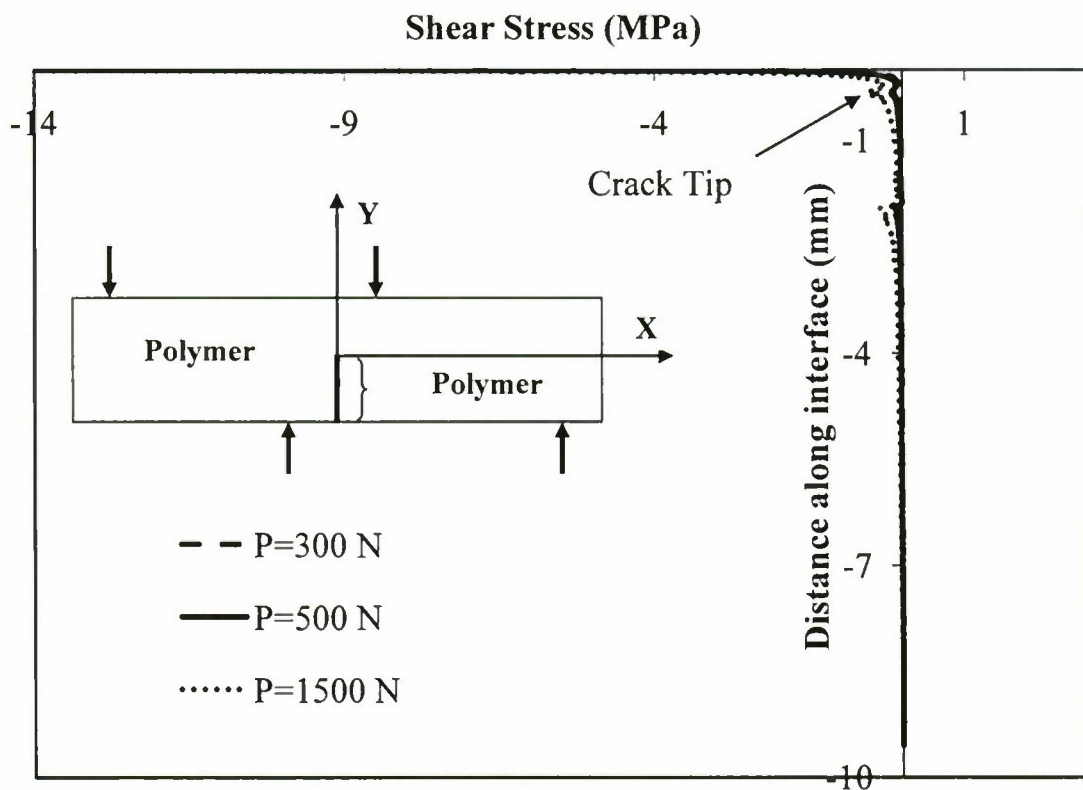


**Fig. 10** Variation of shear stresses along the interface for polycarbonate same-material bonding with increase in applied loading. There is negligible friction observed beyond the crack tip.

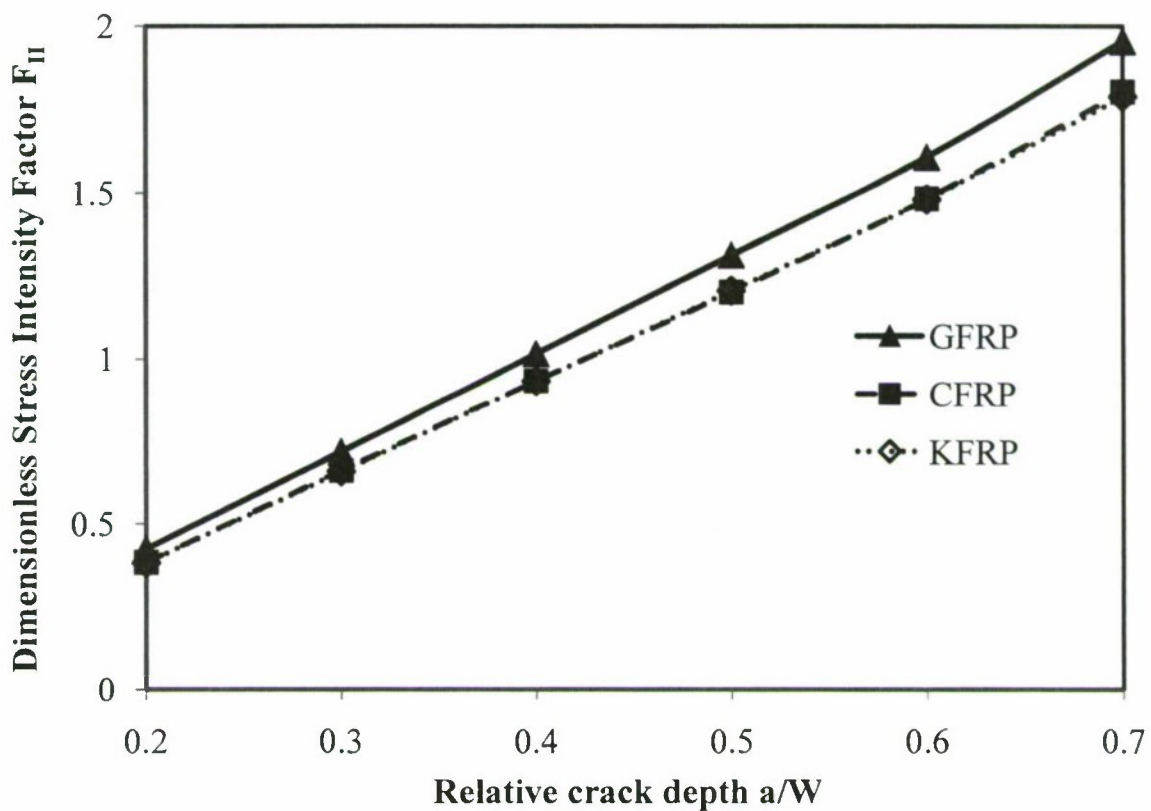


**Fig. 11** Variation of dimensionless stress intensity factor  $F_{II}$  with relative crack depth for different types of composites.

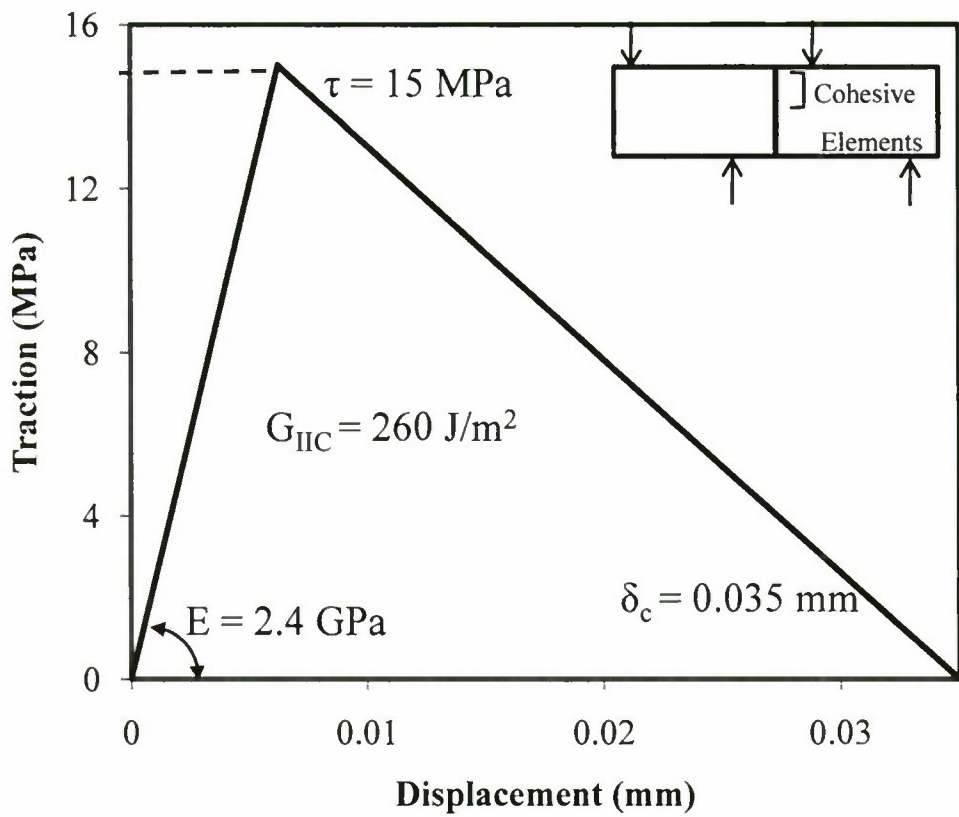
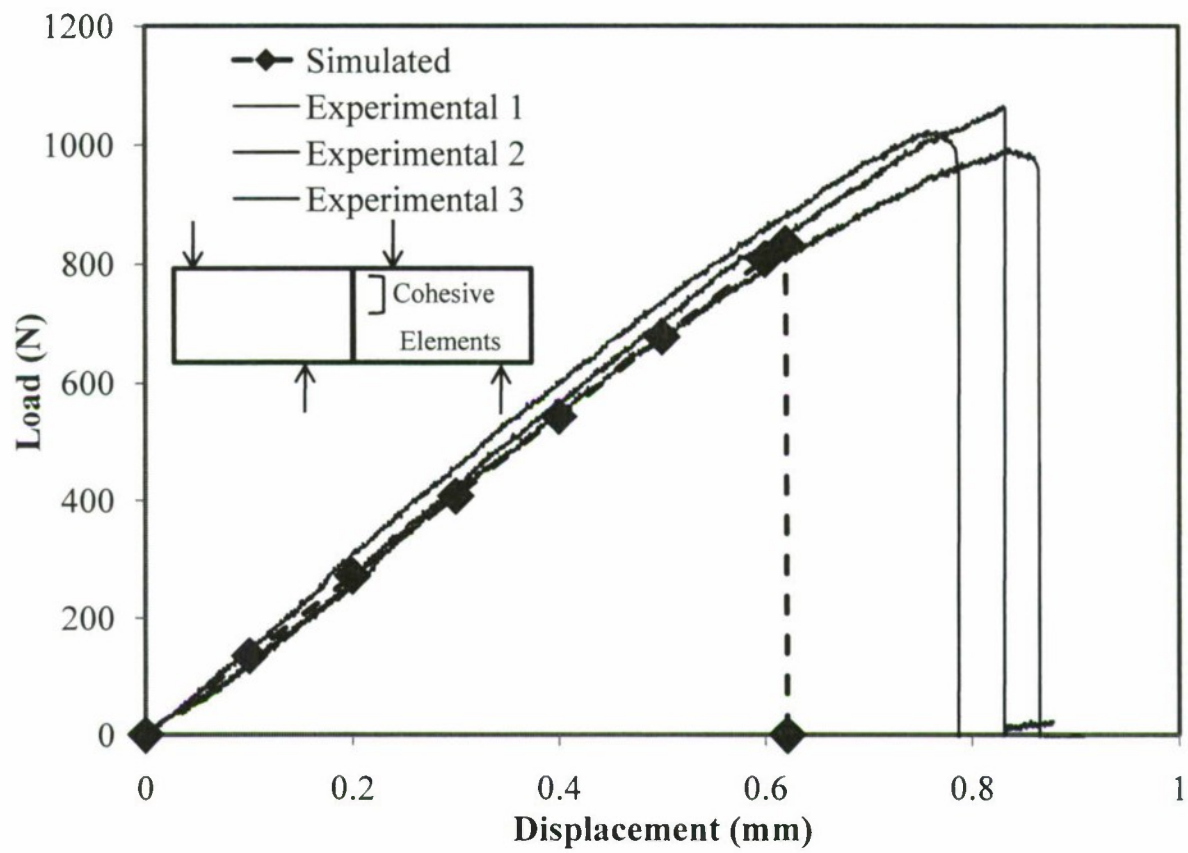
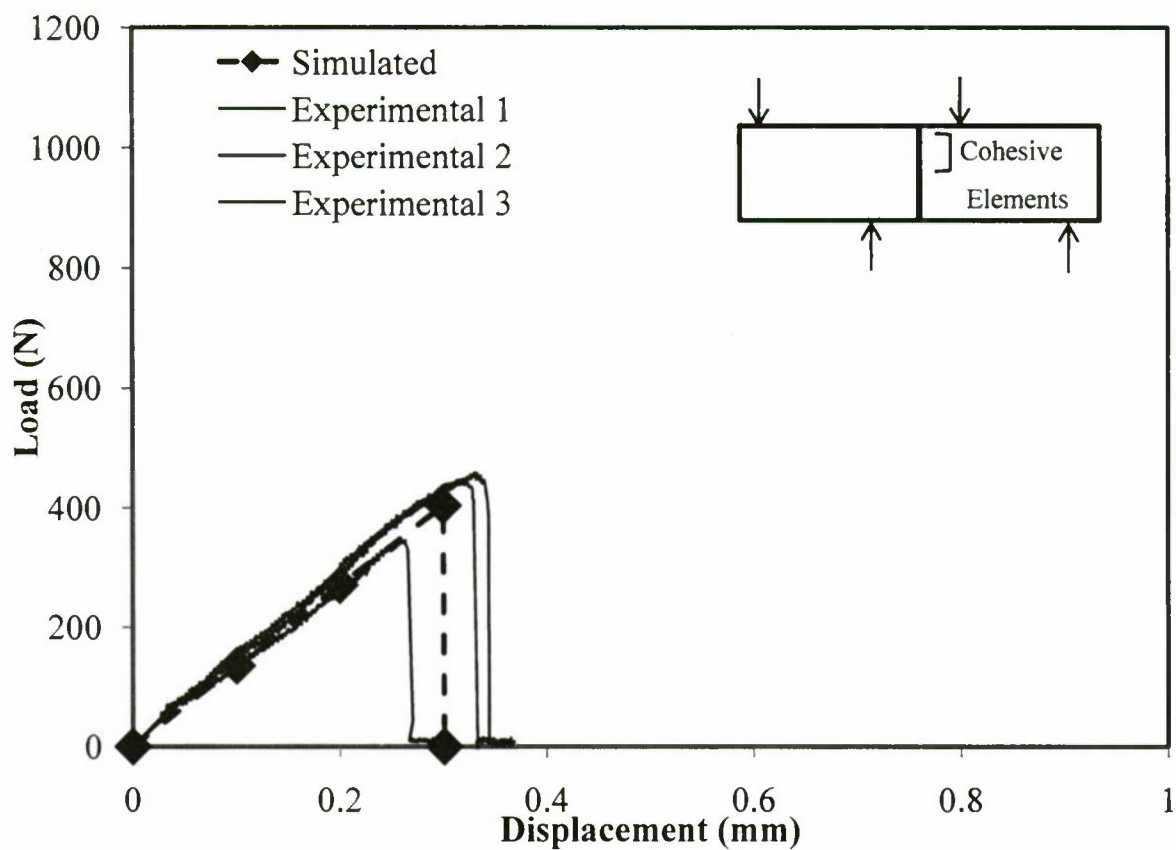


Fig. 12 Traction-Separation law used for strongly bonded Polycarbonate



**Fig. 13** Simulated and experimental load-displacement graphs for strongly bonded polycarbonate systems.



**Fig. 14** Simulated and experimental load-displacement graphs for weakly bonded polycarbonate systems.

**Table. 1** Experimental results for same-material specimens

Bonded materials	Bonding	Crack initiation load (N)	$K_{IIC}$ (MPa $m^{0.5}$ )	$G_{IIC}$ (J/m <sup>2</sup> )
Polycarbonate	Weak	$417 \pm 49$	$0.33 \pm 0.04$	45.8
Polycarbonate	Strong	$1002 \pm 57$	$0.76 \pm 0.05$	260.8
PMMA	Weak	$451 \pm 100$	$0.35 \pm 0.08$	34.6
PMMA	Strong	$975 \pm 81$	$\geq 0.77 \pm 0.06$	$\geq 155.6$

**Table 2.** Variation of mode I and mode II stress intensity factors  $K_I$  and  $K_{II}$  with applied load for same-material polycarbonate specimen

Load (N)	Finite Element Analysis		Formula	
	$K_I$ (MPa $m^{0.5}$ )	$K_{II}$ (MPa $m^{0.5}$ )	$K_I$ (MPa $m^{0.5}$ )	$K_{II}$ (MPa $m^{0.5}$ )
135	0.0019	0.1067	0	0.1060
405	0.0057	0.3199	0	0.3179
675	0.0097	0.5333	0	0.5299
1350	0.019	1.067	0	1.0598

**Table 3.** Properties for three typical composites (Daniel and Ishai, 2005)

Materials	Fiber volume percent (%)	$E_{11}$ (GPa)	$E_{22}$ (GPa)	$G_{12}$ (GPa)	$G_{23}$ (GPa)	$v_{12}$	$v_{23}$
Carbon/Epoxy	63	147	10.3	7	3.7	0.27	0.54
E-Glass/Epoxy	55	41	10.4	4.3	3.5	0.28	0.5
Kevlar/Epoxy	60	80	5.5	2.2	1.8	0.34	0.4

**Table 4.** Variation of  $F_{II}$  with  $a/W$  for different types of composites.  $K_I$  and  $K_{II}$  are expressed in MPa m<sup>1/2</sup> ( $A=15.49$  mm,  $B=32.44$  mm)

CFRP

<b>a/W</b>	<b>Load (N)</b>	<b><math>K_I</math>(MPa m<sup>1/2</sup>)</b>	<b><math>K_{II}</math>(MPa m<sup>1/2</sup>)</b>	<b><math>K_{II}/K_I</math></b>	<b><math>F_{II}</math></b>
0.2	1009	0.0124	1.2412	0.0099	0.3836
0.3	1008	0.0090	2.1345	0.0042	0.6603
0.4	1004	0.0026	3.0042	0.0009	0.933
0.5	1001	0.0006	3.8580	0.0001	1.2018
0.6	991	0.0083	4.7118	0.0018	1.4825
0.7	979	0.0146	5.6605	0.0026	1.8029

GFRP

<b>a/W</b>	<b>Load (N)</b>	<b><math>K_I</math>(MPa m<sup>1/2</sup>)</b>	<b><math>K_{II}</math>(MPa m<sup>1/2</sup>)</b>	<b><math>K_{II}/K_I</math></b>	<b><math>F_{II}</math></b>
0.2	709	0.0405	0.9645	0.0419	0.4242
0.3	708	0.0281	1.6286	0.0173	0.7173
0.4	704	0.0072	2.2927	0.0031	1.0155
0.5	698	0.0095	2.9410	0.0032	1.3138
0.6	687	0.0263	3.5418	0.0075	1.6075
0.7	671	0.0361	4.2058	0.0086	1.9544

KFRP

<b>a/W</b>	<b>Load (N)</b>	<b><math>K_I</math>(MPa m<sup>1/2</sup>)</b>	<b><math>K_{II}</math>(MPa m<sup>1/2</sup>)</b>	<b><math>K_{II}/K_I</math></b>	<b><math>F_{II}</math></b>
0.2	420	0.0058	0.5139	0.0113	0.3815
0.3	420	0.0039	0.8854	0.0044	0.6573
0.4	418	0.0006	1.2491	0.0005	0.9318
0.5	417	0.0004	1.6128	0.0003	1.2059
0.6	413	0.0043	1.9606	0.0022	1.4802
0.7	408	0.0063	2.3401	0.0027	1.7884

Submitted to *Journal of Adhesion* (2009)

## Systematic evaluation of bonding strengths and fracture toughnesses of adhesive joints

Arun Krishnan and L. Roy Xu\*

Department of Civil and Environmental Engineering

and Materials Science Program

Vanderbilt University

Nashville, TN 37235, USA

### Abstract

A systematic experimental investigation to determine the shear, tensile and fracture properties of adhesive joints with bonded same-materials (polymer-polymer) and bi-materials (metal-polymer) is reported. Full-field optical techniques including photoelasticity and Coherent Gradient Sensing (CGS) are employed to record the stress development and failure in these adhesive joints. Five types of strong and weak adhesives are used in conjunction with five different types of materials (aluminum, steel, PMMA, polycarbonate and Homalite) to produce a variety of bonded material systems. Weldon-10 and Polyester bonding consistently show higher tensile and shear bonding strengths. However, bi-material fracture toughnesses tend to show a lesser difference between the weak and strong adhesive bonding. Bi-material systems in shear and fracture report lower properties than the same-material systems due to a higher property mismatch in the former. The resulting complete experimental data are expected to be immensely helpful to computational mechanists in simulating failure mechanics of adhesive joints.

---

\* Corresponding author, E-mail: [luoyu.r.xu@gmail.com](mailto:luoyu.r.xu@gmail.com). Tel: 615-343-4891

*Keywords:* Adhesive bonding, Bi-materials, Fracture toughness, Shear strength, Tensile strength

## 1. INTRODUCTION

A dissimilar-material joint is a special type of material boundary at which two or more different materials are joined together (e.g., aluminum with polycarbonate) by means of an adhesive. This type of an interface poses challenging problems in characterizing its associated mechanical properties, especially if the constituent materials have a significantly high property mismatch. Recently, dissimilar-material joints have found several engineering applications. Examples include adhesively bonded composite and metal joints in advanced aircraft and ship structures, fiber/matrix interfaces in composite materials, thin film/substrate structure in micro-electromechanical systems (MEMS) among others. However, a variety of studies have indicated that failure often occurs along the interface between two different materials with high property mismatch (e.g., free-edge delamination in composite laminates, debonding between thin films/substrates), and that improving the interfacial mechanical properties (especially reducing the interfacial stress level) can modify overall material/structural behavior (Hutchinson and Suo, 1992; Gupta et al., 1994; Lara-Curzio et al., 1995; Needleman and Rosakis, 1999; Martin et al., 2001; Xu and Rosakis, 2002; Wang, 2007). However, the interfacial strength measurement of dissimilar-material joints remains a challenge due to the stress singularity problem (Reedy and Guess, 1993; Tandon et al., 1999; Akisanya and Fleck, 1997), i.e., the theoretical interfacial stress will be infinite at the free-edges. On the other hand, modern numerical tools like the cohesive element method have an urgent need for interfacial strengths and fracture toughnesses as important input data. Hence, it becomes necessary to develop reliable quantitative measurements in order to characterize mechanical properties of dissimilar-material joints.

The primary objective of this paper is to measure complete mechanical properties for polymer and metal combinations with different adhesive bonding. The mechanics of bi-materials is complicated; therefore same-material adhesive joints without high property mismatch will be used to highlight certain simple mechanics aspects involved in the problem. Additionally, we utilize new joint designs to remove the free-edge stress singularity, thereby providing reasonable tensile bonding strength measurements of dissimilar-material joints. We also present resulting fringe patterns from the Coherent Gradient Sensing (CGS) and photoelasticity experiments (Singh et al., 1997), which aid in validating our finite element model. For the sake of completeness and direct comparison, we include some mechanical property data from our previous measurements of dissimilar-material joint systems.

## **2. EXPERIMENTAL TECHNIQUE AND PROCEDURES**

### *2.1 Jointed material combinations with strong and weak adhesive bonding*

This section describes the preparation of specimens and related experimental procedures. Specimens were made of five different types of materials including aluminum, steel, polycarbonate, PMMA, and Homalite. While the same-material joint specimens were made of PMMA, Homalite, polycarbonate and aluminum, bi-material specimen pairs included PMMA/aluminum, PMMA/steel, polycarbonate/aluminum, and Homalite/steel. Two major types of adhesives were used as bonding agents in most of the specimens. Loctite-384 (Henkel Corp., Rocky Hill, CT), a type of tough Acrylic, was used to provide weak bonding. Weldon-10 (IPS Corp., Gardena, CA), a mixture of Acrylic Resin and Methyl Methacrylate Monomer, was used to provide strong bonding. Polyester, Loctite 5083 and Loctite 330 were also used as adhesives

for interfacial bonding. All these adhesives were specifically chosen because their Young's modulus when cured is close to that of PMMA, polycarbonate and Homalite (around 2-4GPa). This ensures that the mechanics of metal/adhesive/polymer joints remains a bi-material mechanics problem and does not become a complicated case involving three different kinds of materials. Every specimen was bonded together from separate halves to enable an interfacial failure and all of the individual bonding surfaces were sandblasted prior to bonding in order to improve the bonding quality. The bonding itself was enabled by a special fixture to guarantee dimensionality. The specimens were cured for a period of 24 hours in order to achieve the bonding strength.

**Fig.1**

## *2.2 Two optical techniques and experimental procedures*

In order to record in-situ fringe patterns developed during the loading process, a mechanical-optical system as illustrated in Fig. 1 was used. This setup included an optical system, a mechanical testing system and an imaging system. The mechanical testing system consisted of a MTS 810 test machine and a fixture. The optical system was utilized to capture the in-situ fringe pattern development during tests. A laser beam was transmitted through the transparent polymer specimens, and the resulting fringe patterns were recorded by a digital camera. The isochromatic fringe patterns observed in polycarbonate and Homalite specimens are the contours of the maximum in-plane shear stress,

$$\tau_{\max} = \frac{(\sigma_1 - \sigma_2)}{2} = \frac{Nf_\sigma}{2h} \quad (1)$$

where  $\sigma_1$  and  $\sigma_2$  are in-plane principal stresses, N is the fringe order,  $f_\sigma$  is the stress-fringe constant and h is the specimen thickness (Kobayashi, 1987). The optical system included a He-Ne laser source (17 mW), a laser collimator, and a reflection mirror. The collimator was used to provide a large and collimated laser beam of approximately 50 mm diameter. The purpose of the mirror was to adjust the laser beam to a desired position for a specific experiment. The imaging system included a digital camera used to capture fringe development and a density filter in front of the camera to reduce the laser intensity of the laser beam entering the camera directly. A convex lens with a focal length 150 mm was added to the system to record the whole field of view. An important issue in obtaining good-quality images is to focus the digital camera at infinity, and to ensure the distance between the convex lens and the specimen to be slightly larger than the focal length of the convex lens. Another technique used in this study, Coherent Gradient Sensing technique developed by Tippur et al. (1991), was used to obtain fringes of gradients of  $\sigma_1 + \sigma_2$  in PMMA specimens as seen in Fig.2.

**Fig.2**

### 3. TENSILE STRENGTHS OF SAME AND DISSIMILAR-MATERIAL JOINTS

#### 3.1 Free-edge stress singularity and specimen designs to remove the stress singularity

For some specific bi-material corners or edges, several researchers including Williams (1952), Bogy (1971), have shown that stress singularities exist. The asymptotic stress field of a bi-material corner can be expressed by

$$\sigma_y(r, \theta) = \sum_{k=0}^N r^{-\lambda_k} K_k f_{ijk}(\theta) \quad (i, j = 1, 2, 3) \quad (2)$$

where  $f_{ijk}(\theta)$  is an angular function and  $K_k$  is also known as the “stress intensity factor”. The fracture mechanics terminology “stress intensity factor” is used in interfacial mechanics to characterize a similar stress singularity problem. It should be noticed that for an interfacial fracture problem (assuming initial debonding), the stress singularity at a crack tip is intrinsic and cannot be removed. However, the stress singularity in interfacial strength investigation such as bi-material joints (assuming perfect bonding) can be removed through appropriate designs. The stress singularity order  $\lambda$  may be real or complex, and the singularity order is -0.5 for a crack in the same material based on the Linear Elastic Fracture Mechanics (LEFM). Hence the theoretical stress values will become infinite as  $r$  (defined in Fig. 2(b)) approaches zero, if  $\lambda$  has a positive real part. This leads to a problem referred to as the “free-edge stress singularity problem”. It is the presence of this stress singularity that leads to erroneous results in current interfacial strength measurements besides being responsible for free-edge debonding or delamination in dissimilar material joints. But, if  $\lambda$  has a non-positive real part, then, the stress singularity disappears.

Bogy (1971) found that the stress singularity was purely determined by the material property mismatch and two joint angles of the bi-material corner  $\theta_1, \theta_2$  (defined in Fig. 2(b)). Generally, the material property mismatch can be expressed in terms of the Dundurs' parameters  $\alpha$  and  $\beta$ - two non-dimensional parameters computed from elastic constants of two bonded materials (Hutchinson and Suo, 1992):

$$\alpha = \frac{\mu_1 m_2 - \mu_2 m_1}{\mu_1 m_2 + \mu_2 m_1} \quad \beta = \frac{\mu_1(m_2 - 2) - \mu_2(m_1 - 2)}{\mu_1 m_2 + \mu_2 m_1} \quad (3)$$

where  $\mu_1$  is the shear modulus of material 1,  $\mu_2$  is the shear modulus of material 2,  $m = 4(1-\nu)$  for plane strain,  $\nu$  is the Poisson's ratio and  $m = 4/(1+\nu)$  for generalized plane

stress. The stress singularity order is related to material and geometric parameters, and is determined by a characteristic equation of coefficients A ( $\theta_1, \theta_2, p$ ) through F ( $\theta_1, \theta_2, p$ ):

$$f(\theta_1, \theta_2, \alpha, \beta, p) = A\beta^2 + 2B\alpha\beta + C\alpha^2 + 2D\beta + 2E\alpha + F = 0 \quad (4)$$

where  $p=1-\lambda$  and A, B, C, D, E and F are as defined by Bogy (1971). Therefore, our basic idea is to vary these four independent parameters ( $\theta_1, \theta_2, \alpha, \beta$ ) in order to obtain a negative real part of the stress singularity order  $\lambda$ . Xu et al., (2004a) chose an interfacial design with two joint angles:  $\theta_1 = 65^\circ$  and  $\theta_2 = 45^\circ$  and assumed material 1 to be a typical hard material and material 2 to be a soft material. Then, there will be no stress singularity for a wide range of current engineering materials (small deviation of this pair of joint angles will not change the result). This result is applicable to the entire possible range of the two Dundur's parameters. For this specific pair of joint angles, the stress singularity is limited to a very small zone near  $\alpha \approx 1$ . These extreme material joint combinations are quite rare in engineering applications since they represent extremely high mismatch in Young's moduli.

Planar and axisymmetric bonded specimens (with the same bonding area) were used for testing specimens in tension. The planar tension specimens are 254 mm long (individual halves are 127 mm long), 38 mm wide and 6 mm thick. These specimens were used to make same and bi-material joints. The length and thickness of all the specimens were chosen such that the gripping pressure from the MTS system did not cause any specimen damage. The two types of planar tension specimens with straight-edges and convex edges are illustrated in Figure 3(a), (b), and the two types of axisymmetric specimens with straight edges and convex edges are shown in Figure 3(c), (d). The free-edge stress singularity was completely removed in axisymmetric convex joint specimens (Wang and Xu, 2006).

**Fig.3**

### *3.2 Comparisons of tensile bonding strengths for different material systems and adhesives*

In each of the tables such as Table 1, the results for same-material joints are reported first followed by the bi-material data. The first column mentions the type of bonding and the joint materials. The second column presents the data as a mean strength, while the third column reports the difference between the weak and strong bonding of the same-material joints. In all the tables, Loctite adhesives are referred to by their corresponding numbers. For example, 384 would denote the weak bond produced by utilizing Loctite 384 adhesive. W10 refers to the strong adhesive Weldon-10. This convention is used in all the tables presented in this study.

**Table 1**

Material systems bonded with Weldon-10 show a higher tensile strength than the same-material systems bonded with Loctite 384 as seen in Table 1. A general trend observed in our tensile strength data is that PMMA material systems show a higher value of tensile strengths than polycarbonate systems. All of the specimens were observed to fail in sudden and brittle tension along the interface. To ensure repeatability, at least five specimens were tested in each case. In order to provide a complete data base of the same-material bonding of different polymer systems, some results from our previous conference paper (Xu et al., 2002) are presented in Table 1 along with latest data. Experimental data from our previous work is accumulated here along with currently measured data for the convenience of modeling and simulation work.

For the Homalite/adhesive/Homalite system, in addition to the strong and weak adhesives (Weldon-10 and Loctite 384), Polyester was also used in strong bonding. The tensile strength of

this bond was the highest as Polyester shares a similar chemical structure with Homalite. Loctite 330 is another strong adhesive similar to Weldon-10 and its tensile bonding strengths are quite high. Indeed, the weak adhesive Loctite 384 only provided slightly lower bonding strength than Loctite 330 or Weldon-10. The weakest adhesive used is Loctite 5083 since its tensile strength is only 20% of the bonding strength obtained by using the strong adhesive Weldon-10.

Table 1 shows a slight increase in the tensile bonding strengths of bi-materials for those material systems using Weldon-10 adhesives. Data related to bi-material bonding are from our previous measurements (Wang and Xu, 2006). Also, bonding strengths of the polycarbonate/aluminum system are just slightly lower than those of PMMA/aluminum system. However, for the Homalite/steel systems, the bonding strength using Loctite 384 is only 32% of the bonding strength of PMMA/aluminum system. This is probably due to the possibility that chemical bonding capability of Loctite 383 with steel/Homalite is not as good as that with aluminum/PMMA.

#### **4. SHEAR STRENGTHS OF SAME AND DISSIMILAR-MATERIAL JOINTS**

##### *4.1 Specimens and test approaches*

Shear bonding strength is a key material property for any adhesive joints of dissimilar materials. Previous researchers (Xu and Rosakis, 2002; Kitey and Tippur, 2008) have shown that shear failure is a dominant interfacial failure mode when layered materials with interfaces were subjected to out-of-plane dynamic loading. Thus, for dissimilar-material joints with interfaces, it becomes very necessary to measure the interfacial shear strength for quality control and failure prevention. In our experiments, we measured the interfacial shear strengths over a range of bonded material systems using two types of shear tests: Iosipescu and short-beam shear tests

which show different interfacial shear stress distributions. While the short-beam shear specimen shows a parabolic variation of shear stress across its interface, the Iosipescu specimen demonstrates a near constant shear stress variation as illustrated in Fig.4. The Iosipescu set-up was used to measure the shear strength of both types of specimens with the same specimen width. Iosipescu and short-beam shear specimens were 76.2 mm long (individual halves were 38.1 mm long), 19.1 mm wide and 5.4 mm thick. In addition, Iosipescu specimens have a notch with a depth of 3.8 mm at the center (Deng et al., 2009). Short-beam shear specimens were exclusively utilized to measure the shear strength of the bonded same-materials. Iosipescu shear specimens were used to measure the shear bonding strength for both same and bi-material joints.

**Fig.4**

Coherent Gradient Sensing experiments were carried out to obtain fringe patterns from bi-material specimens of PMMA/W10/aluminum. This is shown in Fig. 5 where an Iosipescu specimen is subjected to increasing shear load. Aluminum is not transparent and hence the fringes were seen only on the PMMA block. The set of four pictures shown in Fig. 5 illustrate the fringe development in the specimen from a small initial load until failure. A strong stress concentration is seen at the loading points and near the concave joint between aluminum and PMMA. Unlike tensile specimens, we were unable to design convex joints for bi-material shear specimens; hence the free-edge stress singularity still existed in bi-material shear specimens.

**Fig. 5**

In case of specimens with polycarbonate, photoelasticity experiments were carried out to obtain fringe patterns which are contours of maximum in-plane shear stress given by equation (1). These patterns as seen in Fig. 6, were obtained for short-beam shear specimens at loads of

12.5 % and 25 % of their final failure load. A finite element model of the specimen was built with ANSYS 11.0 to obtain the stress distributions in the bonded specimen. A two dimensional analysis was employed for bonded polycarbonate materials. The mesh comprised of only Plane 42 elements to meet the requirements of the plotting software Tecplot. Displacements were applied to the specimen edges to simulate realistic boundary conditions. An iterative procedure was adopted to ensure that the nodes at the lower boundary were free of tensile load as it is impossible for these nodes to be in tension. The obtained loading pattern was anti-symmetric across the interface. Further details of the loading condition and the finite element model can be found in Krishnan and Xu (2009). This stress value was then converted to a fringe order N which in turn was converted into a grayscale value. Half order fringes (0.5, 1.5, 2.5, etc.) were given a value of 255 and full order fringes (0, 1, 2, etc.) were assigned a value of 0 on the grayscale spectrum. The resulting fringe patterns, plotted with Tecplot, are compared with the experimentally observed patterns as depicted in Fig. 6. A close match was obtained between the simulated and experimental patterns thereby validating our finite element model.

**Fig. 6**

#### *4.2 Shear strength comparisons and effect of the interface shear stress on the bonding strength.*

The shear strengths from the different material-systems are reported in Table 2 and Table 3. Table 2 presents shear strength data obtained exclusively by testing Iosipescu shear specimens for a variety of indicated material systems. In each case, about 5-6 specimens were tested to ensure repeatability and the mean values along with their standard deviations are reported here. All the shear specimens were found to fail in shear along the bonding line in a sudden and brittle fashion except for Homalite/W10/Homalite and Homalite/polyester/Homalite systems. Bonded same-materials consistently show a greater value of shear strengths in comparison with bi-

material systems with the same adhesive bonding. This is attributed to a weaker bonding in case of bi-materials due to the mismatch in elastic properties. Similar to tensile bonding strengths, material systems with PMMA show a higher value of mean shear strength than systems with polycarbonate. Again, the difference between Loctite 384 and Weldon-10 bonding is significantly higher for PMMA bonded specimens than its polycarbonate counterparts in case of the same-material bonding. Materials bonded with Weldon-10 consistently report a value of higher shear strength than Loctite 384.

Bonding strengths of Homalite/adhesive/Homalite systems using different adhesives are also presented in Table 2. Shear bonding strengths of the same-material systems show very different values for various adhesives just as in tensile bonding strengths of the same Homalite/adhesive/Homalite systems. Homalite shear specimens bonded with strong adhesives Weldon-10 and polyester, were found to fail in tension in the Homalite part, rather than in shear across the bonded interface (Xu et al., 2004b). Thus, its actual shear bonding strength cannot be measured; but, the lower limit of the shear bonding strength is obtained as seen in Table 2. However, for PMMA and polycarbonate, actual shear bonding strengths can be measured using Iosipescu shear tests as their tensile strengths are much higher than that of Homalite.

**Table 2.**

Table 3 contains shear strength data obtained from both Iosipescu and short-beam shear tests. Here, in each case about 25-30 specimens were tested. Also, specimens for which data is reported in Table 3 were bonded only using weak adhesive Loctite 384. These data indicate only a small difference between measured shear bonding strengths of Iosipescu and short-beam shear specimens, although their interfacial shear stress distributions are very different as shown in Fig.4. Therefore, interfacial shear stress distributions have the least effect on the shear strength

masurement. It has been demonstrated that short-beam shear specimens are more efficient in machining than Iosipescu shear specimens (Krishnan and Xu, 2009).

**Table 3.**

## 5. FRACTURE TOUGHNESS FOR SAME AND DISSIMILAR-MATERIAL JOINTS

### 5.1 Principles on fracture toughness measurements

Edge-notched fracture specimens were used to measure the mode I fracture toughness. The specimens were designed and tested to the following dimensions: specimen width  $W=38$  mm, specimen thickness  $B=5.4$  mm and initial crack length  $a=19$  mm. All specimens had an initial crack with  $a/W = 0.5$  made before bonding by using scotch tape. All of the fracture specimens were tested in three-point bending (Suresh et al., 1990). The length of the initial crack in a bi-material specimen in such a case would have to be chosen carefully to enable fracture in a single mode (mode I). The mode I fracture toughness  $K_{IC}$  for same-material joints was calculated using equation (5) (Anderson, 1995).

$$K_{IC} = \left( \frac{P_Q S}{BW^{3/2}} \right) f(x) \quad 0 < x = a/W < 1$$

$$f(x) = \frac{3}{2} \sqrt{x} \frac{[1.99 - x(1-x)(2.15 - 3.93x + 2.7x^2)]}{(1+2x)(1-x)^{3/2}} \quad (5)$$

where  $P_Q$  is the maximum load from the load-displacement plot,  $S$  is the support span,  $f(x)$  accounts for the correction due to the specimen geometry. In case of bi-materials, the calculation of fracture toughness becomes very different. First, the asymptotic stress field of an interfacial crack in a bi-material specimen,  $\sigma_{ij}$  can be expressed as (Rice, 1988)

$$\sigma_{ij} = \frac{1}{\sqrt{2\pi r}} [ \operatorname{Re} \{ K r^{i\varepsilon} \} \sigma_{ij}^{-I}(\theta; \varepsilon) + \operatorname{Im} \{ K r^{i\varepsilon} \} \sigma_{ij}^{-II}(\theta; \varepsilon) ] \quad (6)$$

where  $K=K_1+iK_2$  is the complex stress intensity factor,  $\sigma_{ij}^{I}$  and  $\sigma_{ij}^{II}$  are the stresses in mode I and mode II, and  $\varepsilon$  is a function of Dundur's parameters  $\beta$  and is given by

$$\varepsilon = \frac{1}{2\pi} \ln \left\{ \frac{1 - \beta}{1 + \beta} \right\} \quad (7)$$

The elastic properties of aluminum include a Young's modulus of  $E=71$  GPa, a shear modulus  $\mu=26.7$  GPa and a Poisson's ratio of  $\nu=0.33$ . Corresponding elastic properties for polycarbonate used in this calculation are  $E=2.4$  GPa,  $\mu=0.9$  GPa,  $\nu=0.34$ . Hence, the two Dundur's parameters for the material combination of polycarbonate and aluminum are calculated as  $\alpha=0.93$  and  $\beta=0.31$ . It should be noted here that PMMA, although chemically different, has similar elastic properties as polycarbonate. Therefore, the Dundur's parameters for PMMA/aluminum are also the same as in above. A schematic of our bi-material specimen used to obtain the fracture toughness value is illustrated in Fig. 7.

**Fig.7**

A general form for the stress intensity factor for a bi-material specimen is given as (O'Dowd et al., 1992)

$$K = YT \sqrt{\alpha} \alpha^{-i\varepsilon} e^{i\psi} \quad (8)$$

where  $T=P(3B/W^2)$ ,  $Y$  and  $\psi$  are calibrating factors which depend on  $a/W$ ,  $B/W$  and the Dundur's parameters. Then the stress intensity factor in mode I can be expressed as

$$K_I = \text{Re} \{ K \alpha^{i\varepsilon} \} \quad (9)$$

Using equations (8) and (9), the bi-material fracture toughness  $K_{IC}$  is calculated as

$$K_{IC} = \frac{3P_Q S}{BW^2} Y \sqrt{a} \cos(\psi) \quad (10)$$

Here,  $Y=2.4$  and  $\psi=7.8$  degrees, the fitting parameters are obtained from O'Dowd et al. (1992) for  $\beta=\alpha/3$  as is in our case.

### *5.2 Fracture toughness results*

The material systems and their measured  $K_{IC}$  values are presented in Table 4. During experiments, the load required to completely break the specimen under three-point bending was recorded and the value of  $K_{IC}$  was calculated using equation (5) for same-material joints and using equation (10) for bi-material systems. It was observed that Weldon-10 bonding shows a slightly higher value of  $K_{IC}$  than Loctite 384 bonding for most material systems. Only polycarbonate/384/aluminum shows a decrease of 10% in fracture toughness from the corresponding weak bond. However, it was also observed that the standard deviation in case of Weldon-10 bonding was higher than Loctite-384 bonding. Generally bi-material fracture specimens show a small difference of  $K_{IC}$  values between the two types of strong and weak adhesives. Similar to its tensile and shear bonding strengths, PMMA shows a better bonding with the two types of adhesives and hence a greater value of fracture toughness is obtained for bonded PMMA specimens. Bi-material specimens consistently show a lower value of mode I fracture toughness than same-material specimens.

Surprisingly, Homalite/polyester/Homalite material systems show lower fracture toughness than other strong adhesive systems used in conjunction with Homalite: Weldon-10 and Loctite 330. It should be noted that polyester provides the highest tensile and shear bonding strengths as can be seen in Tables 1 and 2. Therefore, strength and fracture toughness are very different parameters and should be measured for every new material system. The fracture

toughnesses of other adhesive systems show a trend similar to the bonding strengths of the same-material joints, i.e., bonding strengths increase with fracture toughnesses from weak bonding to strong bonding.

**Table 4**

## 6. CONCLUSIONS

Five different types of strong and weak adhesives (Weldon-10, Loctite 384, Loctite 330, Loctite 5083 and polyester) were used in conjunction with five types of materials (aluminum, steel, PMMA, polycarbonate and Homalite) to produce a variety of bonded material systems. These material systems (same and bi-material joint) are tested in shear, tension and fracture. Results indicate that materials bonded with Weldon-10 and polyester consistently show higher tensile and shear bonding strengths than the same-material systems bonded with other adhesives. However, bi-material fracture toughness (mode I) tends to show lesser difference between the weak and strong adhesive bonding. In general, bi-material systems in shear and fracture report lower properties than the same-material systems due to higher property mismatch involved in bi-material systems. Specimens bonded with PMMA consistently show higher values of shear and tensile bonding strengths, and mode I fracture toughness than polycarbonate systems. A wide variety of carefully measured experimental data will be highly beneficial for computational simulations on failure mechanics of adhesive joints.

## Acknowledgements

The authors acknowledge the support from the Office of Naval Research and the National Science Foundation.

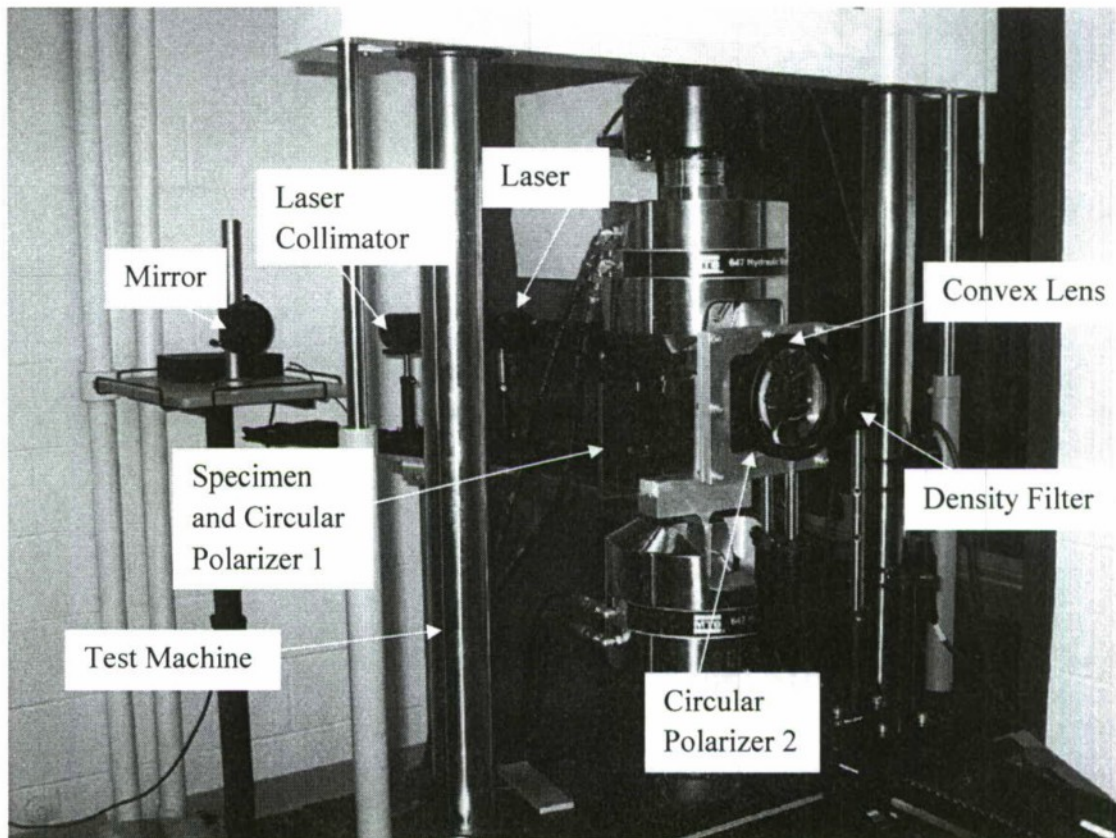


**Figure 1.** Experimental setup of a mechanical-optical system to record in-situ photoelasticity during loading process

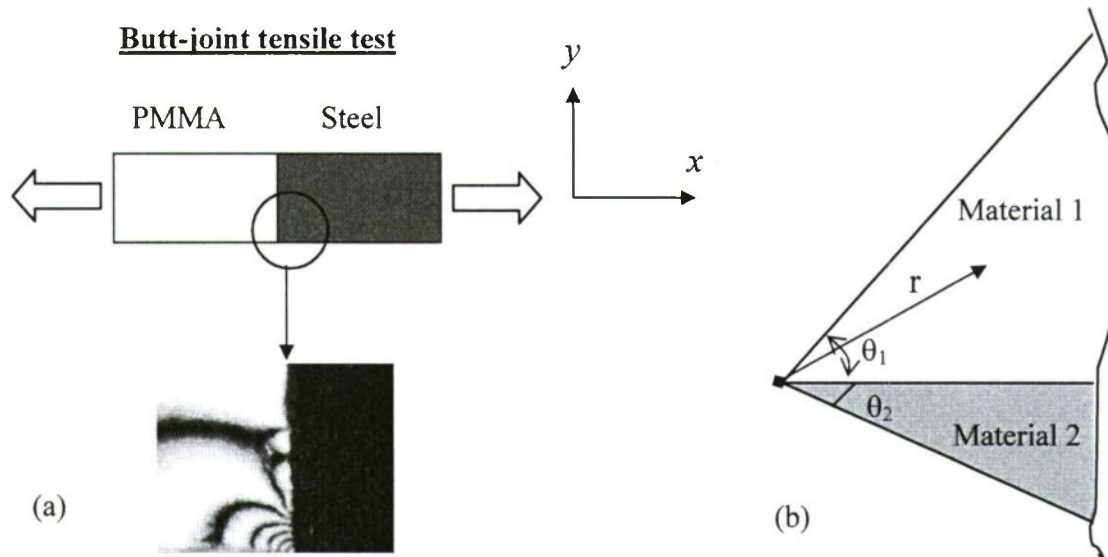


**Figure 2.** (a) Coherent Gradient Sensing (CGS) photograph showing a strong stress concentration (associated with fringe pattern concentrations) at the free edges of a bonded metal and polymer subjected to tensile load (b) Angular definition of a bi-material wedge.

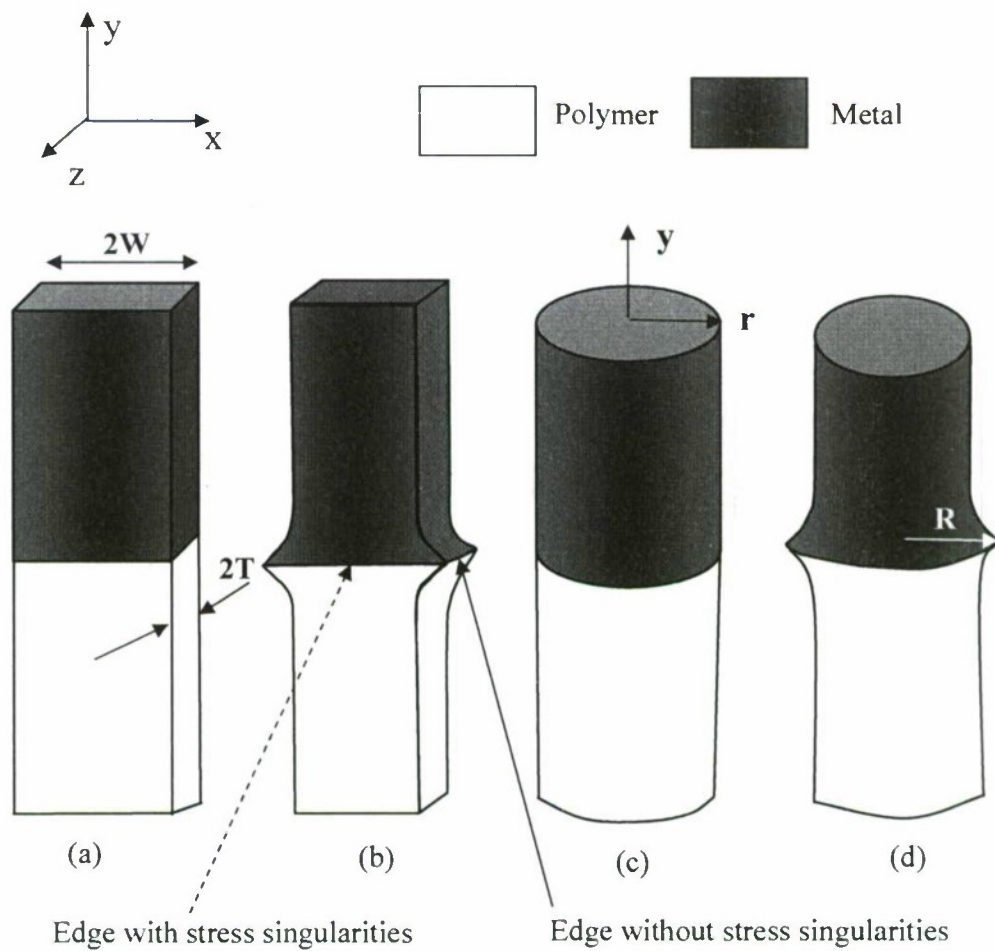


**Figure 3.** Schematic diagrams of metal-polymer joint specimens with (a) straight edges (baseline); (b) convex edges with least stress singularities; (c) axisymmetric straight joints (baseline); (d) axisymmetric convex joints with least stress singularities.

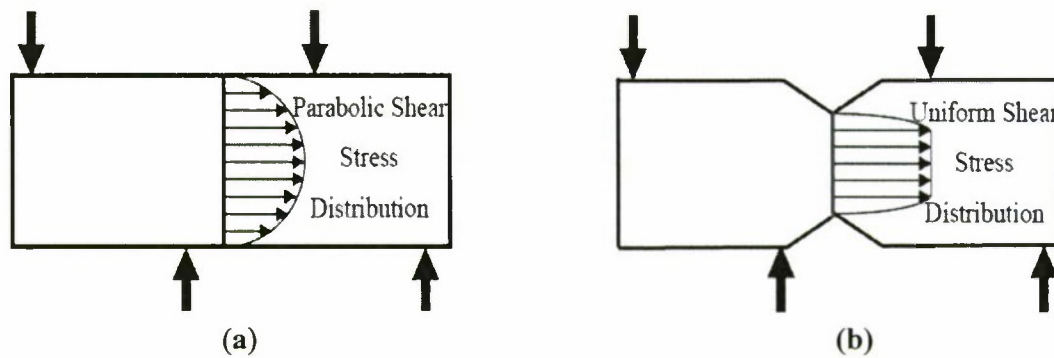


**Figure 4.** Schematic models indicating the structure of (a) Short-beam shear and (b) Iosipescu specimen.

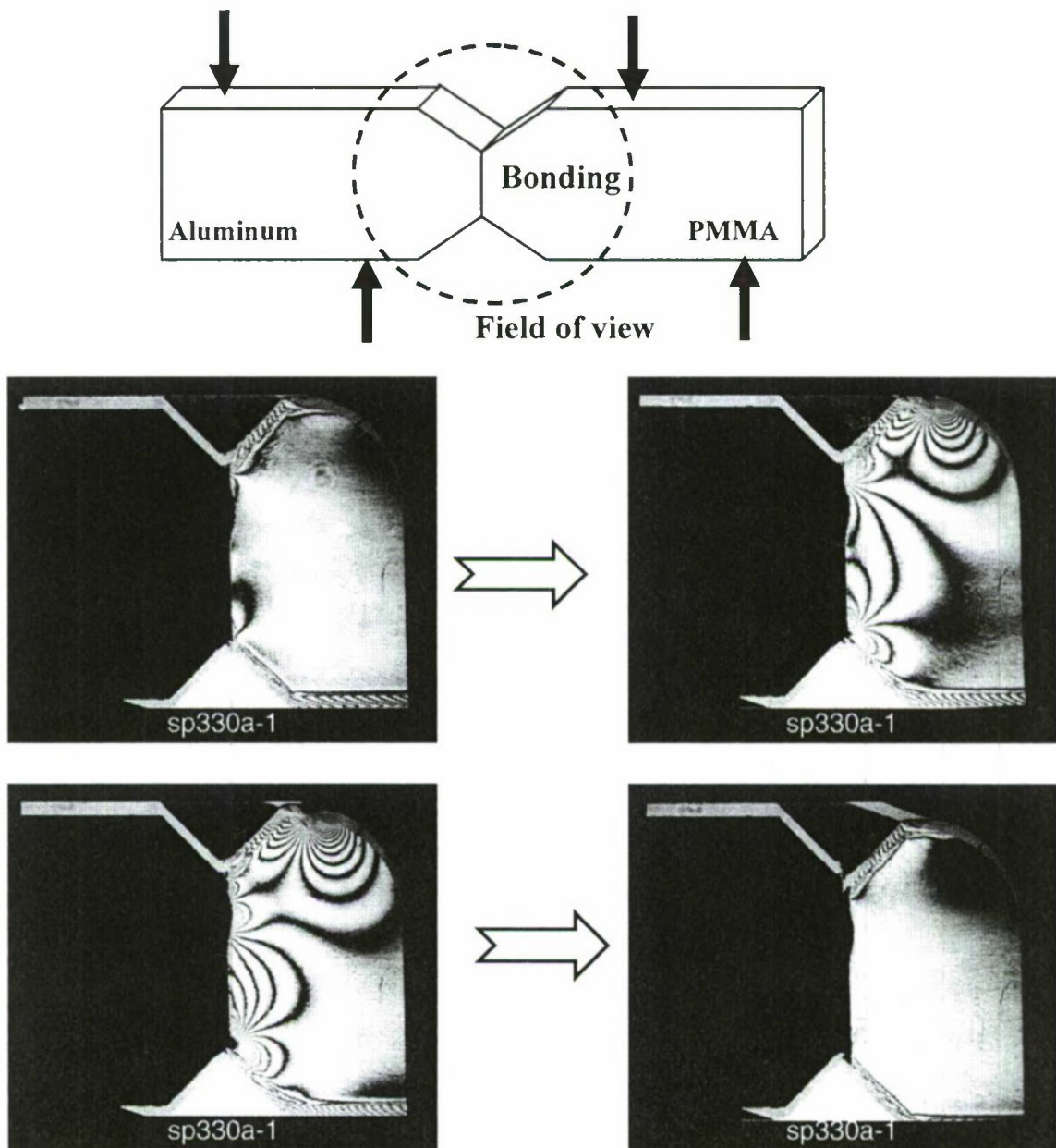


**Figure 5.** CGS fringe pattern development for bonded PMMA/W10/aluminum Iosipescu shear specimen. The first snapshot shows fringe just evolving as the loading is increased and the last snapshot shows the final fracture in the bonded bi-material specimen with a clear shear displacement at the interface.

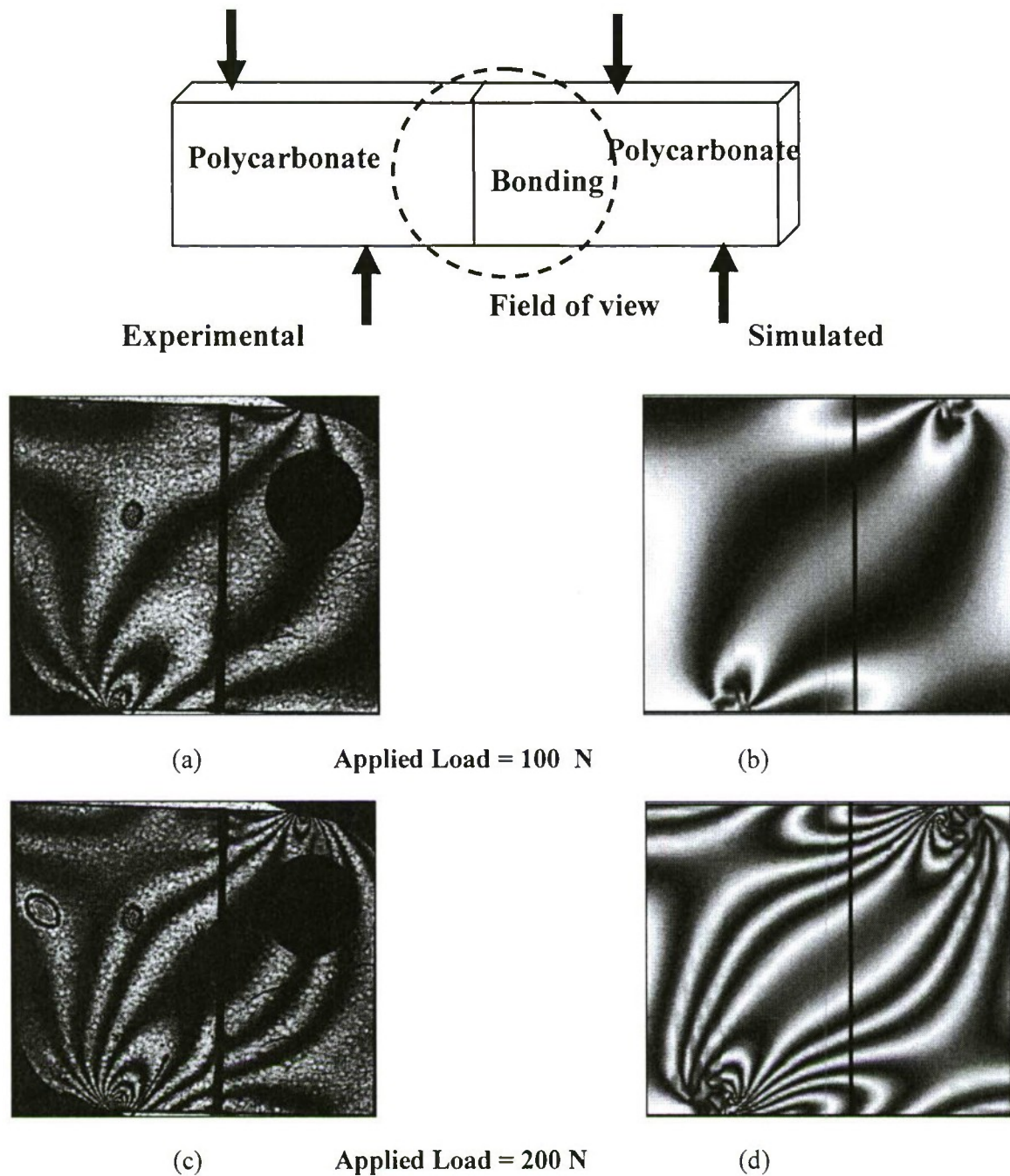


**Figure 6.** Comparison between experimental and finite element generated fringe patterns for a typical polycarbonate short-beam shear specimen.

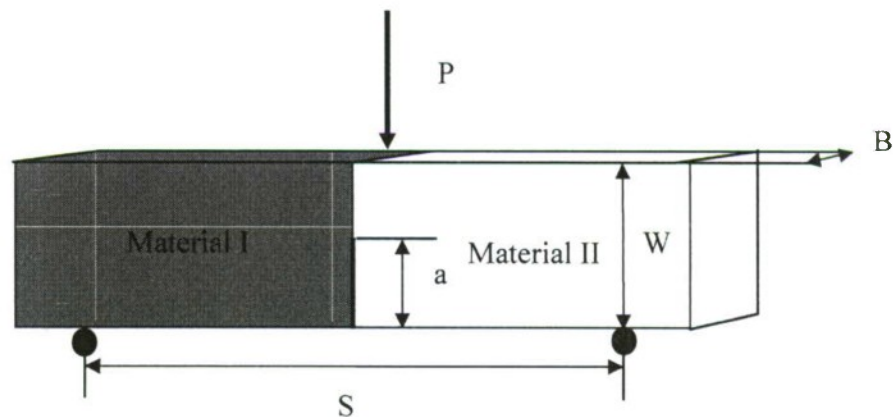


**Figure 7.** Bi-material specimen for mode-I fracture toughness measurement ( $a/W=0.5$ )

**Table 1.** Tensile bonding strengths for same and bi-material joints

Material/adhesive/material	Tensile Strength (MPa)	Notes
<b>Same-Material Bond</b>		
Polycarbonate /384/ Polycarbonate	6.06 ± 1.64	+113 % increase strong/weak
Polycarbonate /W10/ Polycarbonate	12.93 ± 1.36	
PMMA/384/PMMA	12.66 ± 1.63	+64 % increase strong/weak
PMMA/W10/PMMA	20.87 ± 6.21	
Homalite/Polyester/Homalite	28	Xu et al., 2002
Homalite/W10/Homalite	7.74	
Homalite/330/Homalite	7.0	
Homalite/384/Homalite	6.75	
Homalite/5083/Homalite	1.53	Xu et al., 2002
<b>Bi-Material Bond</b>		
Polycarbonate /384/aluminum	9.57 ± 0.72	Wang and Xu, 2006
Polycarbonate /W10/aluminum	11.35	
PMMA/384/aluminum	10.01 ± 0.93	Wang and Xu, 2006
PMMA/W10/ aluminum	12.85	
Homalite/330/steel	5.38	Xu et al., 2002
Homalite/384/steel	3.25	

**Table 2.** Shear bonding strengths for same and bi-material joints

Material/adhesive/material	Shear Strength (MPa)	Notes
<b>Same-Material Bond</b>		
Polycarbonate/384/ Polycarbonate	10.99 ± 1.45	+41 %
Polycarbonate/W10/ Polycarbonate	15.52 ± 2.74	
PMMA/384/PMMA	11.58 ± 2.15	+119 %
PMMA/W10/PMMA	25.35 ± 2.25	
Homalite/W10/Homalite	>21.65	Xu et al., 2002
Homalite/Polyester/Homalite	>23.26	
Homalite/330/Homalite	12.58	
Homalite/384/Homalite	7.47	
Homalite/5083/Homalite	0.81	Xu et al., 2002
<b>Bi-Material Bond</b>		
Polycarbonate/384/aluminum	6.18 ± 2.16	65 %
Polycarbonate/W10/aluminum	10.18 ± 4.35	
PMMA/384/aluminum	8.63 ± 0.85	18 %
PMMA/WD10/aluminum	10.16 ± 3.92	

**Table 3.** Shear bonding strengths of Iosipescu and short-beam shear specimens

Material/adhesive/material	Iosipescu Shear (MPa)	Short-Beam Shear(MPa)	Difference
Aluminum/384/Aluminum	10.75 ± 2.39	10.16 ± 2.41	5.5 %
Polycarbonate/384/Polycarbonate	10.99 ± 1.45	8.51 ± 1.13	22.5 %
PMMA/384/PMMA	11.58 ± 2.15	10.19 ± 0.57	12 %

**Table 4.** Mode-I fracture toughness for same and bi-material joints

Material/adhesive/material	Mean $K_{IC}$ (MPa m <sup>1/2</sup> )	Difference (%)
<b>Same-Material Bond</b>		
Polycarbonate/384/Polycarbonate	$0.64 \pm 0.02$	+36 %
Polycarbonate/W10/Polycarbonate	$0.86 \pm 0.16$	
PMMA/384/PMMA	$0.71 \pm 0.06$	+147 %
PMMA/W10/PMMA	$1.74 \pm 0.15$	
Homalite/Polyester/Homalite	0.56	Xu et al., 2002
Homalite/W10/Homalite	0.83	
Homalite/330/Homalite	0.75	
Homalite/384/Homalite	0.38	
Homalite/5083/Homalite	0.19	Xu et al., 2002
<b>Bi-Material Bond</b>		
Polycarbonate/384/Aluminum	$0.1 \pm 0.01$	-10 %
Polycarbonate/W10/Aluminum	$0.09 \pm 0.02$	
PMMA/384/Aluminum	$0.12 \pm 0.01$	+17 %
PMMA/W10/Aluminum	$0.14 \pm 0.02$	

## References

1. Akisanya, A.R. and Fleck, N.A., "Interfacial cracking from the free-edge of a long bimaterial strip", *International Journal of Solids and Structures*, 34, 1645–1665 (1997).
2. Anderson, T.L., "Fracture mechanics 2<sup>nd</sup> ed.", CRC Press, Boca Raton (1995).
3. Bogy, D.B., "Two edge-bonded elastic wedges of different materials and wedge angles under surface tractions", *Journal of Applied Mechanics*, 38, 377–386 (1971).
4. Deng, S., Qi, B., Hou, M., Ye, L. and Magniez, K., "Assessment of interfacial bonding between polymer threads and epoxy resins by transverse fibre bundle (TFB) tests", *Composites: Part A*, 40, 1698–1707 (2009).
5. Gupta, V., Yuan, J. and Pronin, A., "Recent developments in the laser spallation technique to measure the interface strength and its relationship to interface toughness with applications to metal/ceramic, ceramic/ceramic and ceramic/polymer interfaces", *Journal of Adhesion Science and Technology*, 8, 713–747 (1994).
6. Hutchinson, J. W. and Suo, Z., "Mixed-mode cracking in layered materials", *Advances in Applied Mechanics*, 29, 63–191 (1992).
7. Kitey, R. and Tippur, H., "Dynamic crack growth past a stiff inclusion: Optical investigation of inclusion eccentricity and inclusion-matrix adhesion strength", *Experimental Mechanics*, 48, 37–54 (2008).
8. Kobayashi, A.S. (Ed.), "Handbook on Experimental Mechanics", Society for Experimental Mechanics, Inc. Prentice-Hall, New Jersey (1987).
9. Krishnan, A. and Xu, L.R., "Effect of the interfacial stress distribution on the material interfacial shear strength measurement", *Experimental Mechanics*, in press (2009).
10. Lara-Curzio, E., Ferber, M.K., Besmann, T.M., Rebillat, F. and Lamon, J., "Fiber-matrix bond strength, fiber frictional sliding and the macroscopic tensile behavior of a 2D SiC/SiC Composite with tailored interfaces", *Ceramics Engineering and Science*, 15, 597–612 (1995).
11. Martin E., Leguillon D. and Lacroix C., "A revisited criterion for crack deflection at an interface in a brittle material", *Composites Science and Technology* 6, 1671–1679 (2001).
12. Needleman, A. and Rosakis, A.J., "The effect of bond strength and loading rate on the conditions governing the attainment of interersonic crack growth along interfaces", *Journal of Mechanics and Physics of Solids*, 47, 2411–2449 (1999).
13. O'Dowd, N.P., Shih, C.F. and Stout, M.G., "Test geometries for measuring interfacial fracture toughness", *International Journal of Solids and Structures*, 29 (5), 571–589 (1992).
14. Reedy Jr., E.D. and Guess, T.R., "Comparison of butt tensile strength data with interface corner stress intensity factor prediction", *International Journal of Solids & Structures*, 30, 2929–2936 (1993).
15. Rice, J.R., "Elastic fracture mechanics concepts for interfacial cracks", *Journal of Applied Mechanics*, 55, 98–103 (1988).
16. Singh, R.P., Lambros, J., Shukla, A. and Rosakis, A.J., "Two optical techniques applied to the investigation of the mechanics of crack propagation along a bimaterial interface", *Proceedings of the Royal Society of London A*, 453, 2649–2667 (1997).
17. Suresh, S., Shih, C.F., Morrone, A. and O'Dowd, N.P., "Mixed-Mode fracture toughness of ceramic materials", *Journal of the American Ceramic Society*, 73(5), 1257–1267 (1990).
18. Tandon, G.P., Kim, R.Y., Warrier, S.G. and Majumdar, B.S., "Influence of free edge and corner singularities on interfacial normal strength: application in model unidirectional composites", *Composites, Part B: Engineering*, 30, 115–134 (1999).

19. Tippur, H.V., Krishnasamy, S. and Rosakis, A.J., "A coherent gradient sensor for crack tip deformation measurements: analysis and experimental results", *International Journal of Fracture*, 48, 193–204 (1991).
20. Xu, L.R. and Rosakis, A.J., "Impact failure characteristics in sandwich structures; Part II: effects of impact speed and interfacial strength", *International Journal of Solids and Structures*, 39, 4237–4248 (2002).
21. Xu, L.R., Samudrala, O. and Rosakis, A.J., "Measurements of Interfacial mechanical properties with the aid of two optical techniques", *Proceedings of the 2002 SEM Annual Conference and Exposition on Experimental and Applied Mechanics*, Society for Experimental Mechanics, Inc., Bethel, CT, USA, Paper 34. (2002)
22. Xu, L.R., Kuai, H. and Sengupta, S., "Dissimilar material joints with and without free-edge stress singularities: Part I. A biologically inspired design", *Experimental Mechanics*, 44(6), 608-615 (2004a)
23. Xu, L.R., Sengupta, S. and Kuai, H., "An experimental and numerical investigation of adhesive bonding strengths of polymer materials", *International Journal of Adhesion and Adhesives*, 24, 455-460 (2004b)
24. Wang, J. "Recent development in thin film adhesion measurement by laser-induced stress waves", *Experimental Mechanics*, 22, 249-257 (2007)
25. Wang, P. and Xu, L.R., "Convex interfacial joints with least stress singularities in dissimilar materials", *Mechanics of Materials*, 38, 1001-1011, (2006).
26. Williams, M.L., "Stress singularities resulting from various boundary conditions in angular corners of plates in extension", *Journal of Applied Mechanics*, 19, 526–528 (1952).